

# **Electronic spectroscopy of carbon chain radicals using cw cavity ring down in conjunction with mass detection**

## **Inauguraldissertation**

Zur Erlangung der Würde eines Doktors der Philosophie vorgelegt der  
Philosophisch-Naturwissenschaftlichen Fakultät  
der Universität Basel

von

**Dmitriy Khoroshev**

aus Tobolsk (Russland)

Basel, 2005

Genehmigt von der Philosophisch-Naturwissenschaftlichen Fakultät

auf Antrag von

Prof. Dr. John P. Maier und Prof. Dr. Martin Jungen

Basel, den 5. April 2005

Prof. Dr. Jakob Wirz

Dekan

*To my family*



## *Acknowledgements*

I gratefully acknowledge the helpful collaborative efforts of all my colleagues working in the group of Professor John Maier in the period from 2000 till 2005.

I would like to express personal gratitude to John Maier, who gave me a chance of doing Ph.D. in Basel. He provided me with a pleasant working environment and necessary resources to carry on with my learning and research activities. Professor Martin Jungen is also thanked for acting as co-referee for my thesis.

Dr. David Pfluger introduced me to the experimental set-up and the laser technique. He helped me a lot with my Diploma work, Mater's thesis, German and showed what-is-where in Basel during my first months. Dr. Petre Birza has been working with me in a lab for the last four years and took care of the cw-CRD spectrometer and the ion source. I am grateful to him for the fruitful discussions, advices, and enjoyable times.

I kindly thank Dr. Wayne Sinclair, Dr. Harold Linnartz, and Dr. Andrei Chirokolava for their guidance and assistance during the first three years of my study, especially Harold for his enthusiasm, support, and valuable comments.

Dr. Mitsunori Araki has been my collaborator and scientific adviser during the last two years. I am particularly indebted to him for introducing me to the asymmetric-top rotational structure analysis and contribution to the preparation and presentation of the spectroscopic results described in this work. His guidance and advices are greatly appreciated and will never be forgotten.

My new colleagues Richa Chauhan, Vitaly Rudnev, and Dr. Eun Soonk Kim just joined cw-CRD lab. They will continue development and improvement of the experiment and I wish them good luck and plenty of results.

There are some people who I would like to acknowledge for sharing their knowledge, experimental skills and experience with me: Dr. Tomasz Motylewski developed the CRD software. Dr. Przemyslaw Kolek performed the *ab initio* calculations. Dr. Thomas Pino, Dr. Felix Güthe, and Prof. Evan Bieske provided valuable recommendations concerning the TOF mass spectrometer. Dr. Evan Jochnowitz is especially thanked for the English grammar corrections.

I am also grateful to the people who were technically involved in the experiment: Mr. Mutschler for his extraordinary skills in constructing sophisticated mechanical devices. Dieter Wild and Grischa Martin for their assistance and effort in maintaining the technical hardware.

Georg Holderied for the solving the electronical problems. Jacques Lecoultre for the synthesising the isotopic substances.

My sincere appreciations are given to Esther Stalder and Daniela Tischhauser from secretary office for the taking care of bureaucratic matters and making my life easier. The Swiss National Science Foundation and the City of Basel are thanked for the financial support.

I am also indebted to many people outside of the institute, from which I received support and encouragement: Professor Nikolay M. Bazhin from Novosibirsk State University awoke in me an interest in physical chemistry. I would have never found the position in Basel without him. Dr. Lyudmila A. Belchenko provided invaluable help during my study in Novosibirsk. Finally, I would like to thank my family and Tanja for moral support, kindness, and caring.

---

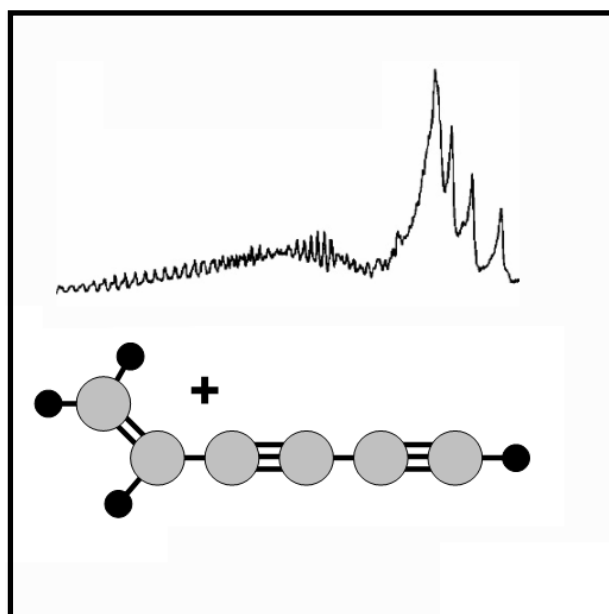
<b>1</b>	<b>Introduction</b>	<b>1</b>
1.1	Motivation	3
1.2	Spectra of $C_6H_4^+$ in gas phase and matrix	5
1.3	Structure of this thesis	6
<b>2</b>	<b>Theory</b>	<b>7</b>
2.1	Theory of rotational structure	9
2.2	Analysis of rotational structure	12
<b>3</b>	<b>Experiment</b>	<b>15</b>
3.1	Principle of CRD spectroscopy	17
3.2	History of cw-CRD spectrometer	20
3.3	Experimental set-up of the cw-CRD spectrometer	23
3.4	Ion source	25
<b>4</b>	<b>Spectroscopic results</b>	<b>29</b>
4.1	Origin band	31
4.2	Vibrationally excited band	34
4.3	<i>Ab initio</i> calculations	37
<b>5</b>	<b>TOF mass spectrometer</b>	<b>39</b>
5.1	Principles of TOF mass spectrometry	41
5.2	Design of the TOF mass spectrometer	44
5.3	Mass spectrometric results	50
<b>6</b>	<b>Summary and outlook</b>	<b>55</b>
<b>7</b>	<b>References</b>	<b>59</b>
<b>8</b>	<b>Appendix</b>	<b>65</b>
8.1	Asymmetric rotors	67
8.2	Laser system and optical components	70
8.3	Observed line positions	73
8.4	Micro channel plates	82
8.5	Publications	84
8.6	Curriculum vitae of the author	101





# 1

## Introduction





# 1.1 Motivation

High resolution spectroscopy of unsaturated carbon chain radicals is interesting from the viewpoint of interstellar hydrocarbon chemistry as well as terrestrial chemical processes, such as the formation of fullerenes [1–3]. Carbon clusters are known to be present in hydrocarbon flames and other soot-forming systems [4–6], and the study of these species is necessary for understanding of these complex chemical environments. For example, soot processes are a dominant feature of hydrocarbon/air diffusion flames; they affect fundamental reaction mechanisms within the flame environment [7]. Formation of soot is an important unresolved problem of combustion science for several reasons: soot emissions are responsible for more deaths than any other combustion pollutant, thermal loads due to continuum radiation from soot limit the durability of combustors, thermal radiation from soot is mainly responsible for the growth and spread of unwanted fires, and carbon monoxide associated with soot emissions is responsible for most fire deaths [8]. Clearly, a detailed knowledge of the physical and chemical properties of carbon clusters is important for understanding a large variety of chemical systems.

In addition to such practical considerations, carbon clusters are fascinating examples of the richness and variety of carbon chemistry in itself [2]. Due to the enormous bonding flexibility of carbon, viz. its unique ability to form stable single, double, or triple bonds, carbon clusters appear in a wide range of structural forms that are synthesized spontaneously in hot carbon plasmas. For example, researchers have been puzzling for more than a decade over the ability of a molecule as symmetric as the icosahedral  $C_{60}$  cluster to form in such a spontaneous way [9]. Understanding the evolution of carbon cluster structure is both a major scientific challenge and requires state of the art experimental and theoretical techniques.

In the John Maier's group the electronic transitions of the chain species  $HC_nH^+$   $n = 6, 8, 10$  [10–12] and  $C_nH$  [13] with an even number of carbons have been studied. Recently, a nonlinear planar carbon chain radical  $C_6H_4^+$ , was detected in a supersonic planar discharge by cavity ring down (CRD) spectroscopy in the 604 nm region [14]. The related  $C_4H_4^+$  and  $C_8H_4^+$  nonlinear carbon chains were also produced and detected in this plasma [15].

## 1. Introduction

---

Hydrogenated nonlinear chains can exist in dark interstellar clouds as well as the linear ones, e.g., column densities of  $C_2O$ ,  $H_2CCO$ , and  $CH_3CHO$  are of the same order of magnitude in the TMC-1 dark cloud [16]. Therefore, long nonlinear carbon chains having an asymmetric top structure may be present in such clouds with comparable abundance. However, they have not yet been detected by radioastronomy because their pure rotational transitions are too weak compared to those of linear carbon chains. If a sufficiently long integration in the radio observations could be carried out based on an accurate rest frequency, identification may prove possible in the future. Thus laboratory measurements of the pure rotational transitions are necessary, and in turn this requires reasonable a priori knowledge of the ground state rotational constants. A rotationally resolved electronic spectrum can produce such constants both in the ground and excited states. For this reason the  ${}^2A''-X{}^2A''$  origin band of  $C_6H_4^+$  was recorded using high-resolution cw-CRD spectroscopy as part of this work. Additionally, an unassigned 585.3 nm absorption band, produced by a molecule having the same mass as  $C_6H_4^+$ , was observed in a 6 K neon-matrix [14]. To identify the carrier, this frequency region was scanned in the gas phase using cw-CRD spectroscopy, and a rotationally resolved band was observed at 581 nm.

The other part of this work consisted of building a linear time-of-flight (TOF) mass spectrometer. This allowed real-time analysis of the production in the pulsed supersonic planar plasma expansion. This upgrade provides an efficient way to optimize discharge conditions for the synthesis of a preferred species.

## 1.2 Spectra of $C_6H_4^+$ in gas phase and matrix

This thesis concerns the high resolution spectroscopy of the  $C_6H_4^+$  cation radical. The first spectrum of  $C_6H_4^+$  was obtained by Araki *et. al.* around 604 nm by using a pulsed-CRD spectrometer with planar discharge of a mixture of acetylene in helium [14]. Because the spectrum had clear rotational and  $K$ -type structure, it was assigned as a nonlinear species. Using  $C_2D_2$  and  $C_2D_2/C_2H_2$  mixtures led to the conclusion that the carrier was of the form  $C_nH_4^{(+)}$  with two similar hydrogen atoms. The rotational analysis of the spectra allowed the determination of the number of carbon atoms ( $n$ ) in the chain. The obtained molecular constants  $A$ ,  $B$  and  $C$  indicated that the observed molecule was very likely to be  $C_6H_4^{(+)}$ . But it was not possible to discriminate between the neutral and cationic species from the rotational analysis alone. However, the experimental condition favored the creation of a charged species. The authors went on to suggest that for the neutral  $C_6H_4$  closed-shell system the electronic transitions are expected to be in the UV. A mass-selective matrix study following the gas phase analysis proved the presence of the cationic species in the plasma discharge. Two strong bands for  $C_6H_4^+$  were observed around 609 and 585 nm. No strong lower energy band was observed; therefore the band at 609 nm was assigned as the origin band. The band at 585 nm was suggested to be due to another isomer of  $C_6H_4^+$ . *Ab initio* calculations (ROHF/6-31G\*\*) were used to find the geometry that best reproduced the observed spectra (Figure 1-1).

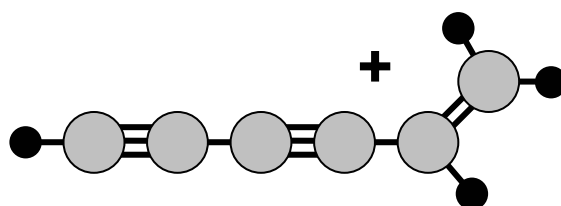


**Figure 1-1.** Geometry of the observed isomer of  $C_6H_4^+$ .

## 1.3 Structure of this thesis

The manuscript is organized in the following way. Chapter 2 compares the theory of the rotational structure in asymmetric and symmetric rotors. It describes the rotational levels and transition energies of the system studied. Section 2.2 contains the analysis of the spectra. Two different approaches are described. The manual fit and the least-squares fitting routine were applied to the analysis of the low and the high resolution spectra respectively.

Chapter 3 is devoted to the experimental apparatus. First part summarizes the principle of CRD spectroscopy and history of the development of cw-CRD spectrometers. Section 3.3 explains the present set-up. Last part gives a detailed description of the ion source.

Chapter 4 covers the spectroscopic results on the origin and vibrationally excited bands of both  $C_6H_4^+$  and  $C_6D_4^+$  radicals. It includes observed spectra, assignment, and molecular constants.

Chapter 5 describes the TOF mass spectrometer and obtained mass spectra of cations that are formed in a supersonic planar plasma expansion.

Chapter 6 summarizes the obtained results and gives an outlook for the possible future studies.

# 2

## Theory

$$\nu_{\text{peak}} = K^2 \Delta A + K \Delta B + T_{00}$$

R branch. In an R-branch transitions  $\Delta J = 1$  conse

$$E'/h = B'(J''+1)(J''+2) + (A' - B')K^2 + T_{00}$$

The frequency of the transition can be written as

$$\begin{aligned} \nu &= B'(J''+1)(J''+2) - B''J''(J''+1) + (\Delta A - \Delta B)K^2 + T_{00} \\ &= \Delta B(J''+1)J'' + 2B''(J''+1) + (\Delta A - \Delta B)K^2 + T_{00} \end{aligned}$$

And the distance between lines of neighbor  $J$  and

$$\nu(J+1) - \nu(J) = 2(J+1)\Delta B + 2B''$$

this information to express the energetics of  
ate the relevant molecular constants as described





## 2.1 Theory of rotational structure

Let us consider an asymmetric-top molecule rotating around three principal axes of inertia. The energy of rotation may be written as

$$W = P_a^2/(2I_a) + P_b^2/(2I_b) + P_c^2/(2I_c) \\ = (4\pi^2 A/h)P_a^2 + (4\pi^2 B/h)P_b^2 + (4\pi^2 C/h)P_c^2 \quad (2-1)$$

The rotational constants  $A$ ,  $B$ , and  $C$  are all different, unlike a symmetric rotor case, where  $B = C$  or  $B = A$ . If  $B$  differs from  $C$  by only a small amount (Figure 2-1), the rotor may be called a near prolate asymmetric top. A slight asymmetry splits the levels  $\pm K$  which are degenerate for symmetric tops. The energy of a slightly prolate asymmetric rotor may be conveniently written in the form

$$E/h = \frac{1}{2}(B+C)J(J+1) + (A - \frac{1}{2}(B+C))w \quad (2-2)$$

where centrifugal distortion has been neglected. The function  $w$  depends on molecular constants and rotational quantum numbers [17].

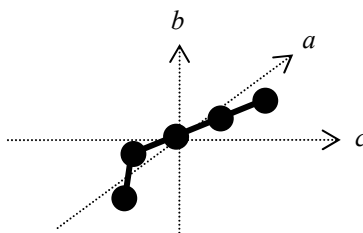


**Figure 2-1.** Principal axes of inertia of a slightly prolate asymmetric-top molecule.

The selection rule governing the changes in  $J$  quantum number in asymmetric rotors is similar to the rule that governs any transition involving the rotation of the molecules.

$$\Delta J = 0, \pm 1 \quad (2-3)$$

Transitions with  $\Delta J = 0$  are called  $Q$ -branch transitions and those with  $\Delta J = +1$  and  $-1$  are  $R$ - and  $P$ -branch transitions, respectively. Quantum number  $K$  is associated with  $K_a$  and  $K_c$  of prolate and oblate symmetric rotors. More information concerning the rotational quantum numbers can be found in the Appendix. Cross and co-workers summarized the stronger transitions in an asymmetric rotor spectrum [18]. This thesis concerns  $a$ -type transition of a near-prolate asymmetric rotor. For these molecules the most intense transitions take place in  $P$  branch when  $\Delta K_a = 0$  and  $\Delta K_c = -1$ ; in  $Q$  branch when  $\Delta K_a = 0$  and  $\Delta K_c = \pm 1$ ; in  $R$  branch when  $\Delta K_a = 0$  and  $\Delta K_c = 1$ .

## 2. Theory

---

In order to simplify the analysis of a slightly prolate asymmetric rotor let us assume  $B = C$ . Therefore we start by treating our molecule as a prolate symmetric top.

The Equation 2-2 may be written now in the form

$$E/h = BJ(J+1) + (A-B)K^2 \quad (2-4)$$

where the function  $w$  equals to  $K^2$ . Now we rewrite this expression applied to the electronic states.

$$E'/h = B'J'(J'+1) + (A'-B')K^2 + T_{00} \quad (2-5)$$

The energy term of the excited state ( $E'$ ) includes the transition energy of the origin band ( $T_{00}$ ). For the ground electronic state ( $E''$ ) Equation 2-4 may be written as

$$E''/h = B''J''(J''+1) + (A''-B'')K^2 \quad (2-6)$$

The difference between  $E'$  and  $E''$  gives the frequency of the electronic transition

$$\nu = E'/h - E''/h \quad (2-7)$$

The selection rules for the prolate symmetric-top molecules applied to  $J$  are similar to the ones shown above (Equation 2-3). However for  $K$  quantum number only transitions with  $\Delta K = 0$  have significant intensity. This is due to the fact that  $K = K_a$  in a prolate symmetric rotor.

Examples below demonstrate the derivation of the transition frequencies for  $P$ ,  $Q$  and  $R$  branches.

1.  $P$  branch. If Equation 2-5 is written while constraining  $\Delta J = -1$  or  $J'' = J' + 1$ , then

$$E'/h = B'(J''-1)J'' + (A'-B')K^2 + T_{00} \quad (2-8)$$

Frequency of the transition according to the Equation 2-7 can now be written as:

$$\begin{aligned} \nu &= B'(J''-1)J'' - B''J''(J''+1) + (\Delta A - \Delta B)K^2 + T_{00} \\ &= \Delta B(J''-1)J'' - 2B''J'' + (\Delta A - \Delta B)K^2 + T_{00} \end{aligned} \quad (2-9)$$

Where  $\Delta A$  and  $\Delta B$  designate the differences between rotational constants in excited and ground states (e.g.  $A' - A'' = \Delta A$ ). One can calculate the distance between lines of neighbor  $J$  in the same  $K$  series.

$$\nu(J+1) - \nu(J) = 2J\Delta B - 2B'' \quad (2-10)$$

2.  $Q$  branch. In a  $Q$ -branch transition  $\Delta J = 0$ , hence  $J'' = J'$ . Using the same approach we can find

$$\nu = \Delta B(J''+1)J'' + (\Delta A - \Delta B)K^2 + T_{00} \quad (2-11)$$

In a low temperature spectrum the most intense transitions for each  $K$ -structure occur in the lowest  $J''$  state, since these levels have the highest Boltzman population. In each  $K$ -series the minimal  $J''$  equals to  $K$  (whereas  $K$  is the projection of  $J$  on the rotation axe, minimal  $J$  can not be smaller than  $K$ , therefore  $J''_{\min} = K$ ). The frequency of the most intense  $Q$ -branch transition of the same  $K$  series follows from the Equation 2-11.

$$\nu_{\text{peak}} = K^2\Delta A + K\Delta B + T_{00} \quad (2-12)$$

3. R branch. In an  $R$ -branch transitions  $\Delta J = 1$  consequently  $J'' = J' - 1$ .

$$E'/h = B'(J'' + 1)(J'' + 2) + (A' - B')K^2 + T_{00} \quad (2-13)$$

The frequency of the transition can be written as

$$\begin{aligned} \nu &= B'(J'' + 1)(J'' + 2) - B''J''(J'' + 1) + (\Delta A - \Delta B)K^2 + T_{00} \\ &= \Delta B(J'' + 1)J'' + 2B''(J'' + 1) + (\Delta A - \Delta B)K^2 + T_{00} \end{aligned} \quad (2-14)$$

And the distance between lines of neighbor  $J$  and the same  $K$  is

$$\nu(J+1) - \nu(J) = 2(J + 1)\Delta B + 2B'' \quad (2-15)$$

Using this information to express the energetics of the system studied, one can calculate the relevant molecular constants as described in the following section.

## 2.2 Analysis of rotational structure

In order to reproduce an observed spectrum we need seven molecular constants  $A''$ ,  $B''$ ,  $C''$ ,  $A'$ ,  $B'$ ,  $C'$ , and  $T_{00}$ . Centrifugal distortion constants can not be determined because of the low resolution of the rotational structure in the observed spectrum. By assuming  $B'' - C'' = B' - C'$ , the seven constants can be simplified to be  $A''$ ,  $\Delta A$ ,  $B''$ ,  $\Delta B$ ,  $B'' - C''$ , and  $T_{00}$ . For the beginning,  $B''$  is assumed to be equal to  $C''$ , i.e. this molecule is treated as a symmetric top. The initial step of the analysis is a manual fitting as follows. It is based on a comparison between observed and simulated spectra.

- 1)  $T_{00}$  is approximately determined by a position of the spectrum.
- 2)  $\Delta A - \Delta B$  is determined by the line distances on the  $R$  branch.
- 3)  $B''$  is determined by the line distances on the  $P$  branch.
- 4)  $\Delta B$  is determined by examining the expansion of the line distances on the  $P$  branch.

For  $P$ -branch transitions the distances between neighboring lines in region of high  $J$  transitions are larger than that of low  $J$  transitions. The differences are produced by  $\Delta B$ .

- 5)  $T_{00}$  is accurately determined by assignment of the  $Q$  branch.
- 6)  $\Delta B$  and  $\Delta A$  are confirmed by the line distances on the  $Q$  branch.
- 7)  $B''$  is accurately determined by a  $K = 0$  line position on the  $R$  branch.
- 8)  $B'' - C''$  is determined by a line profile of  $K = 0$  and 1 transitions on the  $R$  branch (Figure 2-2).

The  $K = 1$  transition is separated into two line series by the asymmetry of this molecule. The  $K = 0$  transitions and the separated  $K = 1$  transitions make one strong blended profile determined by the asymmetry parameter  $B'' - C''$ .

- 9)  $T_{\text{rot}}$  is determined by the relative intensity between the low  $J$  and high  $J$  transitions on the  $P$  branch.
- 10)  $A''$  is approximately determined by the relative intensity between the low  $K$  and high  $K$  transitions on the  $P$  branch.

This procedure was applied to the low resolution spectra of  $C_6H_4^+$  (line width of  $0.05\text{ cm}^{-1}$ ) recorded using a pulsed-CRD spectrometer (Figure 2-2) [14]. The low resolution techniques are sufficient to provide accurate constants for small molecules, due to the overlapping of the rotational lines. In the present work the high resolution spectra of  $C_6H_4^+$  (line width of  $0.01\text{ cm}^{-1}$ ) was obtained using a cw-CRD spectrometer. All observed transitions were put into the least square fitting routine. Results obtained by Araki and co-workers were used as the initial parameters.

In this fitting there were following relation between rotational structure and molecular constants.

- $\Delta B$  and  $\Delta C$  were assumed to be equal since it was impossible to determine them independently in the present resolution.
- Lines from the same  $K$  series on the  $P$  or  $R$  branch improved  $T_{00}$ ,  $B''$ , and  $\Delta B$ .
- Additional lines from another  $K$  series improved  $T_{00}$ ,  $B''$ ,  $\Delta B$ , and  $\Delta A$ .
- High  $J$  lines of  $K = 1$  series, which are split due to the asymmetry of the molecule, improved  $T_{00}$ ,  $B''$ ,  $\Delta B$ ,  $\Delta A$ , and  $C''$ .

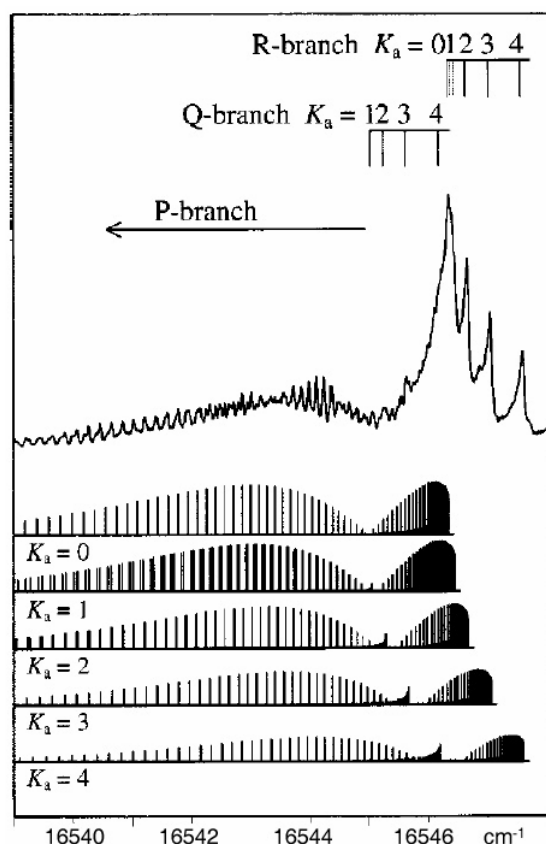
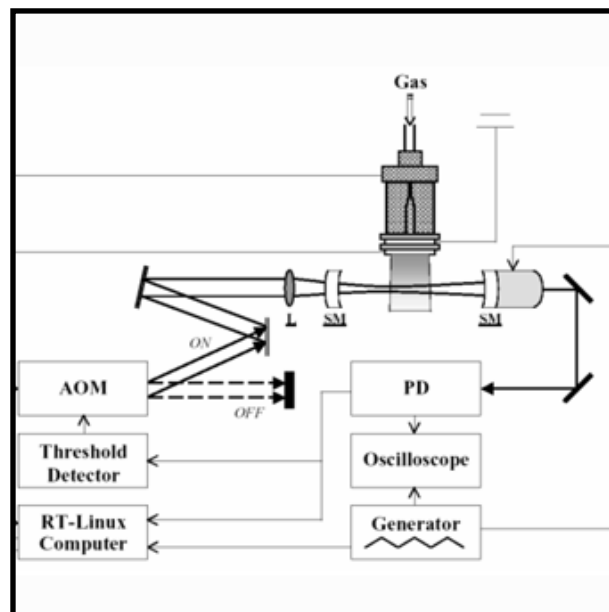


**Figure 2-2.** Spectrum of a near prolate asymmetric-top molecule,  $C_6H_4^+$ . The stick diagrams illustrate the each individual  $K_a$  components. Adapted from [14].



# 3

# Experiment







## 3.1 Principle of CRD spectroscopy

In 1988 O'Keefe and Deacon developed a new method to perform optical absorption measurements: cavity ring down spectroscopy [19]. Their technique was based on the measurement of the rate of absorption rather than the magnitude of absorption, and they obtained sensitivities which were significantly greater than those obtained with conventional absorption spectroscopy. This CRD technique has since been applied in a wide spectral range, from UV to IR, using both pulsed and cw light sources.

In practice, a pulse of laser light is injected into an optical cavity that is formed by a pair of highly reflective mirrors. The small amount of light that is now trapped inside the cavity reflects back and forth between the two mirrors, with a small fraction transmitting through each mirror with each pass. The resultant transmission of the circulating light is monitored at the output mirror as a function of time and allows the decay time of the cavity to be determined. The time required for the cavity to decay to  $1/e$  of the initial output pulse is called the ring down time ( $\tau$ ). The apparatus is converted to a sensitive absorption spectrometer by simply placing an absorbing medium between the two mirrors and recording the frequency dependent ring down time of the cavity. Ideally the ring down time is a function of only the mirror reflectivities, cavity dimensions, and sample absorption.

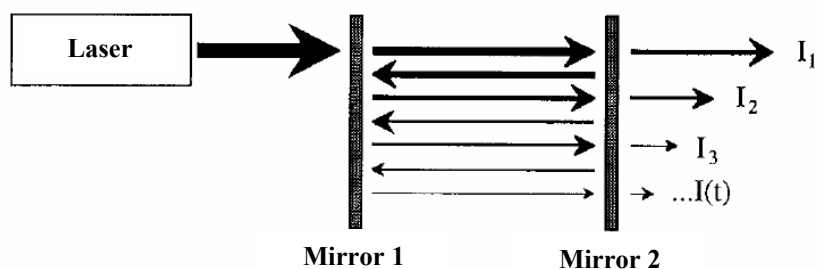


**Figure 3-1.** First-order picture of the cavity decay. Because the laser light is incoherent over the dimensions of the cavity, the light acts like a particle as it bounces back and forth between the mirrors. The intensity monitored at the output mirror is therefore simply a function of the single pass transmission coefficient of the cavity [20].

Traditional absorption spectroscopy measurements determine the attenuation of a light beam passed through a sample and measure absorption coefficients from the ratio of intensities of the light exiting and entering the sample container via the Beer-Lambert law. As such, these methods must measure a small change in a large intensity

### 3. Experiment

---

and hence require very stable light sources with small intensity fluctuations over time. The approach used in a CRD experiment differs because the quantity determined experimentally is the rate of decay of the light intensity within the cavity, and hence CRD is much less sensitive to variations in the laser pulse intensity.

As a first consideration for an empty cavity bounded by two mirrors of high reflectivity ( $R > 99.99\%$ ), separated by a distance  $l$ , the light intensity exiting the cavity will decay with an exponential time profile according to

$$I(t) = I_0 e^{-t/\tau} \quad (3-1)$$

where

$$\tau = [c(1 - R)]^{-1} \quad (3-2)$$

and  $c$  is the speed of light.

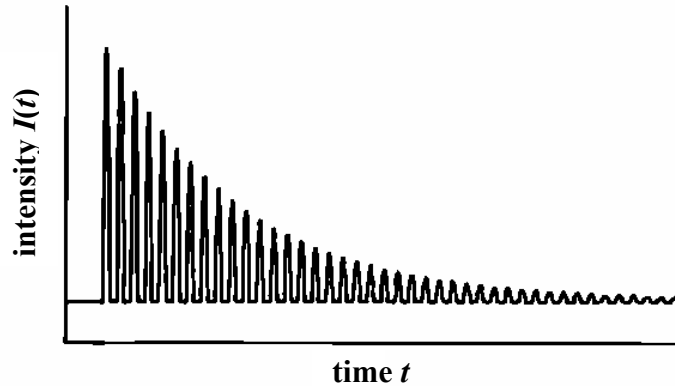


**Figure 3-2.** In the short pulse limit, discrete pulses of laser light leak out of the cavity with each pass. The intensity envelope of the resultant decay is approximated by a smooth exponential expression [20].

Cavity losses by mirror transmission and other processes, such as diffraction and scattering, are equal to  $1 - R$ . The empty cavity  $\tau$  is thus determined by these loss processes, and depends strongly on the reflectivity of the mirrors. For a cavity bounded by two mirrors of reflectivity  $R$ , the number of round trips,  $N$ , performed in the time taken for the intensity to fall to  $1/e$  of its initial value (i.e.  $t = \tau$ ) is obtained by solving

$$R^{2N} = 1/e \quad (3-3)$$

Thus for a mirror reflectivity of 0.999,  $N = 500$ , whereas for  $R = 0.999\ 99$ ,  $N = 50\ 000$ , giving a path length of 100 km for a 1 m cavity. The extreme sensitivity of CRD spectroscopy is, in part, a consequence of these very long path lengths for the probe light through a sample.

If the wavelength of the light within the cavity matches an absorption of a sample gas held between the mirrors, then there will be an additional mechanism for loss of light from the cavity. This, in turn, will increase the decay of the trapped light intensity. For absorption conditions corresponding to Beer-Lambert law behavior, the decay of the light intensity will still be exponential, with time dependence given by

$$I(t) = I_0 e^{-t/\tau - \alpha ct} \quad (3-4)$$

Here  $\alpha$  is the molecular absorption coefficient (with dimensions of length<sup>-1</sup>, and generally quoted in cm<sup>-1</sup>). The product of  $c$  and  $t$  is the path length,  $l$ , over which the absorption is measured. The decay rate is now given by

$$1/\tau' = 1/\tau + c\alpha \quad (3-5)$$

If the empty cavity  $\tau$  is known, measurement of the decay rate of the light intensity as a function of wavelength gives the absorption coefficient for each laser frequency, and hence the absorption spectrum. Spectra can be extracted by directly fitting the exponential decays recorded at each laser wavelength. The time region of the exponential fitted determines the effective path length through the sample. The fit will give the decay time  $\tau'$ .

Extracting spectra depend on the fact that the decay must be a true exponential in order to determine accurate  $\alpha$  values. As was pointed out in Reference [21], care must be taken in any averaging procedure as it is mathematically incorrect to average out shot-to-shot fluctuations by adding a series of exponential decays for multiple laser shots at a particular wavelength and then to fit the resultant decay to obtain an absorption coefficient. The correct procedure must be to fit each decay separately and average the resultant absorption coefficients.

Very high resolution spectroscopy can be obtained by using a single mode cw laser. However, an additional complexity arises from the fact that the spectral overlap between the laser frequency and the frequency of one of the cavity modes is no longer obvious. A build-up of the intracavity field will only take place if the laser frequency and a cavity mode are in resonance, for which there are several ways to proceed.

## 3.2 History of cw-CRD spectrometer

For the measurement of the reflectivity of the cavity mirrors, Anderson et al. used the occasional coincidences of a He-Ne laser with one of the cavity modes [22]. When the light intensity inside the cavity exceeded a predefined threshold, a triggering system switched a Pockels cell that interrupted the laser and started the data acquisition for recording the ring down signal (Figure 3-3). These authors could not tune their laser to obtain absorption spectra, nor did they try to control the occurrence of build-up ring down events. However, this pioneering work is usually not considered as a first demonstration of CRD method. Because the authors were primarily interested in characterizing the reflectivity of mirror coatings and failed to mention the potential use of this technique in spectroscopy.

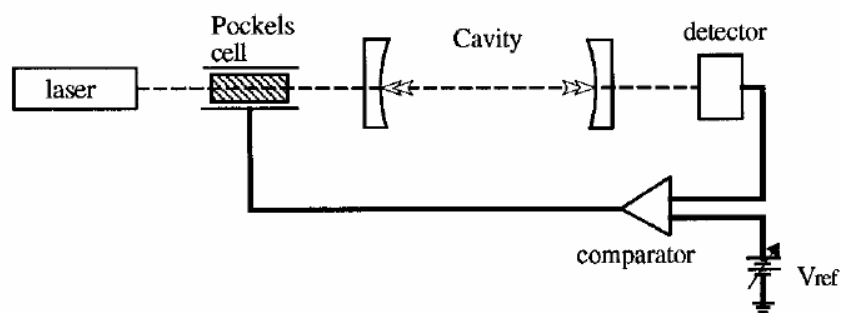


**Figure 3-3.** Mirror reflectometer of Anderson et al.: Instead of measuring the phase shift, the intensity decay of the cavity is measured after the light is quickly shut off with a Pockels cell. Ideally, the modes established in the cavity then undergo a first-order exponential decay [20].

Romanini et al. developed a new approach for measuring cw-CRD absorption spectra [23]. They introduced a regularity into the laser to cavity mode coincidences. The cavity length was piezoelectrically modulated in order to let one of the cavity modes oscillate around the laser line. When the light intensity inside the cavity exceeded a predefined threshold, an acousto-optical modulator turned off the laser beam and a measurement of a ring down decay was obtained. A feedback circuit measured the distance of the position of the mode responsible for the ring down transient with respect to the centre of the modulation range and provided a correction voltage to the piezoelectric transducer (Figure 3-4). In this way they were able to record ring down transients at a range of 200 Hz while the laser was scanned in

wavelength. Unfortunately, in the supersonic jet experiment, this tracking system had problems with sudden fluctuations of the cavity length owing to mechanical vibrations of the pumping system.

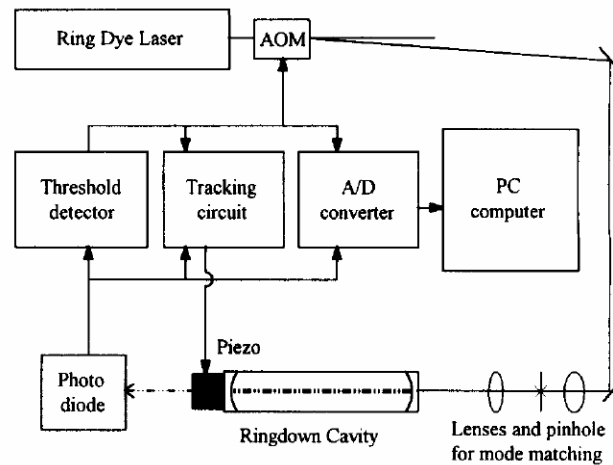


**Figure 3-4.** Cw-CRD set-up of Romanini et al. [23].

According to He et al. the active tracking system is not needed if the modulation of the cavity length is slightly more than one free spectral range and if the modulation speed is not too slow [24]. These authors used a passive scheme approach to match the cavity mode. An acousto-optical modulator switched off a cw near-IR diode laser. One CRD mirror was mounted on a piezoelectric transducer which allow the cavity length to be matched to the laser frequency by wobbling the cavity length slightly over one free spectral range. During each wobble period the cavity would twice reach resonance with the laser frequency. The resonance condition generated a maximum of transmitted intensity after the cavity, which triggered the acousto-optical switch and the data acquisition. Based on this work, Hippler and Quack reported the first implementation of cw-CRD set-up with pulsed jet expansions [25]. In their experiment the cavity was mode matched to the laser wavelength during the gas pulses to achieve highest resolution and lowest noise level (Figure 3-5).

### 3. Experiment

---

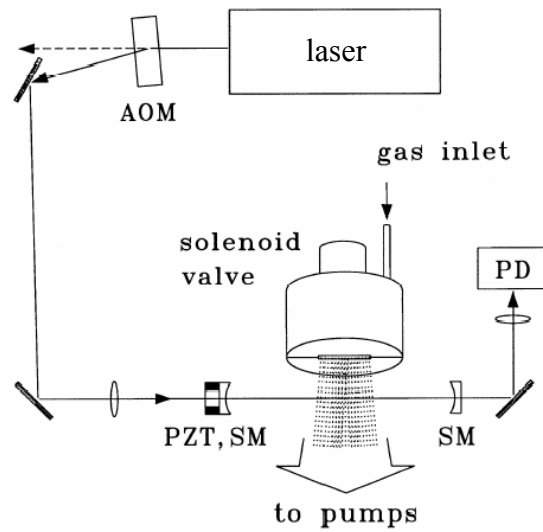


**Figure 3-5.** Experimental set-up of Hippler and Quack [25].

### 3.3 Experimental set-up of the cw-CRD spectrometer

This thesis concerns the high resolution spectroscopy of carbon chains in gas phase. These unstable species are produced in supersonic planar plasma expansion. Based on the work of Hippler and Quack; cw-CRD spectrometer was developed and used in conjunction with a previously built ion source [26, 27].

Figure 3-6 gives general overview of the present experiment. The light source is a single mode continuous wave ring dye laser (COHERENT 899-AUTOSCAN), pumped by a 6 W solid state laser (COHERENT Verdi V-10). The detailed description can be found in an Appendix. The laser beam is guided through an acousto-optical modulator (AOM). The first order deflection is focused into the ring down cavity via a lens where it crosses the planar plasma expansion several mm downstream from the source. The two CRD mirrors (1 m plano/convex,  $R > 99.99\%$ ) are mounted in a mechanically stable holder and separated by a distance of 32 cm.

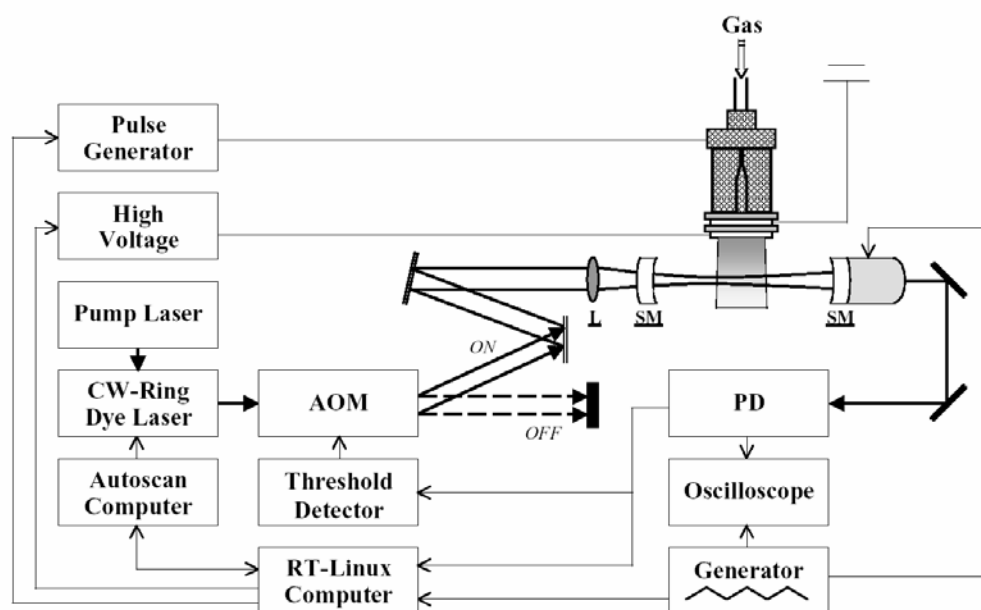


Figure 3-6. Schematic representation of the cw-CRD spectrometer [26].

A strong transmission occurs only when cavity and laser wavelength are mode matched. The cavity length is modulated by moving one of the mirrors mounted on the piezo element. The amplitude of translation is chosen in such a way that it corresponds to at least two free spectral ranges of the laser frequency, i.e. the cavity is

### 3. Experiment

at least four times in resonance with the laser during one period (Figure 3-7). A resonance results in a maximum of transmitted light intensity after the cavity. This transmission is monitored via a Si-photodiode. The AOM is triggered off when the intensity reaches a certain threshold; this process interrupts the laser beam and a ring down event is initiated.

The following detection scheme is used to guarantee that plasma pulse and ring down event coincide (Figure 3-7). The data acquisition programme chooses the first resonance on the ascending voltage ramp as the trigger signal. The program defines a delay at which gas and discharge pulses are activated. When the next ring down event occurs, it automatically samples the plasma. Only every second cycle is used to trigger gas and discharge pulses. The plasma free ring down event is then used for background subtraction.

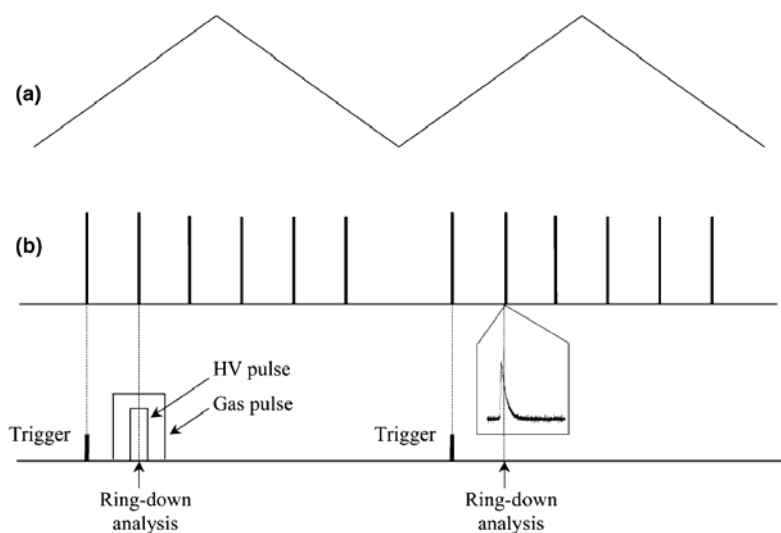


**Figure 3-7.** Relative timing of the piezo ramp voltage, cavity resonances, valve opening, and high voltage pulse applied to the slit electrodes. (a) Ramp voltage applied to the piezo. (b) Signal from the photodiode [27].

The complete decay curve is fitted to an exponential defining  $\tau$ . The CRD spectrum is obtained by recording  $(1/\tau_{\text{plasma}} - 1/\tau_{\text{reference}})$  while scanning the laser. Typical ring down times are  $\tau = 27 \mu\text{s}$ . This is equivalent to approximately 25000 passes through the plasma or an effective absorption path length of 760 m. The observed spectra are calibrated by simultaneous recording  $\text{I}_2$  absorption in a cell. Although the resolution of the laser is 500 kHz, the spectra of  $\text{C}_6\text{H}_4^+$ , for example, show a line width of  $0.01 \text{ cm}^{-1}$ . This is due to Doppler broadening in the planar discharge as well as life time shortening in the excited electronic state of  $\text{C}_6\text{H}_4^+$  (see Chapter 4).



## 3.4 Ion source

In 1951, Kantrowitz and Grey suggested using high pressure gas in front of wide slit as a method to produce a molecular beam [28]. Under these conditions

$$d \gg \lambda_0 \quad (3-6)$$

where  $d$  is the width of the hole and  $\lambda_0$  the mean free path between collisions. For a usual  $d$  (about 40-100  $\mu\text{m}$ ) and a pressure of some atmospheres numerous collisions take place beyond the nozzle which convert the random particle motion into a directional flow. As a result the velocity range is reduced and the translational temperature of the beam becomes extremely low. Every travelling particle in the beam has a slow velocity relative to its neighbours and collisions are very rare. Inside the supersonic molecular beam the motion of the atoms and molecules is parallel. As a result, an observation in the perpendicular direction yields spectra with minimal Doppler broadening. The first spectra obtained in this way using direct absorption technique were reported by Travis and co-workers in 1977 [29].

The word “supersonic” means that the particles have a very high Mach number (about 100). The Mach number is defined as

$$M = u/a \quad (3-7)$$

where  $u$  is the flow velocity and  $a$  is the speed of sound.

For absorption measurements on carbon chain radical cations a precursor gas like acetylene or cyanogen is diluted in He, Ne or Ar and discharged in the throat of the slit nozzle. Strong pumping is required to limit the background pressure in the vacuum chamber to roughly 1 mbar during jet operation.

Translational energy levels are situated very close to each other. This makes the energy transfer from precursor to carrier gas very efficient and the translational temperature is reduced to less than 1 K. The rotational energy levels are further apart and therefore only cooled down to about 15 K. The low temperature concentrates the particles in a few low lying rotational and vibrational states making lower lying transitions more intensive.

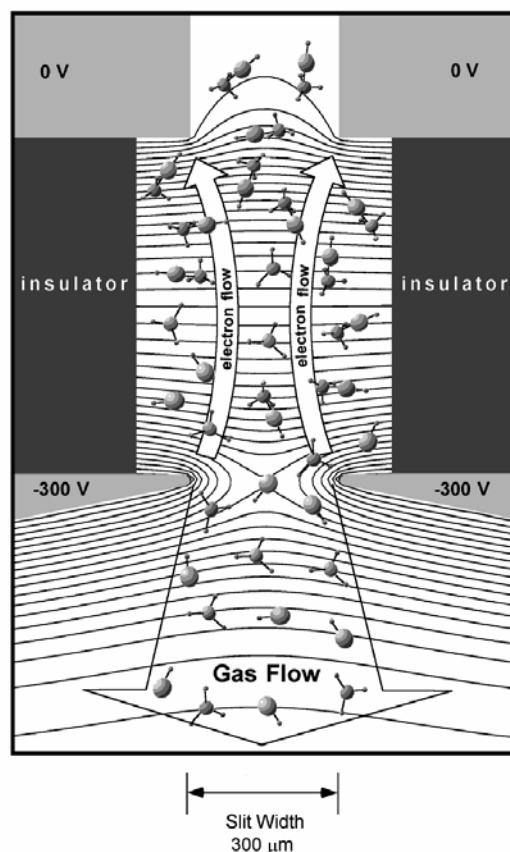
A further useful modification of the jet is to use it with a pulsed outlet. This has a few advantages. Firstly, less sample is used and the size of the nozzle can be enlarged, increasing the molecular density in each pulse. Secondly, pumping capacity can be decreased. Pulsed nozzle sources provide gas densities several orders of

### 3. Experiment

---

magnitude higher than the continuous jet sources [30, 31]. Further improvements by Lovejoy and Nesbitt in 1987 include both increased sensitivity and resolution of the absorption method through the use of a pulsed slit nozzle without discharge to detect neutral hydrogen-bonded complexes [32]. Since then new nozzles have been developed which combine slit jet properties with electric discharges [33, 34]. Applying a high voltage during the gas pulse results in an intense glow discharge strongly localized behind the mouth of the slit supersonic expansion. Transient species created in this source are subsequently cooled and probed via direct absorption by the laser.

Davis and co-workers pointed out several key advantages of this slit discharge design for the direct absorption study of radicals [33]. First of all, the discharge is effectively confined to the region upstream of the slit expansion orifice, as shown in a detailed cross sectional view of the slit discharge in Figure 3-8. From electrostatic modeling of the potentials, the expansion occurs in a field free region that permits efficient supersonic cooling to take place. This cooling concentrates population in the lowest quantum states and therefore substantially enhances the sensitivity of direct absorption methods. Secondly, these high radical densities are geometrically concentrated along the probe laser axis to provide direct absorption path lengths of up to 100 cm. Thirdly, the density of species in a slit falls off more slowly with distance ( $\sim 1/R$ ) than for a pinhole expansion ( $\sim 1/R^2$ ), thus the slit expansion environment provides more cooling collisions with which to equilibrate vibration–rotation–translational degrees of freedom. Finally, the slit expansion collisionally collimates the component of translational velocity parallel to the laser probe axis, thereby compressing the Doppler width by as much as 5–20 fold over that of an unskimmed pinhole expansion geometry. Since this velocity compression conserves the total number of molecules in the probe region, detection sensitivity at line center is correspondingly enhanced, as well as providing substantially sub-Doppler resolution in an unskimmed expansion.



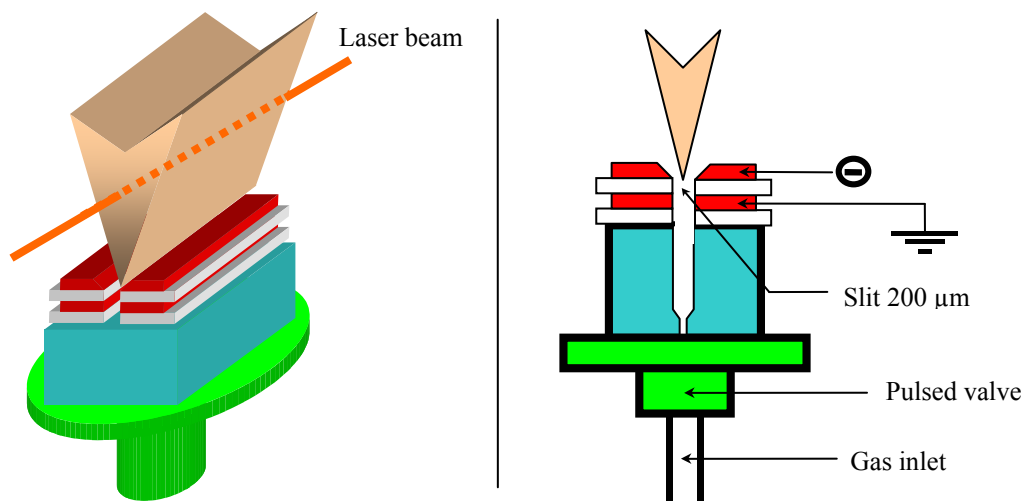
**Figure 3-8.** Detailed cross sectional view of the slit discharge radical source [33].

Figure 3-9 shows the pulsed slit nozzle/electrode assembly in the present spectrometer. It is similar to one described in Reference [34]. This assembly consists of a cathode made of two stainless steel jaws forming a slit ( $30 \text{ mm} \times 200 \text{ }\mu\text{m}$ ,  $60^\circ$  exit angle). The anode is a metal plate electrically insulated from the cathode by a ceramic spacer. The assembly is attached by insulated screws to the top of a metal body. The volume inside the body has been kept as small as possible; this allows the length of the final gas pulse through the slit to be as close as possible to the initial opening time of the pulsed valve. The pulsed valve is mounted on top of the slit nozzle body and controls the gas flow into the system through a short circular channel. A small reservoir in front of the valve operates as gas buffer zone and guarantees a stable gas flow into the slit nozzle. A backing pressure of 10 bars is used. The pressure in the vacuum set-up is computer controlled and kept constant ( $0.17 \text{ mbar}$ ) during jet operation by adjusting the pulse length of the valve. This procedure significantly reduces fluctuations in the radical production. A pulsed negative voltage of  $-500 \text{ V}$  is applied to both jaws via two separate  $4 \text{ k}\Omega$  ballast resistors. The inner metal plate is grounded while the body floats. The latter is

### 3. Experiment

---

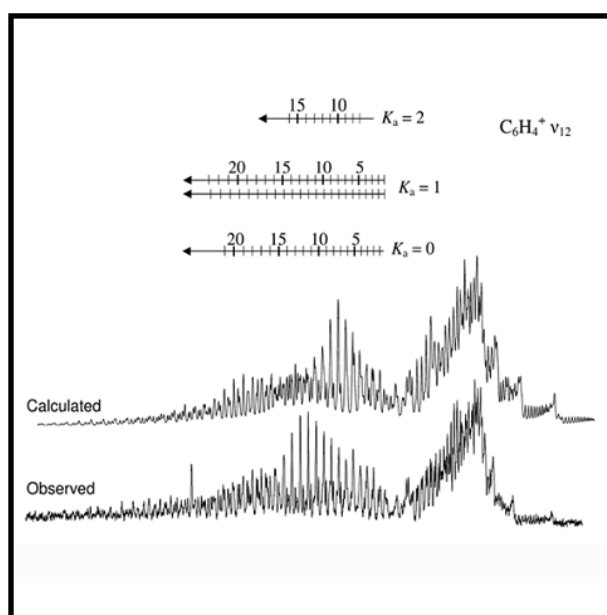
important in order to shield the pulsed valve from internal high voltage arcing. A discharge through the gas mixture of 0.2% acetylene in helium is used to produce the carbon chains. Rotational temperatures of the order 15-40 K are routinely obtained.



**Figure 3-9.** Pulsed slit nozzle/electrode assembly.

# 4

## Spectroscopic results





## 4.1 Origin band<sup>1</sup>

The 604 nm origin band in the  ${}^2A''-X\,{}^2A''$  electronic transition of  $C_6H_4^+$  was observed previously at  $0.05\text{ cm}^{-1}$  resolution [14]. While *P*-branch region of this band included a lot of unblended lines, the *R* branch was not rotationally resolved; only turning points of different *K*-components were present in the spectrum (Figure 4-1).

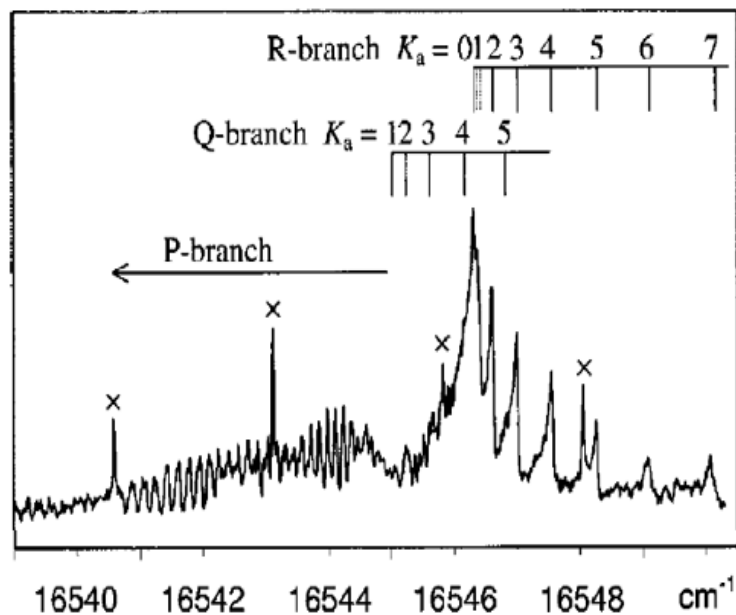


**Figure 4-1.** Spectrum of  $C_6H_4^+$  observed at 604 nm using pulsed CRD spectroscopy through a supersonic planar plasma expansion. Lines marked  $\times$  are due to another carrier [14].

In order to determine more accurate rotational constants, the *R*-branch region was re-measured using a resolution of  $0.01\text{ cm}^{-1}$ . More than 40 rotational lines were recorded and the observed spectrum is shown in Figure 4-2 (lower trace). The assignment is based on the constants given in [14]. The analysis is described in Chapter 2. It was carried out using a conventional Hamiltonian for an asymmetric top molecule where the energy levels were calculated by direct numerical diagonalisation of Hamiltonian matrices and molecular parameters were determined by a least-square fit to the observed line frequencies. The ground state rotational constant  $A''$  was fixed to the value deduced in [14], because it could not be determined from the observed *a*-type transitions.

<sup>1</sup> This chapter is taken from the article published in: D. Khoroshev *et. al.*, *J. Mol. Spec.* 227 (2004) 81

## 4. Spectroscopic results

The rotational constant differences between the ground and excited state,  $\Delta B$  and  $\Delta C$ , which cannot be computed independently from the present data, were assumed to be equal. The measured line frequencies and their assignments are given in the Appendix, and the constants are inferred in Table 4-1. A rotational-profile simulation program WANG [35] reproduced well the observed spectrum as shown in Figure 4-2 (upper trace).

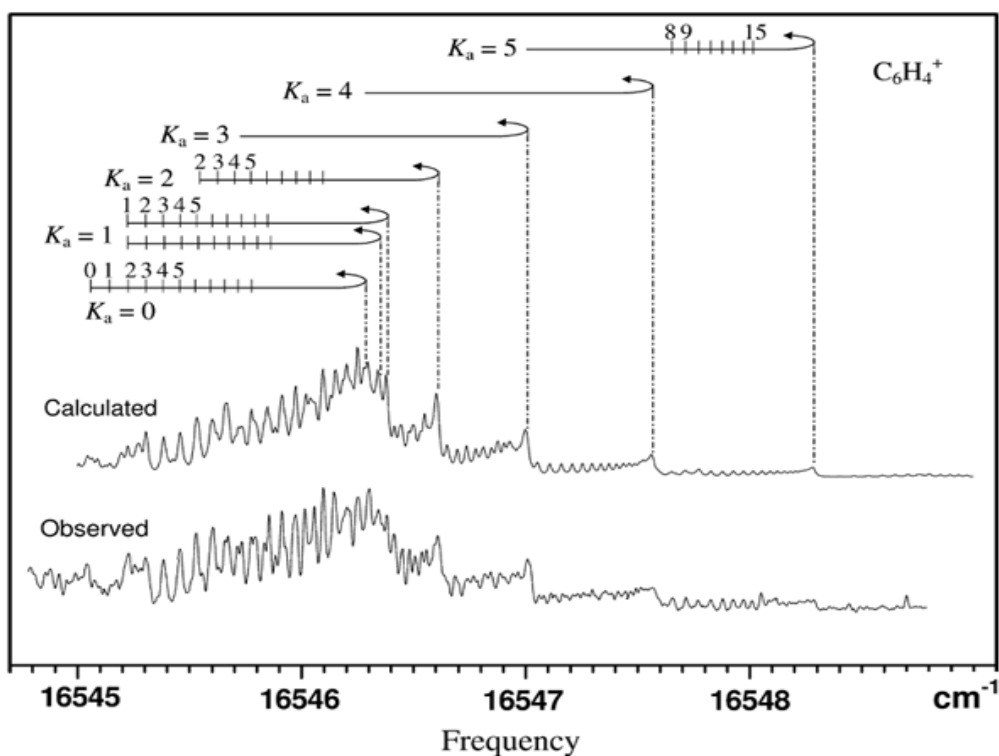


**Figure 4-2.** The rotationally resolved electronic absorption spectra of the origin band in the  $2A'' - X^2A''$  transition for  $C_6H_4^+$  and the simulated rotational structure at 20 K.

Asymmetry of a near prolate top molecule can be expressed by  $B - C$ , which is obtained mainly from the asymmetry splitting of a  $K_a = 1$  series in the  $R$  branch. However, the separation was not resolved for transition having  $J \leq 15$ . Both components were assigned to one line: for instance the  $J_{K_a K_c} = 16_1 16 - 15_1 15$  and  $16_1 15 - 15_1 14$  transitions were assigned to the  $16546.0966 \text{ cm}^{-1}$  peak (Appendix). Thus, the difference  $B - C$  will be underestimated by the least-squares fit and the obtained value ( $= 0.0011 \text{ cm}^{-1}$ ) is smaller than that obtained from *ab initio* calculation (CASSCF/cc-pVTZ,  $0.0016 \text{ cm}^{-1}$ ). An average,  $\frac{1}{2}(B + C)$ , of the two constants was determined accurately from the present data and agrees well with the previous report [14] but with increased accuracy. Frequencies of the pure rotational transitions in the millimeter region can be adequately predicted by the rotational constant  $\frac{1}{2}(B + C)$ .



Table 4-1. Molecular constants for  $C_6H_4^+$  and  $C_6D_4^+$  ( $cm^{-1}$ )

	$C_6H_4^+$			$C_6D_4^+$			
	604 nm	581 nm	Ref. [14]	Calc. <sup>b</sup>	581 nm	Ref. [1]	Calc. <sup>b</sup>
Ground state $X^2A''$	$A''$	1.24 <sup>c</sup>	1.24	1.271	0.89 <sup>c</sup>	0.89	0.923
	$B''$	0.046481(149)	0.0467	0.0466	0.04281(97)	0.0416	0.0415
	$C''$	0.045349(145)	0.0449	0.0450	0.04061(97)	0.0400	0.0397
	$\frac{1}{2}(B'' + C'')$	0.045915(147)			0.04171(97)		
Excited state $^2A''$	$\Delta A$	0.078274(50)	0.0767	0.080		0.0450	0.047
	$\Delta\frac{1}{2}(B + C)$	-0.0014519(72)	-0.0015	-0.0011		-0.0013	-0.010
	$T_{00}$	16544.96879(196) <sup>d</sup>	16544.980			16611.91	
$\nu_{12} = 1$	$\Delta A$	0.07602(82)			0.04665(63)		
	$\Delta\frac{1}{2}(B + C)$	-0.0014613(151)			-0.001444(79)		
	$T_{10}$	17213.7228(22) <sup>d</sup>			17218.1664(118) <sup>d</sup>		
$\nu$	$\nu$	668.7540(42)			606.26		
rms	rms	0.0046			0.0066		

<sup>a</sup> Values in parentheses denote the standard deviation and apply to the last digits of the constants.

<sup>b</sup> Calculated with CASSCF/cc-pVTZ.

<sup>c</sup> Fixed to the value of [14]

<sup>d</sup> The error is from the least-squares fitting, and uncertainty of the calibration is  $0.007 cm^{-1}$ .

## 4.2 Vibrationally excited band

An absorption band observed at 585.3 (584.7) nm following mass-selection of  $C_6H_4^+$  ( $C_6D_4^+$ ) in a 6 K neon matrix was assumed to belong to another isomer of  $C_6H_4^+$  because of difference in the band profile compared to the origin band (Figure 4-3).

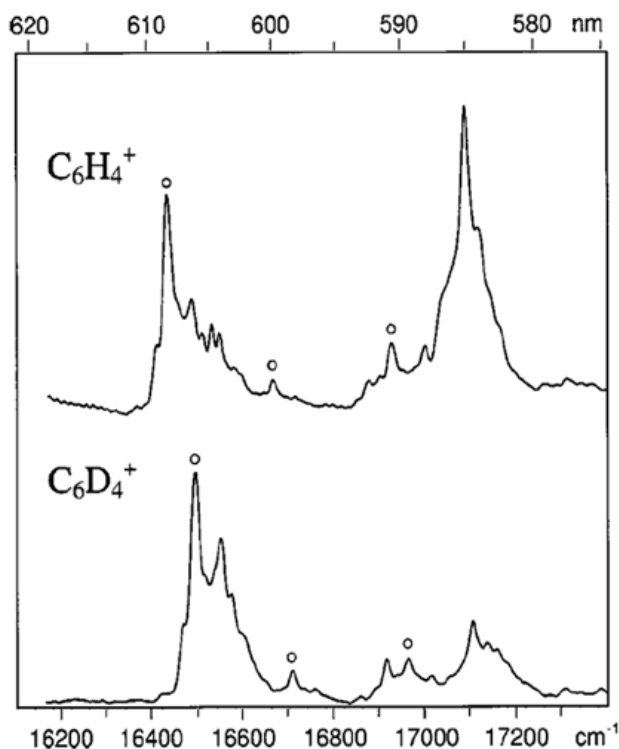


**Figure 4-3.** Electronic absorption spectra of  $C_6H_4^+$  (upper trace) and  $C_6D_4^+$  (lower trace) measured in 6 K matrices after codeposition of mass-selected cations with excess of neon. The bands at 609 nm of  $C_6H_4^+$  and at 606 nm of  $C_6D_4^+$  correspond to the observed gas-phase spectra. The weaker bands at 600 and 591 nm for  $C_6H_4^+$  and 599 and 590 for  $C_6D_4^+$  (indicated by  $\circ$ ) exhibit an identical chemical behavior as the 609 nm band on  $C_6H_4^+$  and the 606 nm band on  $C_6D_4^+$  and are due to transitions to vibrationally excited levels in the upper  ${}^2A''$  state. The bands at 585.3 and 584.7 nm of  $C_6H_4^+$  and  $C_6D_4^+$  are due to another isomer [14].

In order to identify the carrier this wavelength region was scanned with both normal and deuterated precursors using the cw-CRD spectrometer. As result rotationally resolved bands were observed in the 581 nm region (Figures 4-4 and 4-5). However a complete reproduction of the rotational structure did not prove possible using an asymmetric-top Hamiltonian as for the 604 nm band. The spectrum could only be analysed for  $K_a = 0, 1, 2$  transitions in the  $P$  branch. The assignments are given in the Appendix and the molecular constants in Table 4-1. The observed turning

points in the *R* branch could not be reproduced by the simulations. This may be caused by Fermi and Coriolis interactions [36].

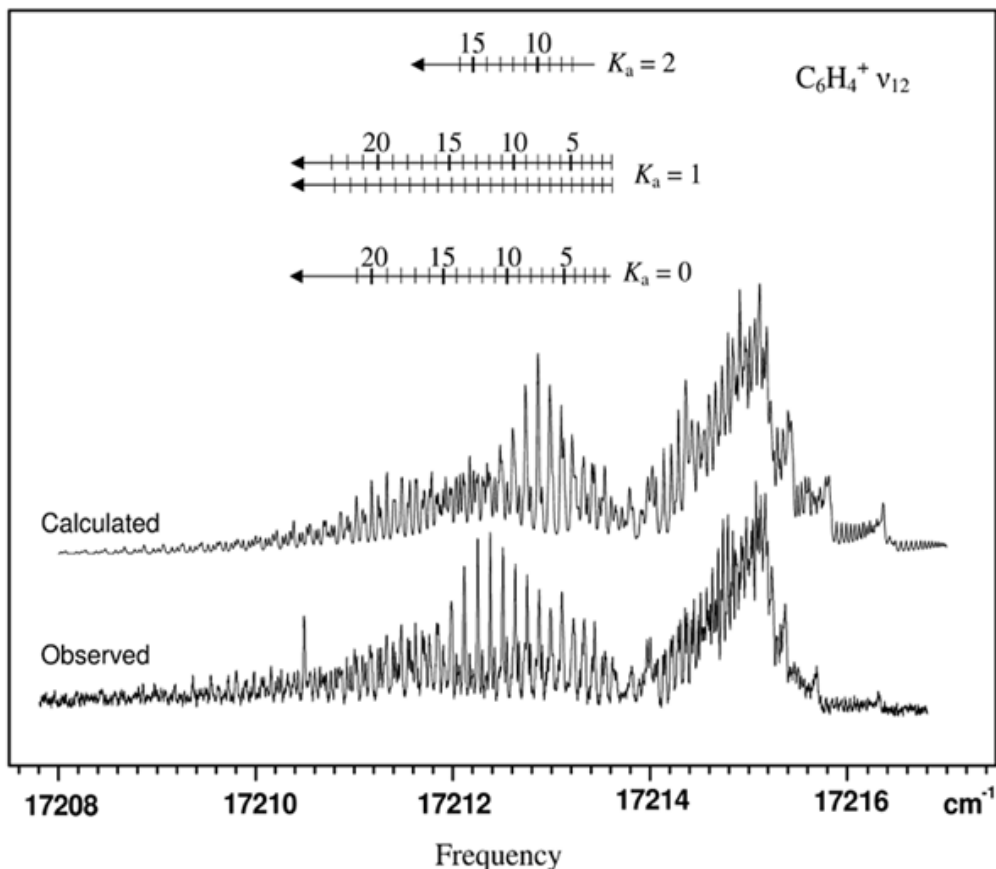


**Figure 4-4.** The rotationally resolved electronic absorption spectra of the 581 nm band in the  ${}^2A''(v_{12}=1) - X^2A''(v=0)$  transition for  $C_6H_4^+$  and the simulated rotational structure at 20 K.

It was considered if the 581 nm band could be the origin of another isomer of  $C_6H_4^+$ . In this case the shift of the transition energy for the fully deuterated species should be approximately equal to that of  $C_6H_4^+/C_6D_4^+$  ( $66.94\text{ cm}^{-1}$ ). However, the shift observed on deuteration is only  $4.4\text{ cm}^{-1}$ , and thus excludes this possibility. Rather, these results suggest that this band is a transition to a vibrationally excited level of a  $C_6H_4^+$  isomer. The rotational constants of a *trans*- $H-C\equiv C-CH=CH-C\equiv CH^+$  isomer, which could be a candidate due to similarity of the structure with that of the 604 nm band, were calculated to be  $A = 1.451$ ,  $B = 0.0489$ , and  $C = 0.0473\text{ cm}^{-1}$  (B3LYP/cc-pVTZ, Gaussian 03 [37]). These are not in agreement with the deduced constants (Table 4-1). On the other hand, the *B* and *C* constants inferred for the ground state agree within the errors of the fit to those from the analysis of 604 nm band. Therefore the 581 nm band is assigned to a transition from the ground state to vibrationally excited level of  $C_6H_4^+$  of the  ${}^2A''-X^2A''$  system.

## 4. Spectroscopic results

The 585.3 nm peak in the matrix spectrum (Figure 4-3) is thus an overlap of the transition observed at 581 nm in the gas phase and that of another isomer, because the site structure is not the same as on the origin band (at 609 nm in neon). This isomer was not detected in the present work presumably because the discharge sources used in the two experiments are quite different.

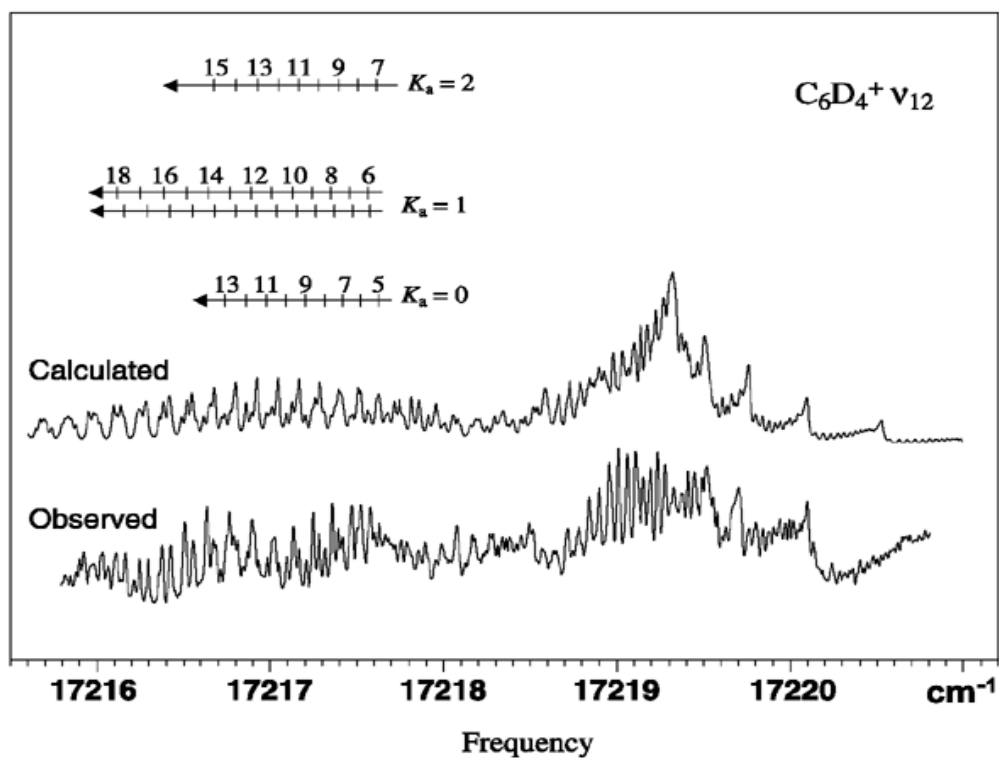


**Figure 4-5.** The rotationally resolved electronic absorption spectra of the 581 nm band in the  ${}^2A''(v_{12}=1) - X^2A''(v=0)$  transition for  $C_6D_4^+$  and the simulated rotational structure at 20K.

## 4.3 *Ab initio* calculations

To assign the vibration excited in the upper electronic state *ab initio* calculations were carried out using MOLPRO [38]. At first the adiabatic transition energies of the  ${}^2A''-X\ {}^2A''$  transition of  $C_6H_4^+$  ( $H-C\equiv C-C\equiv C-CH=CH_2^+$ ), using optimized geometry, were computed to be 2.18 and 1.95 eV using CASSCF and RS2C (CASPT2) method respectively, with the cc-pVTZ basis sets. The calculated values are in good agreement with the experiment, 2.05 eV. Subsequently the vibrational frequencies of the normal modes of  $C_6H_4^+$  and  $C_6D_4^+$  in the  ${}^2A''$  excited state were calculated using a simpler CASSCF method (Table 4-2).

**Table 4-2.** Calculated and observed vibrational frequencies ( $cm^{-1}$ ) in the ground  $X\ {}^2A''$  and excited  ${}^2A''$  state of  $C_6H_4^+$  and  $C_6D_4^+$ <sup>a</sup>

Mode	Symmetry	$C_6H_4^+$				$C_6D_4^+$			
		$X\ {}^2A''$		${}^2A''$		$X\ {}^2A''$		${}^2A''$	
		$\omega_{Calc.}$	Intensity <sup>b</sup>	$\nu_{Obs.}$	$\omega_{Calc.}$	$\omega_{Calc.}$	Intensity <sup>b</sup>	$\nu_{Obs.}$	$\omega_{Calc.}$
17	<i>a'</i>	98	0.0		97	90	0.0	90	
24	<i>a''</i>	136	0.0		131	122	0.0	118	
16	<i>a'</i>	219	0.1	232.3 <sup>c</sup>	222	207	0.2	211	
23	<i>a''</i>	304	0.0		349	271	0.0	300	
15	<i>a'</i>	434	0.1		430	423	0.3	424	
22	<i>a''</i>	489	0.4		457	434	0.2	429	
14	<i>a'</i>	503	2.1	493.7 <sup>c</sup>	496	471	1.4	464	
21	<i>a''</i>	621	0.0		548	564	0.1	480	
13	<i>a'</i>	631	2.2		591	490	1.0	451	
20	<i>a''</i>	709	1.5		486	557	0.9	373	
12	<i>a'</i>	731	2.2	668.8	714	667	2.9	606.3	
19	<i>a''</i>	1000	1.6		933	770	0.7	718	
11	<i>a'</i>	1111	1.1		1058	892	0.4	863	
18	<i>a''</i>	1165	0.6		1007	954	0.1	853	
10 <sup>d</sup>	<i>a'</i>	1311	3.9		1273	1125	1.2	1107	
9	<i>a'</i>	1361	11.9		1222	1077	1.3	1055	
8 <sup>d</sup>	<i>a'</i>	1566	11.3		1533	1526	36.7	1390	
7 <sup>d</sup>	<i>a'</i>	1648	17.8		1612	1323	5.8	1236	
6	<i>a'</i>	2119	33.7		1989	2013	48.0	1935	
5	<i>a'</i>	2258	100.0		2208	2250	100.0	2177	
4	<i>a'</i>	3313	1.0		3320	2409	1.3	2407	
3	<i>a'</i>	3339	0.5		3337	2471	1.8	2465	
2	<i>a'</i>	3429	0.6		3443	2559	0.2	2570	
1	<i>a'</i>	3575	4.4		3558	2741	1.6	2699	

<sup>a</sup> Using CASSCF/cc-pVTZ.

<sup>b</sup> Relative infrared intensity.

<sup>c</sup> Neon-matrix data in [14]

<sup>d</sup> The three modes are mixed.

To assign the vibrational excitation associated with the 581 nm band, both the frequency and their ratio for  $C_6H_4^+$  and  $C_6D_4^+$  were used as indicated in Figure 4-6. The electronic transitions observed in the absorption spectrum in a neon matrix, 600 (599) and 591 (590) nm in  $C_6H_4^+$  ( $C_6D_4^+$ ), and the 581 nm band observed in the gas phase also plotted in the same figure. The vibrational mode excited in the upper state should have *a'* symmetry due to the selection rules for  ${}^2A''-X\ {}^2A''$  transition. The position of the 581 nm band implies a vibrational frequency of  $668.8\ cm^{-1}$  and agrees

## 4. Spectroscopic results

with the value  $713.6\text{ cm}^{-1}$  calculated for the in-plane bending mode. The two bands observed in the matrix, which correspond to  $232$  and  $494\text{ cm}^{-1}$  frequencies, are also in accord with the  $222$  and  $496\text{ cm}^{-1}$  calculated values and their ratio. Therefore the  $600$  and  $591\text{ nm}$  bands in the matrix and the  $581\text{ nm}$  one in the gas phase can be assigned transitions from the lowest level in the ground state to the upper electronic state involving the excitation of the  $\nu_{16}$ ,  $\nu_{14}$ , and  $\nu_{12}$  vibrational modes, respectively. Additionally, the calculation indicates that several overtones and combination bands can be found around the  $\nu_{12}$  vibrational level:  $\nu_{14} + \nu_{16}$  ( $718\text{ cm}^{-1}$ ),  $\nu_{13} + \nu_{17}$  ( $689$ ),  $2\nu_{23}$  ( $698$ ), and  $\nu_{21} + \nu_{24}$  ( $679$ ), with  $a'$  symmetry and  $\nu_{16} + \nu_{20}$  ( $708$ ) with  $a''$  symmetry. The observed irregular rotational structure of the  $581\text{ nm}$  band may be due to Fermi and Coriolis interactions among such adjacent vibrational levels.

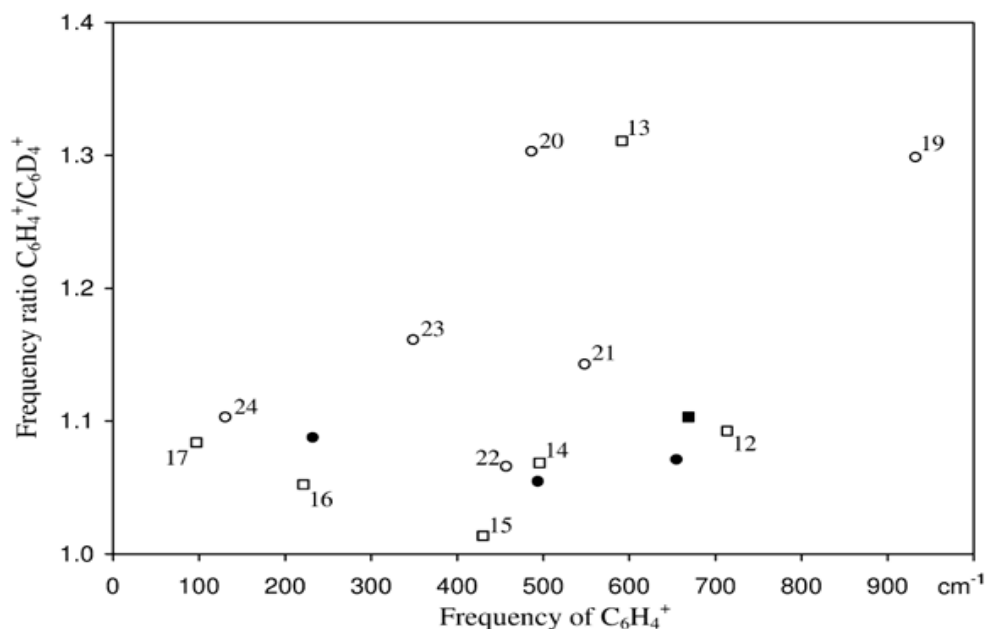
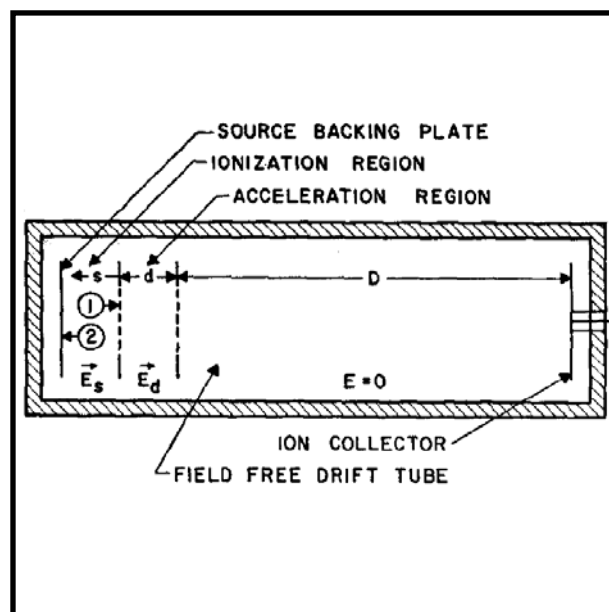


**Figure 4-6.** The calculated frequencies and their ratios  $\omega(C_6H_4^+)/\omega(C_6D_4^+)$  assuming a harmonic potential in the upper  ${}^2A'$  state. The observed values are  $\nu(C_6H_4^+)/\nu(C_6D_4^+)$ . “■” indicates an observed value in gas phase, “●” in neon-matrix, “□” calculated ones with  $a'$  symmetry and “○” calculated ones with  $a''$  symmetry. The numbers attached in the calculated values indicate the vibrational modes as listed in Table 4-2.

Vibrational frequencies, infrared intensities (Table 4-2) and a permanent dipole moment in the ground state were also calculated using the same method and basis set. This may help in the search for the vibrational transitions in the infrared region. The permanent dipole moment in the ground state was calculated to be  $\mu_a = 0.63$  and  $\mu_b = 0.38\text{ D}$ . Thus in the pure rotational spectrum the  $a$ -type transition should be 2.8 times stronger than the  $b$ -type one and suggests that the detection of the  $C_6H_4^+$  is possible.

# 5

## TOF mass spectrometer







## 5.1 Principles of TOF mass spectrometry

The mass spectrometer was built to monitor the molecular components of the plasma discharge. The ion source has been described in Section 3.4. There are several parameters which influence the production of different species: one can vary the gas pressure, applied voltage or concentration of acetylene in helium. Introducing the mass spectrometer can simplify the search of optimal conditions for synthesizing the preferred species.

Time-of-flight (TOF) mass spectrometry is commonly used in conjunction with pulsed ion sources for a few reasons. Particles over a large mass range can be investigated. A complete mass spectrum is generated during a few microseconds and can be obtained for extremely small ion concentrations. There is no need to scan through radio frequencies or voltages to sequentially select certain ions while discarding others. Furthermore, TOF mass spectrometers are inexpensive and easy to build.

The operating principle of a TOF mass spectrometer is that an applied electrical potential, giving all ions the same kinetic energy, propels the ions at different velocities based on their specific mass-to-charge ratios (normally singly charged species are produced). Subsequently, the ions are allowed to drift under no external field and separate as a function of their velocities (masses). The time needed to travel the length of the drift region (the “time-of-flight”) is related to the mass of the ion.

In present studies a linear Wiley-McLaren type TOF mass spectrometer is built. This type spectrometers consist of two acceleration regions (separated by a grid), a drift region, and an ion detector (Figure 5-1). Wiley and McLaren observed that ions of a particular mass-to-charge ratio would reach the detector with a spread in arrival times, due to the effects of uncertainty in their location in the extraction field and their initial kinetic energy, resulting in reduced resolution [39]. They overcome these problems by devising an instrument, incorporating a dual-stage extraction/acceleration region, to compensate for spatial and initial kinetic energy distributions.

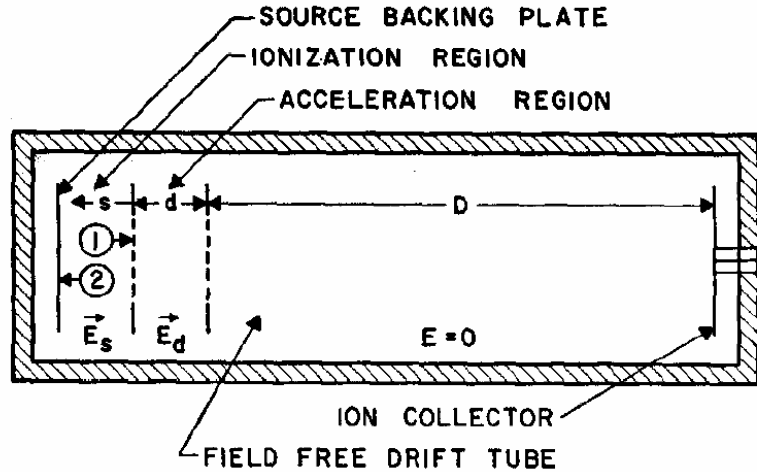


Figure 5-1. Basic geometry of the Wiley-McLaren TOF mass spectrometer [39].

When ions of the same mass with the same initial kinetic energy have different location at the moment of extraction pulse, the ions initially closer to the detector (and thus of smaller  $s$  value, Figure 5-1) will experience a smaller potential gradient and be accelerated to lower kinetic energy, than those which have larger initial  $s$  values. The ions located further from the detector (indicated as “●” in Figure 5-2) will enter the field-free drift region later, but will eventually pass the ions located closer to the detector (indicated as “○” in Figure 5-2) due to having larger velocities. By adjusting the extraction field it is possible to achieve a space focus (SF) plane, where ions of any given mass arrive at the SF plane at the same time. The location of the SF plane is independent of mass, but ions of different masses will arrive at the SF plane at different times (Figure 5-2).

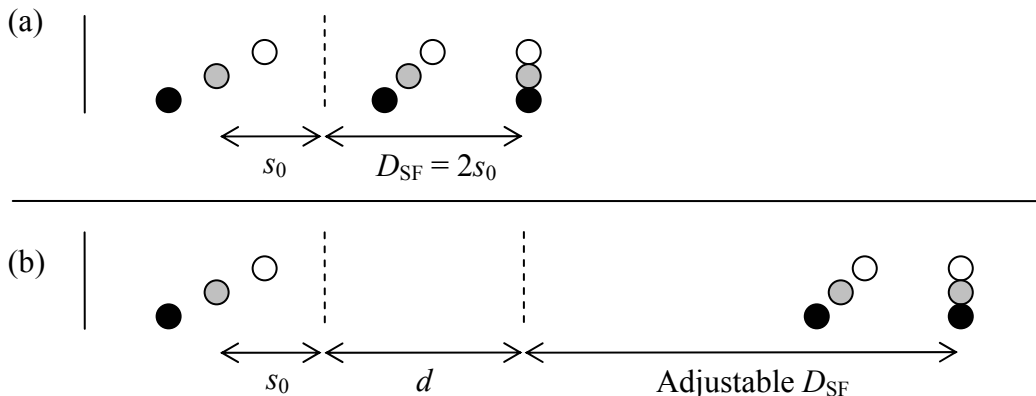


Figure 5-2. Space focus for (a) single-stage and (b) dual-stage TOF. The focus condition for the single-field system is the purely geometric condition,  $D_{SF} = 2s_0$ . In dual-field configuration, position of SF plane depends on the voltage applied to the extraction/acceleration grids.

When ions of the same mass have different initial kinetic energies at the moment of extraction pulse, they will have different final velocities after acceleration and arrive at the detector at different times. The initial kinetic energy distribution also includes ions with the same kinetic energy, but velocities in different directions (ions 1 and 2 in Figure 5-1). These ions will arrive at the detector at different times corresponding to their turn-around time. The resolution of a mass spectrometer can be improved by utilizing longer field-free regions. The longer the drift length ( $D$  in Figure 5-1) increases the magnitude of the time-of-flight. This reduces the effect of turn-around time on resolution.

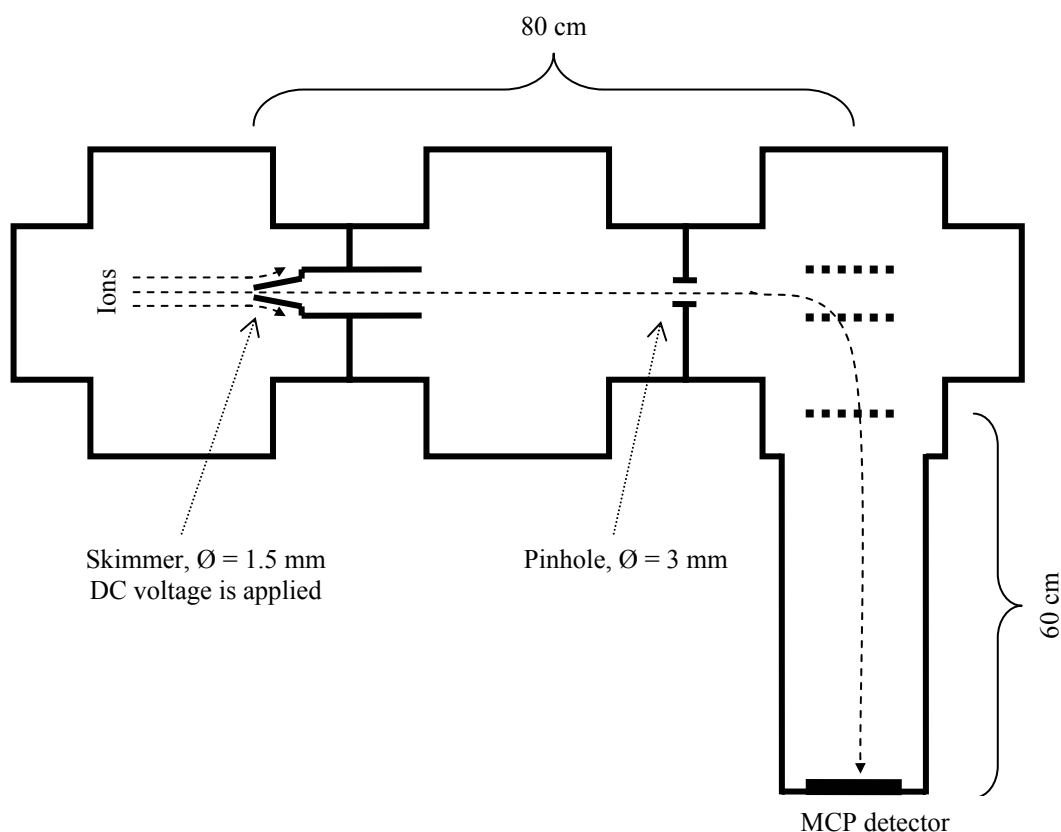
Calibration of the TOF instrument is performed from empirical determination of the times-of-flight of several known masses. Subsequently, a calibration line is drawn, according to

$$m/z = at^2 + bt + c \quad (5-1)$$

where  $m/z$  is the mass-to-charge ratio,  $t$  is the time-of-flight. The calibration constants  $a$ ,  $b$ , and  $c$  are determined through a second order polynomial regression. Any experimental time-of-flight  $t$  can then be converted to a  $m/z$  value to identify the unknown ions.

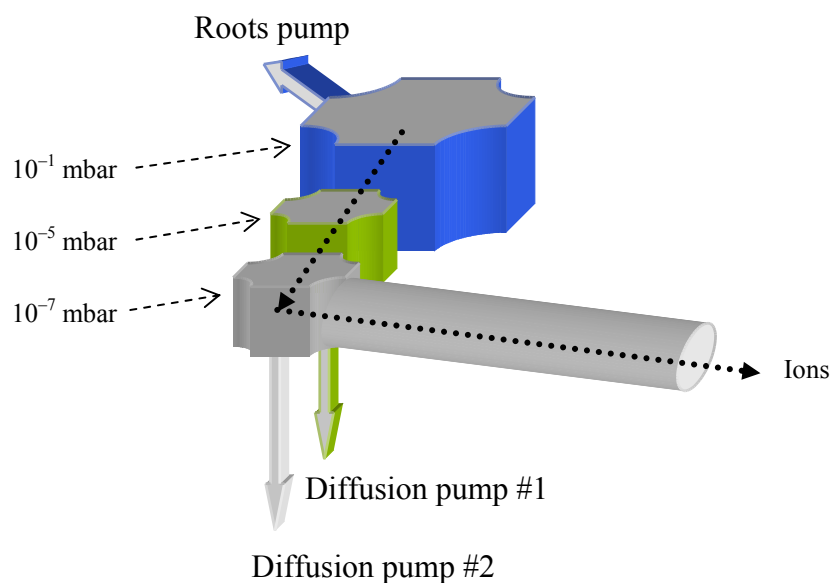
## 5.2 Design of the TOF mass spectrometer

Figure 5-3 shows the general arrangement of the experiment. In the first vacuum chamber the pulsed super sonic slit nozzle source (Figure 3-11) produces the species of interest which pass into the second chamber through a skimmer (Beam Dynamics, Ni,  $\text{\O} = 1.5 \text{ mm}$ ). The flow of carrier gas moves ions further through a pinhole ( $\text{\O} = 3 \text{ mm}$ ) into the detection chamber where the TOF mass spectrometer is situated. It was found that the flux of ions into the last chamber could be increased by applying a DC voltage in range of +40...60 V to the skimmer.



**Figure 5-3.** Schematic representation of TOF mass spectrometer incorporated with slit discharge ion source.

An exterior view of the vacuum hardware is shown in Figure 5-4. The production chamber is pumped by a Roots vacuum pump (Leybold, RA 3001, pumping speed 3900 m<sup>3</sup>/h) to keep pressure during the experiment at  $\approx 10^{-1}$  mbar. The intermediate and detection chambers are pumped by the diffusion vacuum pumps (Inficon, PDI 160-W, pumping speed 650 l/s) maintaining pressures of  $10^{-5}$  and  $10^{-7}$  mbar respectively. The differential pumping approach is used to provide the pressure not higher than  $5 \times 10^{-6}$  mbar in the last chamber, which is necessary for safe MCP detector operation.



**Figure 5-4.** Vacuum hardware of the mass spectrometer.

An ion optics simulation program SIMION 7.0 [40] was used to model the mass spectrometer. Figure 5-5 includes both the simulations of the dual-stage acceleration region and the calculated potential energy surfaces. Wiley and McLaren performed their calculations for the homogeneous electric field produced between the grids [39]. In this case, the potential decreases linear with the distance (Figure 5-5-a). In reality, the TOF electrodes are surrounded by a grounded metal tube, which distorts the potential energy surface (Figure 5-5-b). To avoid this, two metal rings were used. The cross section of the potential energy surface in Figure 5-5-c is more close to linear.

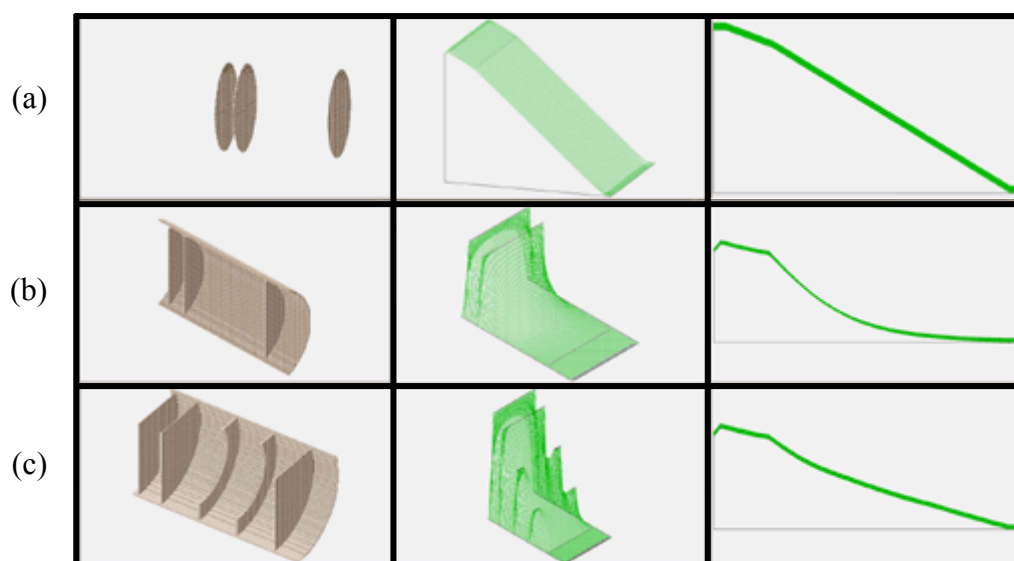


**Figure 5-5.** Simulation of the dual-stage acceleration region in the TOF mass spectrometer, potential energy surfaces and their cross sections. TOF grids are: in space (a), surrounded by a grounded tube (b), in a tube with two metal rings (c).

The scheme of the TOF spectrometer is shown in Figure 5-6. Three nickel grids (Goodfellow, LPI-3, open area 90%) form a dual-stage acceleration region. Two aluminium rings are used to stabilize the electric field. High voltage pulses (2-3 kV) are applied to the first grid and afterwards divided through the resistors as show in Figure 5-7. The value  $R$  (resistance between first and second grids) is adjustable in the range of 0...1 k $\Omega$ . It gives possibility to overlap the position of the space focus plane and position of the detector to increase mass resolution.

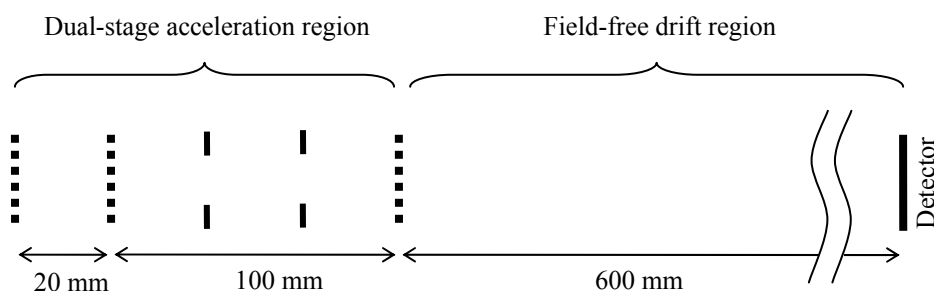


**Figure 5-6.** Dimension of the built TOF mass spectrometer.

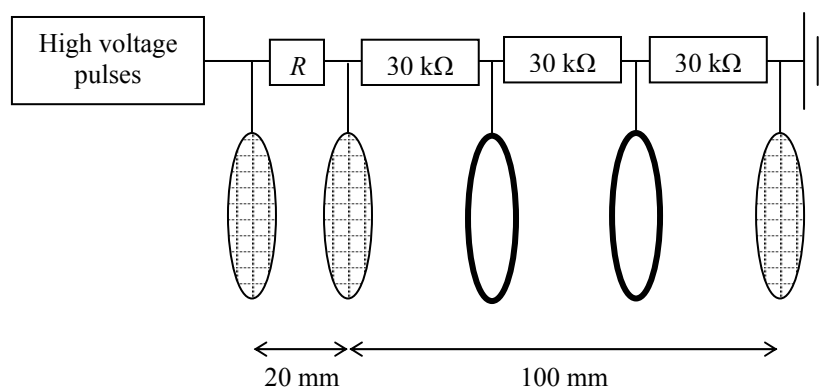


**Figure 5-7.** Acceleration region of the built TOF mass spectrometer.

The program SIMION allows simulating a flight of the ions. One can calculate a time-of-flight and a trajectory. Figure 5-8 presents an example of a separation two groups of ions with masses 30 and 31 amu. Position of the space focus plane is adjustable and depends on the voltage applied to the acceleration grids.

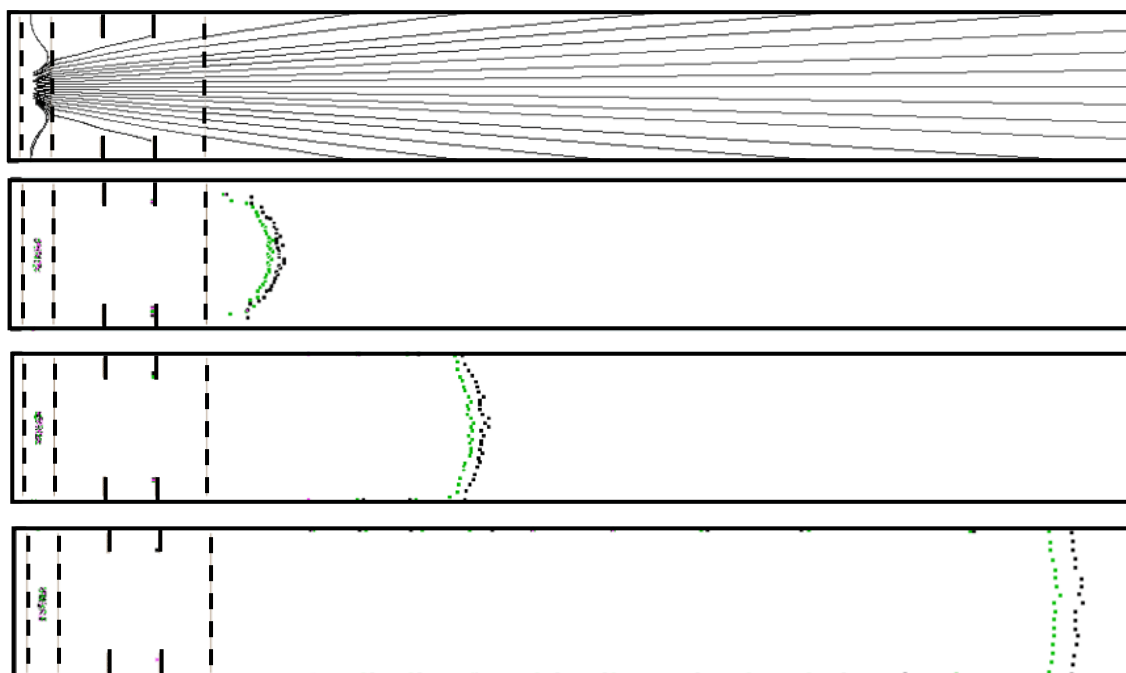


**Figure 5-8.** SIMION simulations of a mass separation in the TOF mass spectrometer.

Figure 5-9 shows the trigger system used in this work. The gas pulse is overlapped with the high voltage pulse applied to the jaws of the ion source. This provides a plasma discharge of about 250  $\mu\text{s}$  duration. The 20  $\mu\text{s}$  high voltage pulse applied to TOF electrodes accelerates the ions towards the detector. The time delay between these two high voltage pulses is necessary for ions to travel to the detection

## 5. TOF mass spectrometer

chamber. The value of the delay is adjustable in range of 200-300  $\mu\text{s}$  to optimize the signal intensity at the ion detector.

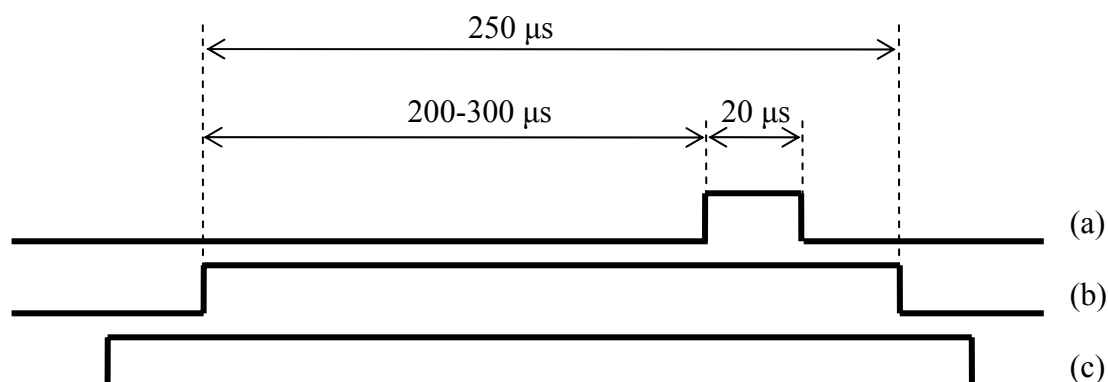


**Figure 5-9.** Time sequence used in the experiment. The high voltage pulses applied to the TOF grids (a), source jaws (b), gas valve (c).

The ion detector used in the experiment is a Micro Channel Plate (MCP) detector (Del Mar Ventures, MCP-MA 34). It has fast response time (in 100 ps range) and flat geometry (effective area diameter of 25 mm). The detector is arranged in a Chevron configuration (amplification  $10^6$ - $10^7$ ) and can be used for detection of both anions and cations depending on the electrical configuration and polarity of the voltage applied. The construction scheme of the MCP is shown in the Appendix. Figure 5-10 shows the electrical arrangement for cation detection.

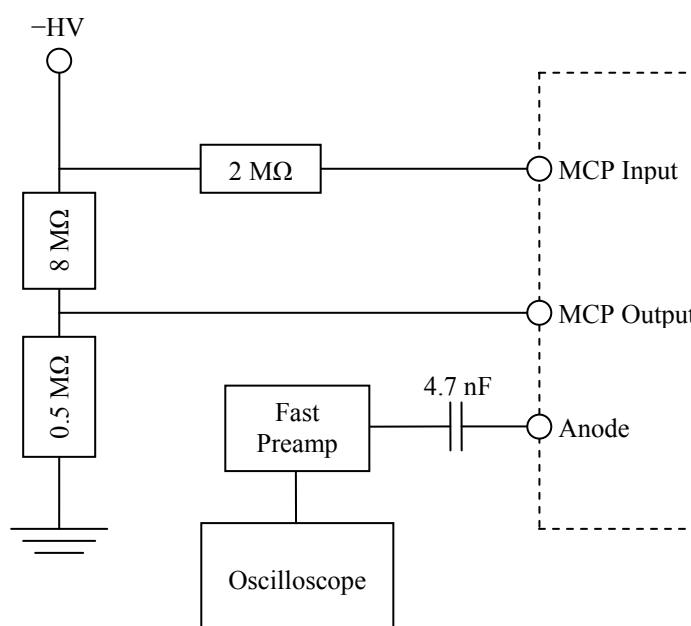


**Figure 5-10.** Electrical configuration of the MCP detector for the cations detection.



The power supply (SRS, PS350) provides a stable negative voltage ( $-1600\text{ V}$ ) at the MCP input. The signal from the anode is amplified through the fast preamplifier (Perkin Elmer, VT 120) and then recorder by a digital oscilloscope (LeCroy, 9350L). A TOF mass spectrum is obtained by accumulating 10 sweeps on the oscilloscope. Thereafter it is saved and analysed on the PC.

To observe the negatively charged species the TOF spectrometer has to be modified. The polarity of the acceleration field has to be reversed and electrical configuration of the MCP detector has to be changed (Figure 5-11). A high voltage applied to the detector should not exceed  $2\text{ kV}$  in order to provide safe MCP operation. To protect the oscilloscope one should switch it on after applying the high voltage, and switch it off before switching off the high voltage. A positive DC voltage (about  $50\text{ V}$ ) applied to the skimmer (Figure 5-3) increases the ions flux and therefore the signal intensity on the oscilloscope.

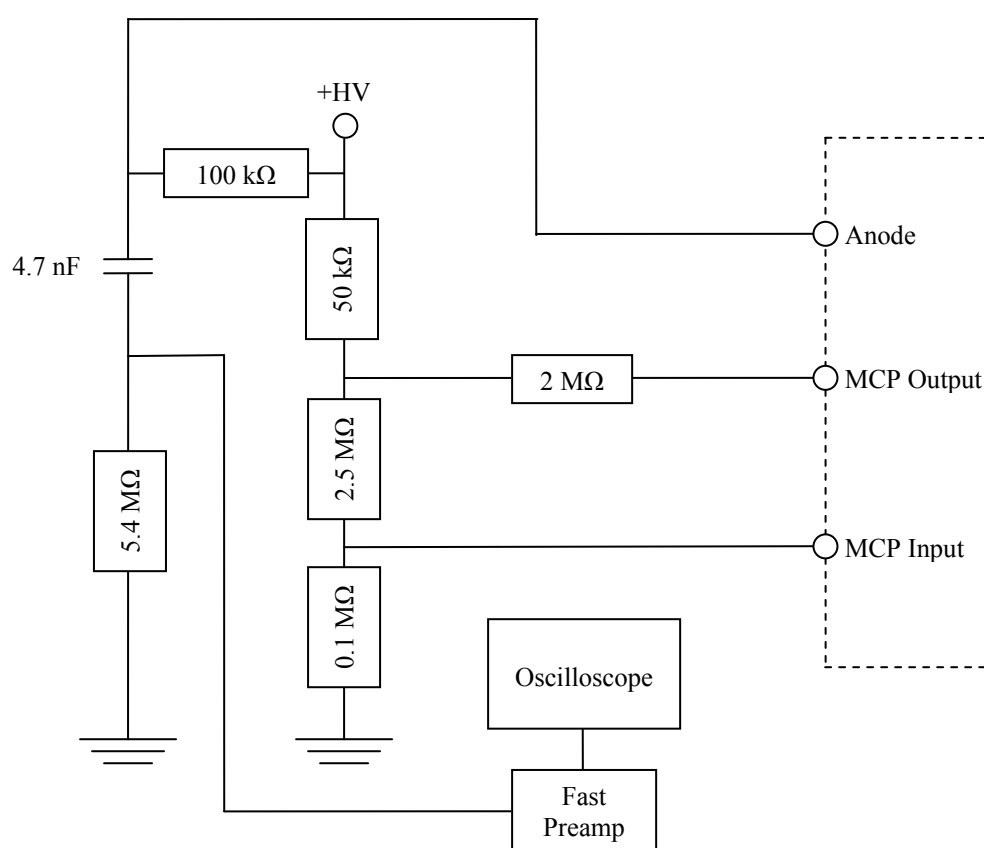


**Figure 5-11.** Electrical configuration of the MCP detector for the anions detection.

## 5.3 Mass spectrometric results

The recorded mass spectra of the cationic species are presented below. A few gas mixtures were prepared for calibration purpose. These were 10% nitrogen in helium, 0.2 % acetylene in helium, and 1% air/10% argon in helium. The time-of-flight mass spectra are shown in Figure 5-12. The first peak in all three spectra at 2.7  $\mu\text{s}$  was assigned to  $\text{He}^+$  (4 amu). The peaks at 6.1, 6.4, and 7.6  $\mu\text{s}$  were assigned to  $\text{C}_2\text{H}_2^+$  (26 amu),  $\text{N}_2^+$  (28 amu), and  $\text{Ar}^+$  (40 amu) respectively.

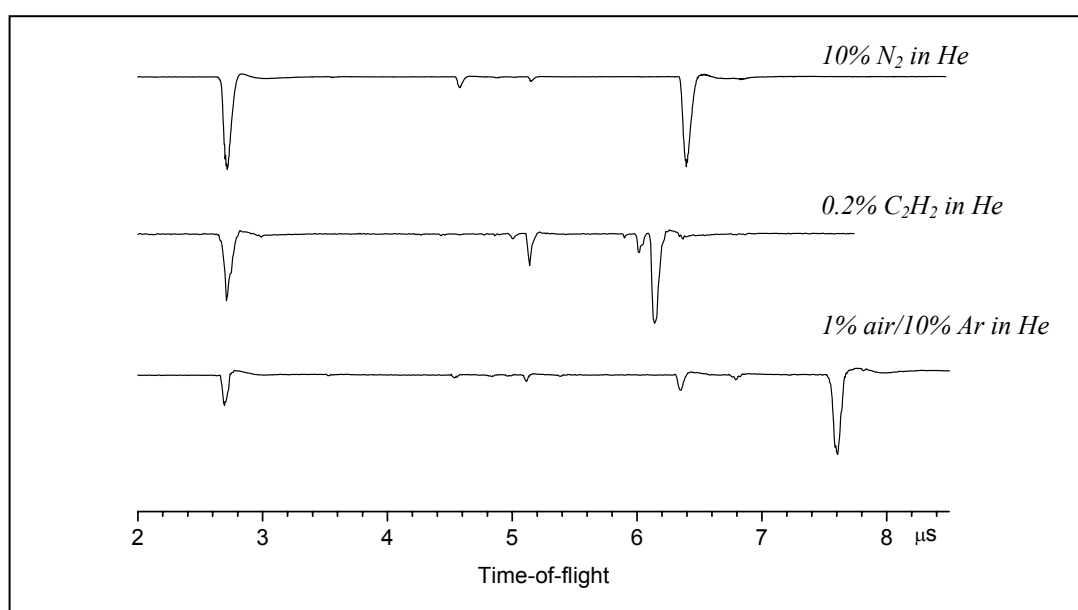


**Figure 5-12.** Calibration time-of-flight spectra.

The calibration constants for converting from flight time to mass were calculated as described in Section 5-1. The converted spectra are shown in Figure 5-13. The peaks at 4.6, 5.2, and 6.0  $\mu\text{s}$  can be straightforwardly assigned to  $\text{N}^+$  (14 amu),  $\text{H}_2\text{O}^+$  (18 amu), and  $\text{C}_2\text{H}^+$  (25 amu).

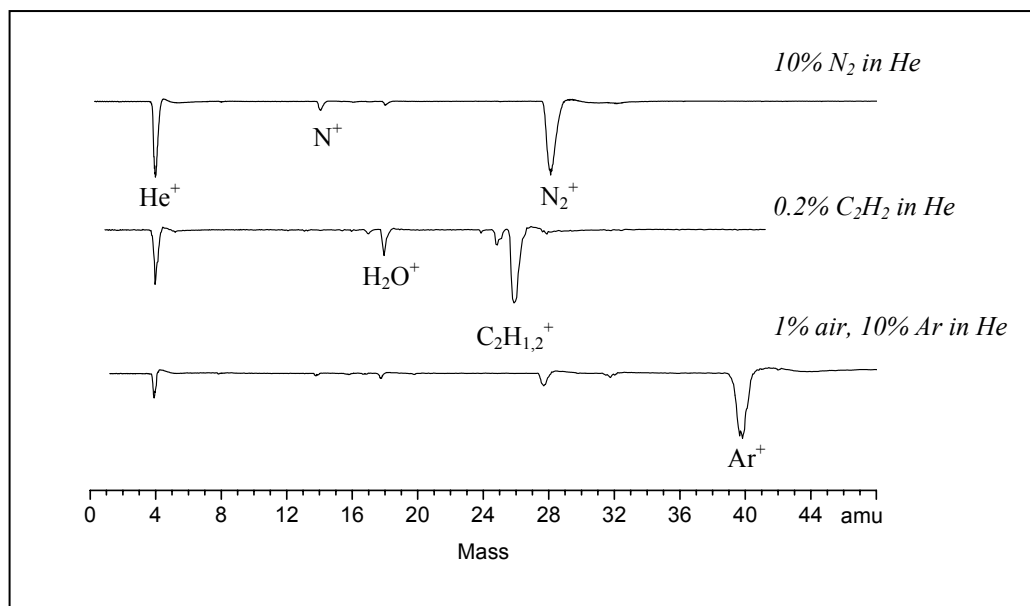


Figure 5-13. Converted calibration spectra.

To extend the calibration into the 40-50 amu region the mass spectrum of 0.3% cyanogen in helium was recorded (Figure 5-14, upper trace). The TOF spectra of 0.3% propene in helium and 0.25% propyne in helium demonstrate the mass resolution obtained. The series of four peaks correspond to the fragments of the precursor (Figure 5-14, middle and lower traces).

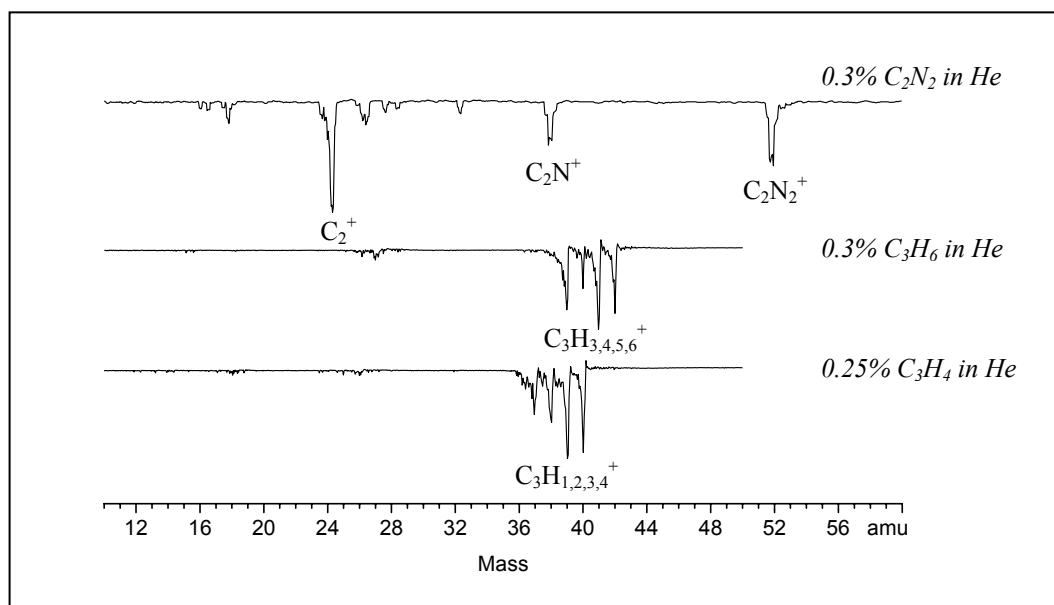
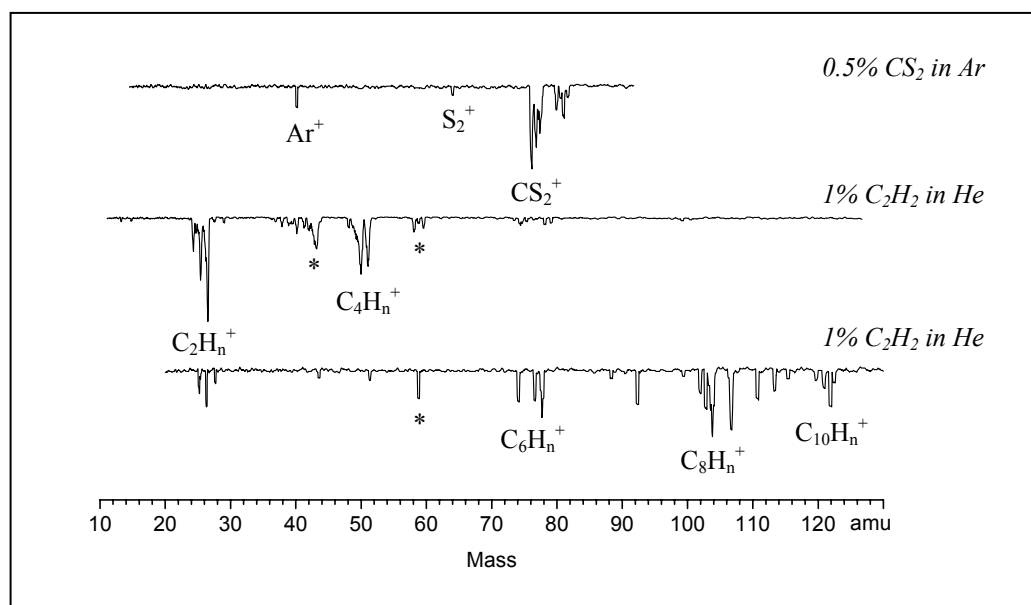


Figure 5-14. Obtained mass resolution.

## 5. TOF mass spectrometer

For expanding the calibration to higher mass region a mixture of 0.5% carbon disulfide (76 amu) in argon was chosen (Figure 5-15, upper trace).



**Figure 5-15.** Mass spectra of the acetylene/helium discharges. Traces of acetone derivatives (indicated by \*) are observed as this is routinely used in pressurized acetylene bottles.

The mass spectrum of acetylene plasma depends on several factors as was pointed out above. The following parameters were found to be optimal for production of polyacetylene carbon chains: gas mixture of 1% acetylene in helium; discharge voltage of  $-900$  V applied to the jaws of the ion source; pressure of  $5 \times 10^{-2}$  mbar in the first vacuum chamber. A mass spectrum obtained under this conditions and its assignment are shown in Figure 5-15.

The time delay between the discharge pulse and acceleration high voltage pulse (Figure 5-9) allows cutting the group of ions arriving towards the detector according to their masses. By varying this value one can optimize the spectrometer for detecting the preferred masses. For example, the lower trace in Figure 5-15 shows more of longer chain cations comparing to the other spectrum (middle trace). This is due to the  $100 \mu\text{s}$  longer delay used.

A mass spectrum of the anions in acetylene/helium discharge is shown in Figure 5-16. The two strong peaks at  $6.00$  and  $6.15 \mu\text{s}$  were assigned to  $\text{C}_2^-$  and  $\text{C}_2\text{H}^-$  respectively.

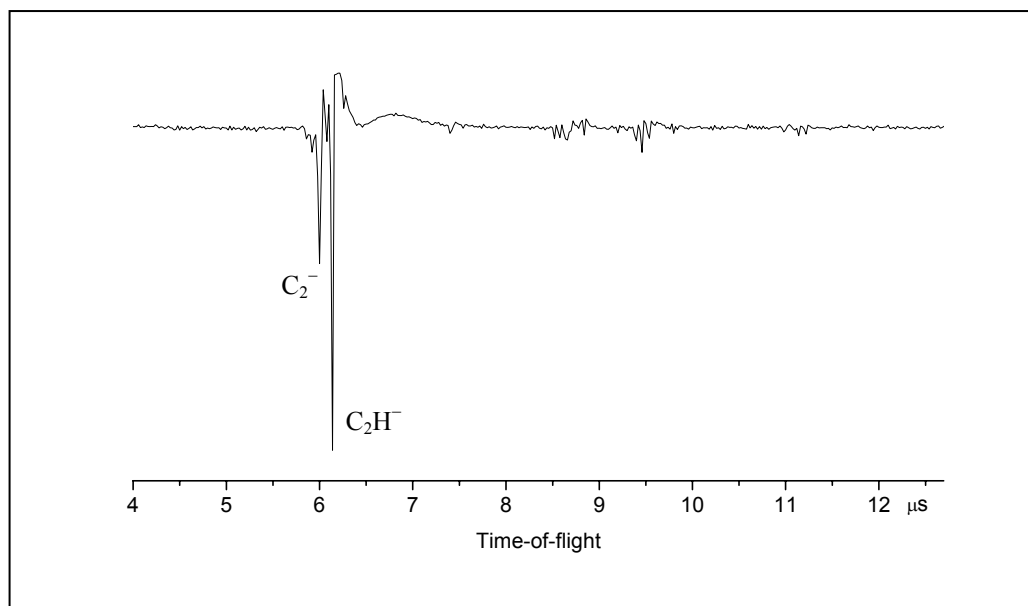
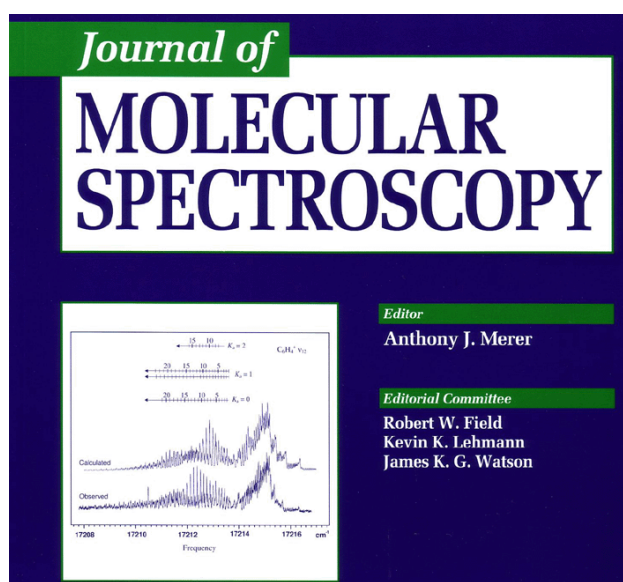


**Figure 5-16.** Mass spectra of the anions formed in the acetylene/helium discharge.



# 6

## Summary and outlook







The electronic absorption spectrum of the  ${}^2A'' - X {}^2A''$  origin band of the nonlinear carbon chain radical  $C_6H_4^+$  was rotationally resolved by cw-CRD spectroscopy [41]. It was analysed using a least-squares method and the rotational constants of the ground and excited states were determined accurately. The 581 nm band observed under the same discharge conditions is assigned to the same electronic transition of  $C_6H_4^+$  but involving the excitation of the  $\nu_{12}$  vibrational mode in the upper state based on comparison with *ab initio* results. The presented data provide a basis for future observations of the  $C_6H_4^+$  radical in both millimeter and infrared regions.

A linear time-of-flight mass spectrometer was constructed to provide on-line monitoring of the plasma discharge with a mass resolution of 1 amu at a range up to 120 amu. The results from the acetylene/helium plasma discharge are in good agreement with those obtained using the reflectron TOF mass spectrometer and a similar ion source [42]. To improve the experimental set-up, the following modifications can be made:

- Transferring the signal from the oscilloscope directly to a PC via a GPIB card will increase the speed of data processing;
- Computer control of the voltage applied will make the spectrometer easier to operate;
- Using a metal grid at ground potential in front of MCP detector will increase the flight time of ions improving the mass resolution;
- Installing a focusing lens will increase the number of ions arriving at the detector, and therefore increase the signal on the oscilloscope.



# 7

## References

- [10] M. Hippler, M. Quack, Cw cavity ring down spectroscopy in pulsed supersonic jets: nitrobenzene // *J. Chem. Phys.* 111 (1999) 273
- [11] P. Birza, T. Motylewski, D. I. Maier, Cw cavity ring down spectroscopy of nitrobenzene // *Chem. Phys.* 283 (2002) 119
- [12] P. Birza, D. Khoroshev, A. Ch. Maier, Doppler broadening in the gas phase  $B^2\Sigma^+$  // *Phys. Lett.* 382 (2003) 245
- [13] A. Kantrowitz, J. Grey, High resolution laser spectroscopy: Theoretical // *Rev. Sci. Instrum.* 44 (1973) 1511



- 
- [1] J.P. Maier, Electronic spectroscopy of carbon chains // Chem. Soc. Rev. 1 (1997) 21
- [2] A. Van Orden, R.J. Saykally, Small carbon clusters: spectroscopy, structure, and energetics // Chem. Rev. 98 (1998) 2313
- [3] M.C. McCarthy, P. Thaddeus, Microwave and laser spectroscopy of carbon chains and rings // Chem. Soc. Rev. 30 (2001) 177
- [4] Q.L. Chang, S.C. O'Brien, J.R. Heath, Y. Liu, R.F. Curl, H.W. Kroto, R.E. Smalley, Reactivity of large carbon clusters: spheroidal carbon shells and their possible relevance to the formation and morphology of soot // J. Phys. Chem. 90 (1986) 525
- [5] Ph. Gerhardt, S. Löffler, K.H. Homann, Polyhedral carbon ions in hydrocarbon flames // Chem. Phys. Lett. 137 (1987) 306
- [6] H.W. Kroto, K. McKay, The formation of quasi-icosahedral spiral shell carbon particles // Nature 331 (1988) 328
- [7] P.B. Sunderland, G.M. Faeth, Soot formation in hydrocarbon/air laminar jet diffusion flames // Combust. Flame 105 (1996) 132
- [8] K.C. Lin, Z. Dali, G.M. Faeth, Laminar soot processes // in Fifth International Microgravity Combustion Workshop, NASA Glenn Research Center, Cleveland, Ohio, 1999
- [9] H.W. Kroto, J.R. Heath, S.C. O'Brien, R.F. Curl, R.E. Smalley, C<sub>60</sub>: Buckminsterfullerene // Nature 318 (1985) 162
- [10] W.E. Sinclair, D. Pfluger, H. Linnartz, J.P. Maier, Rotationally resolved  $A^2\Pi_g \leftarrow X^2\Pi_u$  electronic spectrum of triacetylene cation by frequency modulation absorption spectroscopy // J. Chem. Phys. 110 (1999) 296
- [11] D. Pfluger, T. Motylewski, H. Linnartz, W.E. Sinclair, J.P. Maier, Rotationally resolved  $A^2\Pi_u \leftarrow X^2\Pi_g$  electronic spectrum of tetraacetylene cation // Chem. Phys. Lett. 329 (2000) 29
- [12] P. Cias, O. Vaizert, A. Denisov, J. Mes, H. Linnartz, J.P. Maier, Electronic gas-phase spectrum of the pentaacetylene cation // J. Phys. Chem. A 106 (2002) 9890
- [13] H. Linnartz, T. Motylewski, J.P. Maier, The  $^2\Pi \leftarrow X^2\Pi$  electronic spectra of C<sub>8</sub>H and C<sub>10</sub>H in the gas phase // J. Chem. Phys. 109 (1998) 3819
- [14] M. Araki, H. Linnartz, P. Cias, A. Denisov, J. Fulara, A. Batalov, I. Shnitko, J.P. Maier, High resolution electronic spectroscopy of a nonlinear carbon chain radical C<sub>6</sub>H<sub>4</sub><sup>+</sup> // J. Chem. Phys. 118 (2003) 10561

## 7. References

---

- [15] M. Araki, P. Cias, A. Denisov, J. Fulara and J.P. Maier, Electronic spectroscopy of the nonlinear carbon chains  $C_4H_4^+$  and  $C_8H_4^+$  // *Can. J. Chem.* 82 (2004) 1
- [16] M. Ohishi, W.M. Irvine, N. Kaifu, Molecular abundance variations among and within cold, dark molecular clouds // in *Astrochemistry of Cosmic Phenomena*, Ed. P.D. Singh, Dordrecht, Kluwer (1992) 1
- [17] C.H. Townes, A.L. Schawlow, Asymmetric-top molecules // in *Microwave Spectroscopy*, New-York: Dover Publications (1975) 83
- [18] P.C. Cross, R.M. Hainer, G.W. King, The asymmetric rotor. II. Calculation of dipole intensities and line classification // *J. Chem. Phys.* 12 (1944) 210
- [19] A. O'Keefe, D.A.G. Deacon, Cavity ring-down optical spectrometer for absorption measurements using pulsed laser sources // *Rev. Sci. Instrum.* 59 (1988) 2544
- [20] J.J. Scherer, J.B. Paul, A. O'Keefe, R.J. Saykally, Cavity ringdown laser absorption spectroscopy: history, development, and application to pulsed molecular beams // *Chem. Rev.* 97 (1997) 25
- [21] M.D. Wheeler, S.M. Newman, A.J. Orr-Ewing, M.N.R. Ashfold, Cavity ring-down spectroscopy // *J. Chem. Soc., Faraday Trans.* 94 (1998) 337
- [22] D.Z. Anderson, J.C. Frisch, C.S. Masser, Mirror reflectometer based on optical cavity decay time // *Appl. Opt.* 23 (1984) 1238
- [23] D. Romanini, A.A. Kachanov, N. Sadeghi, E. Stoeckel, CW cavity ring down spectroscopy // *Chem. Phys. Lett.* 264 (1997) 316
- [24] Y. He, M. Hippler, M. Quack, High-resolution cavity ring-down absorption spectroscopy of nitrous oxide and chloroform using a near-infrared cw diode laser // *Chem. Phys. Lett.* 289 (1998) 527
- [25] M. Hippler, M. Quack, Cw cavity ring-down infrared absorption spectroscopy in pulsed supersonic jets: nitrous oxide and methane // *Chem. Phys. Lett.* 314 (1999) 273
- [26] P. Birza, T. Motylewski, D. Khoroshev, A. Chirokolava, H. Linnartz, J.P. Maier, Cw cavity ring down spectroscopy in a pulsed planar plasma expansion // *Chem. Phys.* 283 (2002) 119
- [27] P. Birza, D. Khoroshev, A. Chirokolava, T. Motylewski, J.P. Maier, Lifetime broadening in the gas phase  $B^2\Pi \leftarrow X^2\Pi$  electronic spectrum of  $C_8H$  // *Chem. Phys. Lett.* 382 (2003) 245
- [28] A. Kantrowitz, J. Grey, High intensity source for the molecular beam. I. Theoretical // *Rev. Sci. Instrum.* 22 (1951) 328
- [29] D.N. Travis, J.C. McGurk, D. McKeown, R.G. Denning, Infrared spectroscopy of supercooled gases // *Chem. Phys. Lett.* 45 (1977) 287

- [30] Y. Mizugai, H. Kuze, H. Jones, M. Takami, Diode-laser spectroscopy of supersonic free jets // *Appl. Phys. B* 32 (1983) 43
- [31] G.D. Hayman, J. Hodge, B.J. Howard, J.S. Muentert, T.R. Dyke, Molecular-beam infrared absorption studies of rare gas-carbonyl sulfide complexes // *Chem. Phys. Lett.* 118 (1985) 12
- [32] C.M. Lovejoy, D.J. Nesbitt, High sensitivity, high-resolution IR laser spectroscopy in slit supersonic jets: application to molecular nitrogen-hydrogen fluoride complex ( $\text{N}_2\text{HF}$ )  $\nu_1$  and  $\nu_5 + \nu_1 - \nu_5$  // *J. Chem. Phys.* 86 (1987) 3151
- [33] S. Davis, D.T. Anderson, G. Duxbury, D.J. Nesbitt, Jet-cooled molecular radicals in slit supersonic discharges: Sub-Doppler infrared studies of methyl radical // *J. Chem. Phys.* 107 (1997) 5661
- [34] T. Motylewski, H. Linnartz, Cavity ring down spectroscopy on radicals in a supersonic slit nozzle discharge // *Rev. Sci. Instrum.* 70 (1999) 1305
- [35] D. Luckhaus, M. Quack, The far infrared pure rotational spectrum and the Coriolis coupling between  $\nu_3$  and  $\nu_8$  in  $\text{CH}^{35}\text{ClF}_2$  // *Mol. Phys.* 63 (1989) 745
- [36] D.L. Joo, D.J. Clouthier, A.J. Merer, Determination of the spectroscopic constants of a dark vibrational state: Fermi and Coriolis perturbations in the  $\nu_2$  band of formyl chloride // *J. Chem. Phys.* 101 (1994) 31
- [37] M.J. Frisch et al., Gaussian 03 // Revision A.1, Inc., Pittsburgh, PA, 2003
- [38] MOLPRO, a package of ab initio programs designed by H.-J. Werner and P.J. Knowles, version 2002.1, with contributions from others. Available from [www.molpro.net](http://www.molpro.net)
- [39] W.C. Wiley, I.H. McLaren, Time-of-flight mass spectrometer with improved resolution // *Rev. Sci. Instrum.* 26 (1955) 1150
- [40] D.A. Dahl, SIMION 7.0 // [www.simion.com](http://www.simion.com)
- [41] D. Khoroshev, M. Araki, P. Kolek, P. Birza, A. Chirokolava, J.P. Maier, Rotationally resolved electronic spectroscopy of a nonlinear carbon chain radical  $\text{C}_6\text{H}_4^+$  // *J. Mol. Spec.* 227 (2004) 81
- [42] E. Witkowicz, H. Linnartz, C.A. de Lange, W. Ubachs, A. Sfounis, M. Massauti, M. Velegrakis, Mass spectrometric and laser spectroscopic characterization of a supersonic planar plasma expansion // *Int. J. Mass Spec.* 232 (2004) 25





# 8

## Appendix

11 - 3 <sub>12</sub>	17213.5145	17213.5137	0.0
02 - 3 <sub>03</sub>	17213.4377	17213.4381	-0.0
13 - 4 <sub>14</sub>	17213.4146	17213.4173	-0.0
12 - 4 <sub>13</sub>		17213.4124	0.0
03 - 4 <sub>04</sub>	17213.3325	17213.3373	-0.0
14 - 5 <sub>15</sub>	17213.3143	17213.3142	0.0
13 - 5 <sub>14</sub>		17213.3081	0.0
04 - 5 <sub>05</sub>	17213.2231	17213.2337	-0.0
15 - 6 <sub>16</sub>	17213.2065	17213.2082	-0.0
14 - 6 <sub>15</sub>		17213.2009	0.0
26 - 8 <sub>27</sub>	17213.1985	17213.2150	-0.0
25 - 8 <sub>26</sub>		17213.2149	-0.0
05 - 6 <sub>06</sub>	17213.1221	17213.1271	-0.0
16 - 7 <sub>17</sub>	17213.1054	17213.0993	0.0
15 - 7 <sub>16</sub>		17213.0907	0.0
06 - 7 <sub>07</sub>	17213.0125	17213.0176	-0.0
17 - 8 <sub>18</sub>	17212.9911	17212.9875	0.0



## 8.1 Asymmetric rotors

Unlike the cases of linear and symmetric rotor molecules, there are no closed formulae for the rotational term values which are generally applicable to asymmetric rotors. Two types of term value expressions are in use. The first one involves the asymmetry parameter  $b$ . For a molecule which resembles a prolate rather than an oblate symmetric rotor, a so-called prolate near-symmetric rotor for which

$$I_c \approx I_b > I_a \quad (8-1)$$

the term values can be written as

$$F(J_\tau) = \frac{1}{2}(B + C)J(J + 1) + [A - \frac{1}{2}(B + C)]W(b_p) \quad (8-2)$$

neglecting centrifugal distortion. The function  $W(b_p)$  has the form

$$W(b_p) = K_a^2 + c_1 b_p + c_2 b_p^2 + \dots \quad (8-3)$$

where  $K_a$ , sometimes written as  $K_{-1}$ , is the quantum number  $K$  of the corresponding prolate symmetric rotor. For an oblate near-symmetric rotor the symbol used is  $K_c$  or  $K_1$ . The quantity  $b_p$  is the asymmetry parameter used for a prolate near-symmetric rotor and is given by

$$b_p = (C - B)/(2A - B - C) \quad (8-4)$$

The coefficients  $c_1, c_2, \dots$  are functions of the quantum numbers and have been listed in Reference [17];  $\tau$  is a label used to distinguish the  $(2J + 1)$  rotational levels having the same value of  $J$  and can take the values

$$\tau = J, J - 1, J - 2, \dots, -J \quad (8-5)$$

analogous to the signed quantum number  $k$  in a symmetric rotor. When  $B = C$ ,  $b_p = 0$  and the term value become those of a prolate symmetric rotor.

The second type of term value expression is for a general asymmetric rotor and is of the form

$$F(J_\tau) = \frac{1}{2}(A + C)J(J + 1) + \frac{1}{2}(A - C)E(k) \quad (8-6)$$

where  $E(k)$  is a function of the asymmetry parameter  $k$ , introduced by Ray, and given by

$$k = (2B - A - C)/(A - C) \quad (8-7)$$

For a prolate symmetric rotor  $B = C$  and  $k = -1$  and for an oblate symmetric rotor  $A = B$  and  $k = 1$ ; these extreme values of  $k$  are used as subscripts in the  $K_{-1}$  and  $K_1$  symbols sometimes used for prolate and oblate symmetric rotors, respectively. Instead of using

## 8. Appendix

the subscript  $\tau$  as a label for states having the same value of  $J$ , the values of  $K_a$  and  $K_c$  are often used, as in  $J_{K_a K_c}$ . The quantity  $\tau$  is related to  $K_a$  and  $K_c$  by

$$\tau = K_a - K_c \text{ (or } K_{-1} - K_1) \quad (8-8)$$

Figure 8-1 shows how the energy levels of a prolate symmetric rotor correlate with those of an oblate symmetric rotor for the case when  $A = 2C$  and  $B$  varies between  $A$  and  $C$ . This shows how, as a prolate symmetric rotor becomes slightly asymmetric, on the left-hand side of the figure, the double degeneracy of all levels with  $K_a > 0$  is removed. The splitting decreases with  $K_a$ , for constant  $J$ , and increases with  $J$  for constant  $K_a$ .

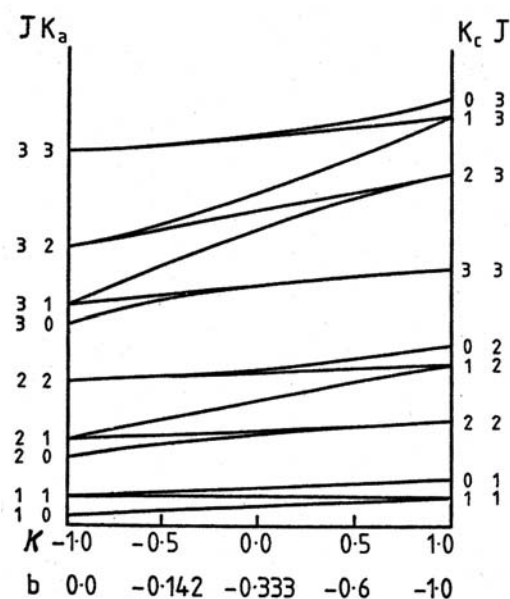


**Figure 8-1.** Correlation of the rotational energy levels of a prolate ( $k = -1.0$ ,  $b = 0$ ) with those of an oblate ( $k = 1.0$ ,  $b = -1.0$ ) symmetric rotor [17].

The selection rule governing the changes in  $J$  in asymmetric rotors is

$$\Delta J = 0, \pm 1 \quad (8-9)$$

Transitions with  $\Delta J = 0$  are called *Q*-branch transitions and those with  $\Delta J = +1$  and  $-1$  are *R*- and *P*-branch transitions, respectively. The selection rules replacing the  $\Delta K = 0$  rule in symmetric rotors are more complex. They involve the parity, i.e. the evenness or oddness, of  $K_a$  and  $K_c$  and also the direction in the molecule of the permanent dipole moment. For example, if the dipole moment is along the *a*-axis, the parity of either  $K_a$  or  $K_c$  must change during the transition. If we label the rotational energy levels as *eo*, implying that  $K_a$  is even and  $K_c$  is odd, *oe*, *ee* or *oo* the selection rules are those given in Table 8-1 for an *a*-axis dipole moment; the allowed transitions in this case are referred to as *A*-type. This table also gives the selection rules for *B*- and *C*-

type transitions which occur when the dipole moment is along the  $b$ - or the  $c$ -axis, respectively.

**Table 8-1.** Selection rules for asymmetric rotors. In all cases  $\Delta J = 0, \pm 1$ .

<b>Axes parallel to dipole moment</b>	<b>Allowed transitions</b>
$a$ (least)	$ee \leftrightarrow eo$ $oo \leftrightarrow oe$
$b$ (intermediate)	$ee \leftrightarrow oo$ $eo \leftrightarrow oe$
$c$ (greatest)	$ee \leftrightarrow oe$ $oo \leftrightarrow eo$

Since the selection rules in Table 8-1 refer only to the parity of  $K_a$  and  $K_c$ , in principle  $\Delta K_a$  or  $\Delta K_c$  can be  $0, \pm 2, \pm 4, \dots$  or  $\pm 1, \pm 3, \pm 5, \dots$ . In practice, if the molecule is a prolate near-symmetric rotor, only transitions with  $\Delta K_a = 0$  or  $\pm 1$ , the symmetric rotor selection rules, have significant intensity and, for an oblate near-symmetric rotor, only transitions with  $\Delta K_c = 0$  or  $\pm 1$ . The same rotational selection rules apply to electronic, vibronic and rotational electric dipole transitions. The main difference is that there is a much larger change of rotational constants due to an electronic than a vibronic transition.

In a band contour of a symmetric or near-symmetric rotor three kinds of regular series of features may stand out. These are:

1. Line-like  $Q$  branches in which many  $Q$ -branch lines are nearly coincident. This occurs when  $\frac{1}{2}(B' + C') \approx \frac{1}{2}(B'' + C'')$ , where  $B''$ ,  $C''$  and  $B'$ ,  $C'$  are molecular rotational constants in ground and electronically excited state.
2.  $R$ -branch heads to be observed when  $\frac{1}{2}(B' + C') < \frac{1}{2}(B'' + C'')$ .
3.  $P$ -branch heads formation takes place when  $\frac{1}{2}(B' + C') > \frac{1}{2}(B'' + C'')$ .

## 8.2 Laser system and optical components

The model COHERENT 899-AUTOSCAN system is a convertible cw laser that can operate as a conventional dye ring laser or as a solid state ring laser using Titanium:Sapphire as the gain medium. It is tuneable from 560 to 700 nm in dye operation. The compact solid-state diode-pumped, frequency-doubled Nd:Vanadate (Nd:YVO<sub>4</sub>) laser COHERENT Verdi V-10 provides a single-frequency green (532 nm) output beam and is used as the pump source. The 899-AUTOSCAN incorporates passive and active frequency control in order to obtain stable operation in a single longitudinal cavity mode. An optical diagram of dye configuration is shown in Figure 8-2.

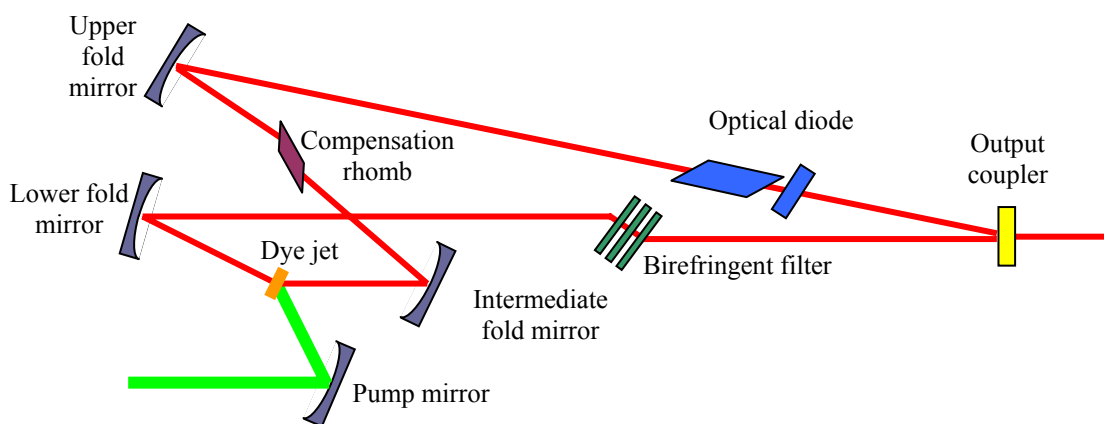


**Figure 8-2.** Optical scheme of COHERENT 899-AUTOSCAN ring laser system in dye configuration.

The major laser head components and stages are mounted to an Invar bar that provides mechanical strength and length stability due to a low coefficient of expansion. This results in passive cavity length thermal stabilization of less than 1 micron per degree centigrade. Unidirectional lasing is achieved with an optical diode. The device achieves lasing in one preferred direction by utilizing optical activity and the Faraday effect. Figure 8-3 includes a Faraday rotator, an optical activity element and intracavity Brewster plates. The Faraday rotator changes the polarization in one certain rotational direction independent of beam direction, while the optical rotator distinguishes the forward and backward waves and affects the rotation direction. Therefore the forward wave has a certain polarization, which is changed by the optical

rotator and is recovered after the Faraday rotator. The backward wave's polarization is changed in the same direction in both rotators and Brewster plates reflect this light out of the cavity.

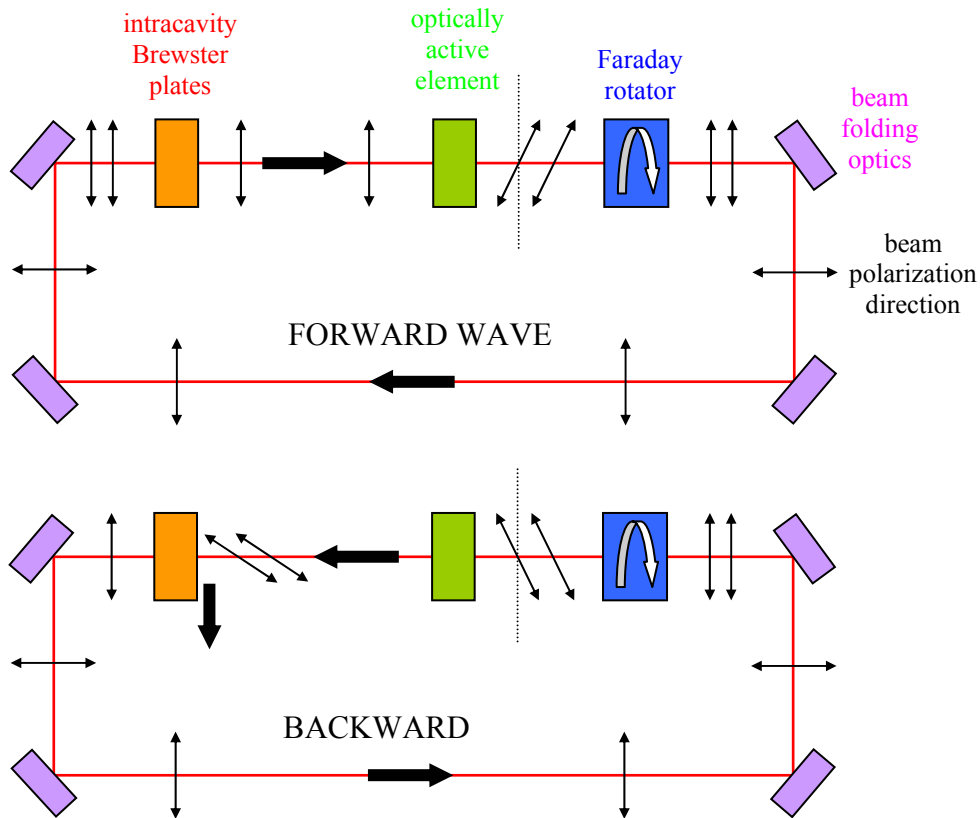


**Figure 8-3.** Optical diode scheme.

Passive frequency control is achieved with a series of intracavity frequency filters. The three plate birefringent filter allows broadband operation over approximately 2 GHz. This filter is mounted at Brewster's angle to ensure maximum tuning range. With the insertion of the intracavity etalon assembly, which consist of a thick and thin etalon, the operational bandwidth is narrowed to 10 MHz. The etalons are of low finesse to allow broadband coverage. Active frequency control is achieved with an electronic servo loop and a reference cavity. The servo loop uses an error signal derived from the reference cavity when the laser frequency drifts. Part of the error signal is applied to the tweeter, a mirror mounted on a piezo device, to correct for fast cavity length variation. The other part is used to drive the rotating Brewster plate to compensate for the slower cavity length changes. With active frequency control, line width may be narrowed down to 500 kHz. Single mode frequency scanning up to 30 GHz is possible by continuously varying the cavity length with the

## 8. Appendix

---

rotating galvanometer driven Brewster plate. The Brewster plate is mounted at the vertex of the optical beam path. This design minimizes displacement of the intracavity beam while maintaining a constant reflection loss of about 0.4 % during a scan. The thickness of the thick etalon may be varied with the piezoelectric transducer in order to track the laser frequency as it is scanned. The thin etalon is tuned by a galvanometer drive which controls the tip angle.



## 8.3 Observed line positions

**Table 8-2.** The observed and fitted rovibronic lines for the origin band in the  ${}^2A''-X\ {}^2A''$  electronic transition of  $C_6H_4^+$ .

$N_{KaKc}$	$\nu_{\text{obs}} (\text{cm}^{-1})$	$\nu_{\text{calc}} (\text{cm}^{-1})$	$o - c$
$3_{03} - 2_{02}$		16545.2258	0.0000
$2_{11} - 1_{10}$	16545.2258	16545.2242	0.0016
$2_{12} - 1_{11}$		16545.2219	0.0039
$4_{04} - 3_{03}$		16545.3053	-0.0017
$3_{13} - 2_{12}$	16545.3036	16545.3039	-0.0003
$3_{12} - 2_{11}$		16545.3073	-0.0037
$4_{14} - 3_{13}$		16545.3828	0.0014
$4_{13} - 3_{12}$	16545.3842	16545.3874	-0.0032
$5_{05} - 4_{04}$		16545.3817	0.0025
$6_{06} - 5_{05}$		16545.4550	0.0024
$5_{15} - 4_{14}$	16545.4574	16545.4587	-0.0013
$5_{14} - 4_{13}$		16545.4643	-0.0069
$7_{07} - 6_{06}$		16545.5252	0.0043
$6_{16} - 5_{15}$	16545.5295	16545.5314	-0.0019
$6_{15} - 5_{14}$		16545.5382	-0.0087
$8_{08} - 7_{07}$		16545.5924	0.0104
$7_{17} - 6_{16}$	16545.6028	16545.6011	0.0017
$7_{16} - 6_{15}$		16545.6090	-0.0062
$9_{09} - 8_{08}$	16545.6582	16545.6564	0.0018
$8_{18} - 7_{17}$		16545.6677	0.0034
$8_{17} - 7_{16}$	16545.6711	16545.6767	-0.0056
$10_{010} - 9_{09}$	16545.7138	16545.7174	-0.0036
$9_{19} - 8_{18}$		16545.7312	0.0007
$9_{18} - 8_{17}$	16545.7319	16545.7414	-0.0095
$11_{011} - 10_{010}$		16545.7753	0.0008
$6_{25} - 5_{24}$	16545.7761	16545.7743	0.0018
$10_{110} - 9_{19}$		16545.7916	0.0004 <sup>a</sup>
$10_{19} - 9_{18}$	16545.7920	16545.8029	-0.0109 <sup>a</sup>
$12_{012} - 11_{011}$	16545.8344	16545.8300	0.0044
$11_{111} - 10_{110}$	16545.8547	16545.8489	0.0058 <sup>a</sup>

## 8. Appendix

**Table 8-2.** (continued)

11 <sub>110</sub>	–	10 <sub>19</sub>		16545.8614	–0.0067 <sup>a</sup>
7 <sub>25</sub>	–	6 <sub>24</sub>	16545.8547	16545.8446	0.0101
13 <sub>013</sub>	–	12 <sub>012</sub>	16545.8836	16545.8817	0.0019
12 <sub>112</sub>	–	11 <sub>111</sub>		16545.9032	0.0088 <sup>a</sup>
12 <sub>111</sub>	–	11 <sub>110</sub>	16545.9120	16545.9168	–0.0048 <sup>a</sup>
8 <sub>27</sub>	–	7 <sub>26</sub>		16545.9117	0.0003
14 <sub>014</sub>	–	13 <sub>013</sub>	16545.9277	16545.9303	–0.0026
13 <sub>113</sub>	–	12 <sub>112</sub>		16545.9544	0.0166 <sup>a</sup>
13 <sub>112</sub>	–	12 <sub>111</sub>	16545.9710	16545.9691	0.0019 <sup>a</sup>
15 <sub>015</sub>	–	14 <sub>014</sub>		16545.9759	–0.0049
9 <sub>27</sub>	–	8 <sub>26</sub>		16545.9758	–0.0048
14 <sub>114</sub>	–	13 <sub>113</sub>		16546.0024	0.0123 <sup>a</sup>
14 <sub>113</sub>	–	13 <sub>112</sub>	16546.0147	16546.0183	–0.0036 <sup>a</sup>
16 <sub>016</sub>	–	15 <sub>015</sub>		16546.0183	–0.0036
17 <sub>017</sub>	–	16 <sub>016</sub>		16546.0576	–0.0012
15 <sub>115</sub>	–	14 <sub>114</sub>	16546.0564	16546.0474	0.0090 <sup>a</sup>
15 <sub>114</sub>	–	14 <sub>113</sub>		16546.0644	–0.0080 <sup>a</sup>
16 <sub>116</sub>	–	15 <sub>115</sub>		16546.0893	0.0073 <sup>a</sup>
16 <sub>115</sub>	–	15 <sub>114</sub>	16546.0966	16546.1074	–0.0108 <sup>a</sup>
18 <sub>018</sub>	–	17 <sub>017</sub>		16546.0939	0.0027
11 <sub>210</sub>	–	10 <sub>29</sub>		16546.0946	0.0020
28 <sub>028</sub>	–	27 <sub>027</sub>		16546.2865	0.0135
31 <sub>031</sub>	–	30 <sub>030</sub>	16546.3000	16546.2840	0.0160
29 <sub>029</sub>	–	28 <sub>028</sub>		16546.2887	0.0113
30 <sub>030</sub>	–	29 <sub>029</sub>		16546.2879	0.0121
28 <sub>128</sub>	–	27 <sub>127</sub>		16546.3516	–0.0102
31 <sub>131</sub>	–	30 <sub>130</sub>	16546.3414	16546.3478	–0.0064
29 <sub>129</sub>	–	28 <sub>128</sub>		16546.3534	–0.0120
30 <sub>130</sub>	–	29 <sub>129</sub>		16546.3521	–0.0107
32 <sub>131</sub>	–	31 <sub>130</sub>		16546.3765	0.0035
28 <sub>127</sub>	–	27 <sub>126</sub>		16546.3833	–0.0033
31 <sub>130</sub>	–	30 <sub>129</sub>	16546.3800	16546.3828	–0.0028
29 <sub>128</sub>	–	28 <sub>127</sub>		16546.3862	–0.0062
30 <sub>129</sub>	–	29 <sub>128</sub>		16546.3860	–0.0060
19 <sub>218</sub>	–	18 <sub>217</sub>	16546.4475	16546.4468	0.0007

Table 8-2. (continued)

19 <sub>2 17</sub>	–	18 <sub>2 16</sub>		16546.4474	0.0001
20 <sub>2 19</sub>	–	19 <sub>2 18</sub>	16546.4820	16546.4769	0.0051
20 <sub>2 18</sub>	–	19 <sub>2 17</sub>		16546.4776	0.0044
21 <sub>2 20</sub>	–	20 <sub>2 19</sub>	16546.5067	16546.5040	0.0027
21 <sub>2 19</sub>	–	20 <sub>2 18</sub>		16546.5048	0.0019
28 <sub>2 27</sub>	–	27 <sub>2 26</sub>		16546.6070	0.0002
28 <sub>2 26</sub>	–	27 <sub>2 25</sub>		16546.6086	–0.0014
31 <sub>2 30</sub>	–	30 <sub>2 29</sub>		16546.6049	0.0023
31 <sub>2 29</sub>	–	30 <sub>2 28</sub>	16546.6072	16546.6068	0.0004
29 <sub>2 28</sub>	–	28 <sub>2 27</sub>		16546.6094	–0.0022
29 <sub>2 27</sub>	–	28 <sub>2 26</sub>		16546.6111	–0.0039
30 <sub>2 29</sub>	–	29 <sub>2 28</sub>		16546.6087	–0.0015
30 <sub>2 28</sub>	–	29 <sub>2 27</sub>		16546.6105	–0.0033
28 <sub>3 26</sub>	–	27 <sub>3 25</sub>		16547.0065	0.0026
28 <sub>3 25</sub>	–	27 <sub>3 24</sub>		16547.0066	0.0025
31 <sub>3 29</sub>	–	30 <sub>3 28</sub>		16547.0045	0.0046
31 <sub>3 28</sub>	–	30 <sub>3 27</sub>	16547.0091	16547.0045	0.0046
29 <sub>3 26</sub>	–	28 <sub>3 25</sub>		16547.0090	0.0001
29 <sub>3 27</sub>	–	28 <sub>3 26</sub>		16547.0089	0.0002
30 <sub>3 27</sub>	–	29 <sub>3 26</sub>		16547.0083	0.0008
30 <sub>3 28</sub>	–	29 <sub>3 27</sub>		16547.0083	0.0008
28 <sub>4 25</sub>	–	27 <sub>4 24</sub>		16547.5652	–0.0016
28 <sub>4 24</sub>	–	27 <sub>4 23</sub>		16547.5652	–0.0016
31 <sub>4 27</sub>	–	30 <sub>4 26</sub>		16547.5631	0.0005
31 <sub>4 28</sub>	–	30 <sub>4 27</sub>	16547.5636	16547.5631	0.0005
29 <sub>4 26</sub>	–	28 <sub>4 25</sub>		16547.5676	–0.0040
29 <sub>4 25</sub>	–	28 <sub>4 24</sub>		16547.5676	–0.0040
30 <sub>4 26</sub>	–	29 <sub>4 25</sub>		16547.5669	–0.0033
30 <sub>4 27</sub>	–	29 <sub>4 26</sub>		16547.5669	–0.0033
9 <sub>5 4</sub>	–	8 <sub>5 3</sub>	16547.6546	16547.6519	0.0027
9 <sub>5 5</sub>	–	8 <sub>5 4</sub>		16547.6519	0.0027
10 <sub>5 6</sub>	–	9 <sub>5 5</sub>	16547.7158	16547.7129	0.0029
10 <sub>5 5</sub>	–	9 <sub>5 4</sub>		16547.7129	0.0029
11 <sub>5 6</sub>	–	10 <sub>5 5</sub>	16547.7693	16547.7708	–0.0015

## 8. Appendix

---

**Table 8-2.** (continued)

11 <sub>57</sub>	–	10 <sub>56</sub>		16547.7708	–0.0015
12 <sub>58</sub>	–	11 <sub>57</sub>	16547.8258	16547.8256	0.0002
12 <sub>57</sub>	–	11 <sub>56</sub>		16547.8256	0.0002
13 <sub>59</sub>	–	12 <sub>58</sub>	16547.8789	16547.8774	0.0015
13 <sub>58</sub>	–	12 <sub>57</sub>		16547.8774	0.0015
14 <sub>510</sub>	–	13 <sub>59</sub>	16547.9262	16547.9260	0.0002
14 <sub>59</sub>	–	13 <sub>58</sub>		16547.9260	0.0002
15 <sub>510</sub>	–	14 <sub>59</sub>	16547.9713	16547.9716	–0.0003
15 <sub>511</sub>	–	14 <sub>510</sub>		16547.9716	–0.0003
16 <sub>511</sub>	–	15 <sub>510</sub>	16548.0097	16548.0141	–0.0044
16 <sub>512</sub>	–	15 <sub>511</sub>		16548.0141	–0.0044
28 <sub>524</sub>	–	27 <sub>523</sub>		16548.2835	0.0009
28 <sub>523</sub>	–	27 <sub>522</sub>		16548.2835	0.0009
31 <sub>527</sub>	–	30 <sub>526</sub>		16548.2814	0.0030
31 <sub>526</sub>	–	30 <sub>525</sub>	16548.2844	16548.2814	0.0030
29 <sub>524</sub>	–	28 <sub>523</sub>		16548.2859	–0.0015
29 <sub>525</sub>	–	28 <sub>524</sub>		16548.2859	–0.0015
30 <sub>525</sub>	–	29 <sub>524</sub>		16548.2852	–0.0008
30 <sub>526</sub>	–	29 <sub>525</sub>		16548.2852	–0.0008

<sup>a</sup> Weight is 0.1 in the least-squares fit.

**Table 8-3.** The observed and fitted rovibronic lines in the 581 nm band of the  ${}^2A''-X\ {}^2A''$  electronic transition of  $C_6H_4^+$ .

$N_{KaKc}$	$\nu_{\text{obs}} (\text{cm}^{-1})$	$\nu_{\text{calc}} (\text{cm}^{-1})$	o-c
$1_{11} - 2_{12}$	17213.6180	17213.6146	0.0034
$1_{10} - 2_{11}$		17213.6122	0.0058
$1_{01} - 2_{02}$	17213.5417	17213.5359	0.0058
$2_{12} - 3_{13}$	17213.5145	17213.5174	-0.0029
$2_{11} - 3_{12}$		17213.5137	0.0008
$2_{02} - 3_{03}$	17213.4377	17213.4381	-0.0004
$3_{13} - 4_{14}$	17213.4146	17213.4173	-0.0027
$3_{12} - 4_{13}$		17213.4124	0.0022
$3_{03} - 4_{04}$	17213.3325	17213.3373	-0.0048
$4_{14} - 5_{15}$	17213.3143	17213.3142	0.0001
$4_{13} - 5_{14}$		17213.3081	0.0062
$4_{04} - 5_{05}$	17213.2231	17213.2337	-0.0106
$5_{15} - 6_{16}$	17213.2065	17213.2082	-0.0017
$5_{14} - 6_{15}$		17213.2009	0.0056
$7_{26} - 8_{27}$	17213.1985	17213.2150	-0.0165 <sup>a</sup>
$7_{25} - 8_{26}$		17213.2149	-0.0164 <sup>a</sup>
$5_{05} - 6_{06}$	17213.1221	17213.1271	-0.0050
$6_{16} - 7_{17}$	17213.1054	17213.0993	0.0061 <sup>a</sup>
$6_{15} - 7_{16}$		17213.0907	0.0147 <sup>a</sup>
$6_{06} - 7_{07}$	17213.0125	17213.0176	-0.0051
$7_{17} - 8_{18}$	17212.9911	17212.9875	0.0036 <sup>a</sup>
$7_{16} - 8_{17}$		17212.9777	0.0134 <sup>a</sup>
$9_{28} - 10_{29}$	17212.9621	17212.9814	-0.0193 <sup>a</sup>
$9_{27} - 10_{28}$		17212.9812	-0.0191 <sup>a</sup>
$7_{07} - 8_{08}$	17212.9060	17212.9052	0.0008
$8_{18} - 9_{19}$	17212.8756	17212.8728	0.0028 <sup>a</sup>
$8_{17} - 9_{18}$		17212.8617	0.0139 <sup>a</sup>
$10_{29} - 11_{210}$	17212.8433	17212.8602	-0.0169 <sup>a</sup>
$10_{28} - 11_{29}$		17212.8599	-0.0166 <sup>a</sup>
$8_{08} - 9_{09}$	17212.7846	17212.7899	-0.0053
$9_{19} - 10_{110}$	17212.7541	17212.7551	-0.0010 <sup>a</sup>
$9_{18} - 10_{19}$		17212.7428	0.0113 <sup>a</sup>

## 8. Appendix

**Table 8-3.** (continued)

11 <sub>210</sub> – 12 <sub>211</sub>	17212.7300	17212.7361	-0.0061 <sup>a</sup>
11 <sub>29</sub> – 12 <sub>210</sub>		17212.7357	-0.0057 <sup>a</sup>
9 <sub>09</sub> – 10 <sub>010</sub>	17212.6697	17212.6716	-0.0019
10 <sub>110</sub> – 11 <sub>111</sub>	17212.6331	17212.6345	-0.0014 <sup>a</sup>
10 <sub>19</sub> – 11 <sub>110</sub>		17212.6210	0.0121 <sup>a</sup>
10 <sub>010</sub> – 11 <sub>011</sub>	17212.5477	17212.5505	-0.0028
11 <sub>111</sub> – 12 <sub>112</sub>	17212.5089	17212.5110	-0.0021 <sup>a</sup>
11 <sub>110</sub> – 12 <sub>111</sub>		17212.4963	0.0126 <sup>a</sup>
11 <sub>011</sub> – 12 <sub>012</sub>	17212.4235	17212.4264	-0.0029
12 <sub>112</sub> – 13 <sub>113</sub>	17212.3802	17212.3846	-0.0044 <sup>a</sup>
12 <sub>111</sub> – 13 <sub>112</sub>		17212.3686	0.0116 <sup>a</sup>
14 <sub>213</sub> – 15 <sub>214</sub>	17212.3397	17212.3462	-0.0065 <sup>a</sup>
14 <sub>212</sub> – 15 <sub>213</sub>		17212.3455	-0.0058 <sup>a</sup>
12 <sub>012</sub> – 13 <sub>013</sub>	17212.2984	17212.2994	-0.0010
13 <sub>113</sub> – 14 <sub>114</sub>	17212.2566	17212.2553	0.0013
13 <sub>112</sub> – 14 <sub>113</sub>	17212.2470	17212.2381	0.0089
15 <sub>214</sub> – 16 <sub>215</sub>	17212.2008	17212.2104	-0.0096 <sup>a</sup>
15 <sub>213</sub> – 16 <sub>214</sub>		17212.2096	-0.0088 <sup>a</sup>
13 <sub>013</sub> – 14 <sub>014</sub>	17212.1697	17212.1696	0.0001
14 <sub>114</sub> – 15 <sub>115</sub>	17212.1219	17212.1230	-0.0011
14 <sub>113</sub> – 15 <sub>114</sub>	17212.1096	17212.1046	0.0050
16 <sub>215</sub> – 17 <sub>216</sub>	17212.0632	17212.0717	-0.0085 <sup>a</sup>
16 <sub>214</sub> – 17 <sub>215</sub>		17212.0707	-0.0075 <sup>a</sup>
14 <sub>014</sub> – 15 <sub>015</sub>	17212.0346	17212.0368	-0.0022
15 <sub>115</sub> – 16 <sub>116</sub>	17211.9886	17211.9878	0.0008
15 <sub>114</sub> – 16 <sub>115</sub>	17211.9743	17211.9682	0.0061
15 <sub>015</sub> – 16 <sub>016</sub>	17211.9021	17211.9011	0.0010
16 <sub>116</sub> – 17 <sub>117</sub>	17211.8504	17211.8498	0.0006
16 <sub>115</sub> – 17 <sub>116</sub>	17211.8386	17211.8289	0.0097
16 <sub>016</sub> – 17 <sub>017</sub>	17211.7627	17211.7625	0.0002
17 <sub>117</sub> – 18 <sub>118</sub>	17211.7087	17211.7087	0.0000
17 <sub>116</sub> – 18 <sub>117</sub>	17211.6902	17211.6866	0.0036
17 <sub>017</sub> – 18 <sub>018</sub>	17211.6224	17211.6211	0.0013
18 <sub>118</sub> – 19 <sub>119</sub>	17211.5661	17211.5648	0.0013

**Table 8-3.** (continued)

18 <sub>117</sub> – 19 <sub>118</sub>	17211.5447	17211.5415	0.0032
18 <sub>018</sub> – 19 <sub>019</sub>	17211.4766	17211.4767	-0.0001
19 <sub>119</sub> – 20 <sub>120</sub>	17211.4184	17211.4180	0.0004
19 <sub>118</sub> – 20 <sub>119</sub>	17211.3938	17211.3934	0.0004
19 <sub>019</sub> – 20 <sub>020</sub>	17211.3261	17211.3294	-0.0033
20 <sub>120</sub> – 21 <sub>121</sub>	17211.2709	17211.2682	0.0027
20 <sub>119</sub> – 21 <sub>120</sub>	17211.2411	17211.2424	-0.0013
20 <sub>020</sub> – 21 <sub>021</sub>	17211.1662	17211.1793	-0.0131
21 <sub>121</sub> – 22 <sub>122</sub>	17211.1169	17211.1156	0.0013
21 <sub>120</sub> – 22 <sub>121</sub>	17211.0842	17211.0885	-0.0043
21 <sub>021</sub> – 22 <sub>022</sub>	17211.0265	17211.0262	0.0003
22 <sub>122</sub> – 23 <sub>123</sub>	17210.9655	17210.9600	0.0055
22 <sub>121</sub> – 23 <sub>122</sub>	17210.9274	17210.9317	-0.0043
23 <sub>123</sub> – 24 <sub>124</sub>	17210.8091	17210.8015	0.0076
23 <sub>122</sub> – 24 <sub>123</sub>	17210.7638	17210.7720	-0.0082

<sup>a</sup> Weight is 0.1 in the least-squares fit.

## 8. Appendix

**Table 8-4.** The observed and fitted rovibronic lines in the 581 nm band of the  ${}^2A''-X\ {}^2A''$  electronic transition of  $C_6D_4^+$ .

$N_{KaKc}$	$\nu_{\text{obs}} (\text{cm}^{-1})$	$\nu_{\text{calc}} (\text{cm}^{-1})$	$\text{o-c}$
$5_{05} - 6_{06}$	17217.6289	17217.6227	0.0062
$7_{26} - 8_{27}$	17217.6012	17217.6105	-0.0093
$7_{25} - 8_{26}$		17217.6101	-0.0089
$6_{16} - 7_{17}$	17217.5804	17217.5777	0.0027
$6_{15} - 7_{16}$	17217.5704	17217.5622	0.0082
$6_{06} - 7_{07}$	17217.5229	17217.5221	0.0008
$8_{27} - 9_{28}$	17217.5012	17217.5040	-0.0028
$8_{26} - 9_{27}$		17217.5035	-0.0023
$7_{17} - 8_{18}$	17217.4743	17217.4752	-0.0009
$7_{16} - 8_{17}$	17217.4573	17217.4575	-0.0002
$7_{07} - 8_{08}$	17217.4177	17217.4186	-0.0009
$9_{28} - 10_{29}$	17217.3932	17217.3947	-0.0015
$9_{27} - 10_{28}$		17217.3939	-0.0007
$8_{18} - 9_{19}$	17217.3637	17217.3698	-0.0061
$8_{17} - 9_{18}$	17217.3568	17217.3499	0.0069
$8_{08} - 9_{09}$	17217.3155	17217.3122	0.0033
$10_{29} - 11_{210}$	17217.2811	17217.2824	-0.0013
$10_{28} - 11_{29}$		17217.2814	-0.0003
$9_{19} - 10_{110}$	17217.2508	17217.2616	-0.0108
$9_{18} - 10_{19}$	17217.2446	17217.2395	0.0051
$9_{09} - 10_{010}$	17217.2070	17217.2031	0.0039
$11_{210} - 12_{211}$	17217.1656	17217.1673	-0.0017
$11_{29} - 12_{210}$		17217.1659	-0.0003
$10_{110} - 11_{111}$	17217.1394	17217.1505	-0.0111
$10_{19} - 11_{110}$	17217.1301	17217.1262	0.0039
$10_{010} - 11_{011}$	17217.0959	17217.0910	0.0049
$12_{211} - 13_{212}$	17217.0495	17217.0493	0.0002
$12_{210} - 13_{211}$		17217.0475	0.0020
$11_{111} - 12_{112}$	17217.0262	17217.0365	-0.0103
$11_{110} - 12_{111}$	17217.0119	17217.0100	0.0019
$11_{011} - 12_{012}$	17216.9824	17216.9762	0.0062
$13_{212} - 14_{213}$	17216.9322	17216.9284	0.0038
$13_{211} - 14_{212}$		17216.9261	0.0061

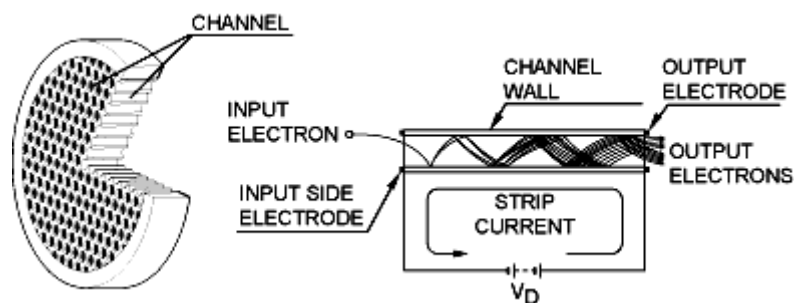


Table 8-4. (continued)

$12_{112} - 13_{113}$	17216.9111	17216.9196	-0.0085
$12_{111} - 13_{112}$	17216.8965	17216.8909	0.0056
$12_{012} - 13_{013}$	17216.8681	17216.8585	0.0096
$14_{213} - 15_{214}$	17216.8123	17216.8047	0.0076
$14_{212} - 15_{213}$		17216.8018	0.0105
$13_{113} - 14_{114}$	17216.7907	17216.7999	-0.0092
$13_{112} - 14_{113}$	17216.7641	17216.7689	-0.0048
$13_{013} - 14_{014}$	17216.7486	17216.7380	0.0106
$15_{214} - 16_{215}$	17216.6837	17216.6780	0.0057
$15_{213} - 16_{214}$		17216.6746	0.0091
$14_{114} - 15_{115}$	17216.6710	17216.6772	-0.0062
$14_{113} - 15_{114}$	17216.6343	17216.6441	-0.0098
$15_{115} - 16_{116}$	17216.5553	17216.5518	0.0035
$15_{114} - 16_{115}$	17216.5064	17216.5165	-0.0101
$16_{116} - 17_{117}$	17216.4264	17216.4234	0.0030
$16_{115} - 17_{116}$	17216.3762	17216.3860	-0.0098
$17_{117} - 18_{118}$	17216.2965	17216.2922	0.0043
$17_{116} - 18_{117}$	17216.2466	17216.2526	-0.0060
$18_{118} - 19_{119}$	17216.1634	17216.1582	0.0052
$18_{117} - 19_{118}$	17216.1083	17216.1163	-0.0080

## 8.4 Micro channel plates

MCP is a specially fabricated plate that amplifies electron signal similar to secondary electron multiplier (SEM). Unlike SEM, MCP has several million independent channels and each channel works as independent electron multiplier. In other words, one can imagine MCP as an assembly of millions miniature SEMs. MCP consists of a two-dimensional periodic array of very-small diameter glass capillaries (channels) fused together and sliced in a thin plate. A single incident particle (ion, electron, photon etc.) enters a channel and emits an electron from the channel wall. Secondary electrons are accelerated by an electric field developed by a voltage applied across the both ends of the MCP. They travel along their parabolic trajectories until they in turn strike the channel surface, thus producing more secondary electrons. This process is repeated many times along the channel; as a result, this cascade process yields a cloud of several thousand electrons, which emerge from the rear of the plate. If two or more MCPs are operated in series, a single input event will generate a pulse of  $10^8$  or more electrons at the output.



**Figure 8-4.** The operational principle of the MCP (from [www.sciner.com/MCP](http://www.sciner.com/MCP)).

Since the individual channels confine the pulse, the spatial pattern of electron pulses at the rear of the plate preserve the pattern (image) particles incident on the front surface. The output signals are typically collected in any of several ways, including metal or multimetal anodes, resistive anode (one- or two- dimensional), wedge and strip anode, Delay-Line Readout or on a phosphor screen deposited on a fiberoptic or other substrate.

Micro channel plates have a combination of unique properties like high gain, high spatial resolution and high temporal resolution. They can be used in a large variety of applications including, imaging spectroscopy, electron spectroscopy and

microscopy, mass spectrometry, astronomy, molecular and atomic collision studies, cluster physics etc. Most of these applications require only some of MCP properties, for example TOF mass spectrometry require high temporal resolution of MCPs, imaging of single atoms in field ion microscopes or X-ray imaging of the Sun require mainly spatial resolution. Particle analysers may be produced by using a MCP detector at the output of a electrostatic and/or magnetic dispersion system. Very high sensitivity optical, UV and EUV and X-ray spectrometers can also be produced with appropriate filtering and dispersive elements. The same micro channel plate technology is used to make visible light image intensifiers for night vision goggles and binoculars.

## 8.5 Publications

- H. Linnartz, D. Pfluger, O. Vaizert, P. Cias, P. Birza, D.Khoroshev, and J.P. Maier, Rotationally resolved  $A^2\Pi_u \leftarrow X^2\Pi_g$  electronic transition of  $\text{NC}_6\text{N}^+$  // J. Chem. Phys. 116 (2002) 924
- P. Birza, T. Motylewski, D. Khoroshev, A. Chirokolava, H. Linnartz, J.P. Maier, Cw cavity ring down spectroscopy in a pulsed planar plasma expansion // Chem. Phys. 283 (2002) 119
- P. Birza, D. Khoroshev, A. Chirokolava, T. Motylewski, J.P. Maier, Lifetime broadening in the gas phase  $B^2\Pi \leftarrow X^2\Pi$  electronic spectrum of  $\text{C}_8\text{H}$  // Chem. Phys. Lett. 382 (2003) 245
- D. Khoroshev, M. Araki, P. Kolek, P. Birza, A. Chirokolava, J.P. Maier, Rotationally resolved electronic spectroscopy of a nonlinear carbon chain radical  $\text{C}_6\text{H}_4^+$  // J. Mol. Spec. 227 (2004) 81

# Rotationally resolved $A^2\Pi_u \leftarrow X^2\Pi_g$ electronic transition of $\text{NC}_6\text{N}^+$

H. Linnartz,<sup>a)</sup> D. Pflüger, O. Vaizert, P. Cias, P. Birza, D. Khoroshev, and J. P. Maier  
*Institute for Physical Chemistry, Klingelbergstrasse 80, CH-4056 Basel, Switzerland*

(Received 17 August 2001; accepted 23 October 2001)

The rotationally resolved  $A^2\Pi_u \leftarrow X^2\Pi_g$  electronic origin band spectrum of dicyanodiacetylene cation,  $\text{NC}_6\text{N}^+$ , has been recorded in the gas phase using frequency-production double modulation spectroscopy in a liquid nitrogen cooled hollow cathode discharge and cavity ring down spectroscopy in a supersonic plasma. The analysis of the complementary results provides accurate molecular parameters for the two spin-orbit components in both electronic states. © 2002 American Institute of Physics. [DOI: 10.1063/1.1427710]

## I. INTRODUCTION

In recent years several cyanopolyacetylene radicals ( $\text{HC}_n\text{N}$ ) have been studied by Fourier transform microwave spectroscopy<sup>1,2</sup> and, following their laboratory detection, species as large as  $\text{HC}_{11}\text{N}$  have been identified by radio astronomy in the interstellar medium.<sup>3</sup> The dicyano derivatives ( $\text{NC}_n\text{N}$ ) may be comparably abundant in space, but are unsuitable for microwave detection due to absence of a dipole moment. In this case accurate spectroscopic information can be obtained from high resolution studies of vibrational or electronic transitions in the gas phase. The latter are available for a series of carbon chain radicals. Examples are the nonpolar  $\text{NC}_5\text{N}$  (Ref. 4) and  $\text{HC}_7\text{H}$ ,<sup>5,6</sup> as well as chains that were already detected in dense interstellar clouds such as  $\text{HC}_6\text{N}$  (Ref. 6) and  $\text{C}_6\text{H}$ .<sup>7</sup> These species are formed in ion-molecule reactions and consequently spectroscopic information on carbon chain ions is needed as well, but high resolution data are rare and pure rotational spectra are limited to a few species.<sup>8</sup>

This is particularly true for the (di)cyanopolyacetylene cations. Electronic spectra have been recorded in neon matrices for  $\text{NC}_{2n}\text{N}^+$  ( $n=2-6$ ) and  $\text{HC}_{2n+1}\text{N}^+$  ( $n=2-6$ ).<sup>9-12</sup> Following these and low resolution emission studies<sup>13-15</sup> the rotationally resolved electronic gas phase spectrum of the cyanodiacetylene ( $\text{HC}_5\text{N}^+$ ) and dicyanoacetylene ( $\text{NC}_4\text{N}^+$ )<sup>16</sup> as well as the cyanotriacetylene ( $\text{HC}_7\text{N}^+$ )<sup>17</sup> were reported. In the present work the rotationally resolved spectrum of the next larger member in the dicyano-series,  $\text{NC}_6\text{N}^+$ , is presented. The results are compared with the results of density functional theory calculations<sup>18</sup> and the spectroscopic parameters available for the iso-electronic chains  $\text{HC}_7\text{N}^+$  (Ref. 17) and  $\text{HC}_8\text{H}^+$ .<sup>19</sup>

## II. EXPERIMENT

The spectra are recorded using two complementary experimental approaches. These are frequency production double modulation (FPM) spectroscopy of a static plasma generated in a discharge cell ( $T_{\text{rot}} \sim 150$  K) and cavity ring-down (CRD) spectroscopy sampling a supersonic planar

plasma ( $T_{\text{rot}} = 15$  K), yielding spectra with significantly different rotational profiles. Both experimental techniques have been described. In the FPM experiment<sup>20</sup> mixtures of 0.5%–0.6% cyanogen/He are discharged in a liquid nitrogen cooled hollow cathode incorporated into a White-type multiple reflection cell ( $L_{\text{tot}} \sim 100$  m). Production modulation is obtained by applying a rectified 17 kHz ac voltage (–500 to 700 V). The laser beam is electro-optically modulated at a radio frequency of 192 MHz and detected by a fast photodiode. Subsequent phase sensitive demodulation of the high frequency portion of the signal during a production cycle gives absorption bands that have a derivativelike shape. The resolution is Doppler limited and typically of the order of 550 MHz.

In the CRD setup<sup>21</sup> the  $\text{NC}_6\text{N}^+$  radicals are formed by a discharge through a high pressure gas pulse (typically 100 mA at –1000 V for a 12 bar backing pressure) of an 0.2% cyanogen/He mixture in the throat of a 3 cm × 300 μm multilayer slit nozzle device. A standard CRD spectrometer is used to detect the signals in direct absorption. The resolution is limited by the bandwidth of the laser to  $\sim 0.035$  cm<sup>–1</sup>. In both experiments iodine spectra are used for an absolute frequency calibration.

## III. RESULTS AND DISCUSSION

An overview scan of the  $A^2\Pi_u \leftarrow X^2\Pi_g$  electronic origin band transition of  $\text{NC}_6\text{N}^+$  recorded by FPM in the discharge cell is shown in Fig. 1. In the range 15 240–15 248 cm<sup>–1</sup> approximately 200 individual absorption lines are resolved. These transitions belong to the *P*-, *Q*- and *R*-branches of two subbands corresponding to the parallel  $A^2\Pi_{3/2} \leftarrow X^2\Pi_{3/2}$  and  $A^2\Pi_{1/2} \leftarrow X^2\Pi_{1/2}$  electronic transitions. The intensity ratio of the two bands is determined by the “spin-orbit temperature” and the value of the spin-orbit splitting ( $A''$ ) in the ground state. The latter is estimated from previous studies to be of the order of  $-40(5)$  cm<sup>–1</sup>,<sup>16</sup> the minus indicating that the  $\Omega = \frac{3}{2}$  spin-orbit component is lower in energy than the  $\Omega = \frac{1}{2}$ . At the high ambient temperature in the cell both spin-orbit components are equally intense. The rotational population is distributed over many levels and the intensity of both *Q*-branches and transitions starting from low *J*-levels is low. Clear band heads, however, are missing. Moreover, the spin-

<sup>a)</sup>Electronic mail: Henricus.Linnartz@unibas.ch

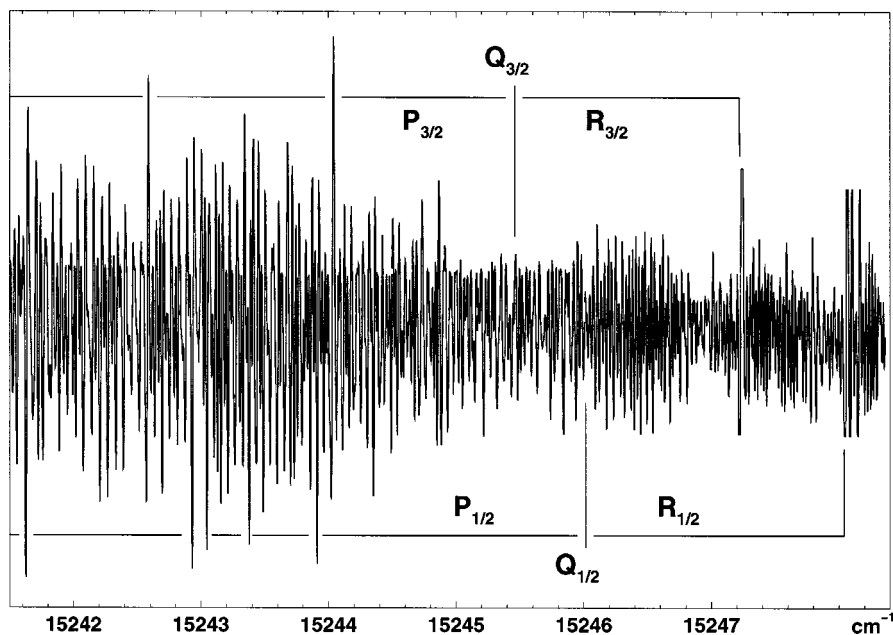


FIG. 1. Rotationally resolved frequency production double modulation absorption spectrum of the  $A^2\Pi_u \leftarrow X^2\Pi_g$  electronic origin band of  $\text{NC}_6\text{N}^+$  measured in a liquid-nitrogen cooled hollow cathode discharge ( $T_{\text{rot}} \sim 150$  K). The  $P$ -,  $Q$ - and  $R$ -branches of the  $A^2\Pi_{3/2} \leftarrow X^2\Pi_{3/2}$  and  $A^2\Pi_{1/2} \leftarrow X^2\Pi_{1/2}$  subbands are indicated.

orbit components overlap as the difference in spin-orbit splittings in ground and excited state,  $\Delta A$ , appears to be small. All these factors together lead to ambiguity in the assignment of the rotational lines. What is missing is a clearly defined starting point. This is provided by the jet spectrum.

In Fig. 2 part of the spectral region of Fig. 1 is shown. The spectrum is recorded by CRD in the plasma expansion. Only the lower subband,  $A^2\Pi_{3/2} \leftarrow X^2\Pi_{3/2}$ , is clearly visible now, as the population of the upper spin-orbit component is low. Besides unresolved  $P$ - and  $R$ -branches,<sup>22</sup> a clear  $Q$ -branch is observed starting at  $15245.46(3)$   $\text{cm}^{-1}$ . This branch is not visible in Fig. 1, but the CRD position allows the assignment of transitions belonging to the  $A^2\Pi_{3/2} \leftarrow X^2\Pi_{3/2}$  subband within  $\pm 1$   $J$  quantum numbering in the FPM spectrum. The band gap is  $\sim 10B$  [with  $B \sim 0.019$   $\text{cm}^{-1}$  (Ref. 18)] reflecting that the lowest rotational transitions cor-

respond to  $P(\frac{5}{2})$  and  $R(\frac{3}{2})$ . Adjacent transitions are separated by  $\sim 2B$ . In this way more than 80(40) transitions have been assigned in  $P(R)$ -branch of the  $A^2\Pi_{3/2} \leftarrow X^2\Pi_{3/2}$  band with  $J$ -values up to 90.5.<sup>23</sup> These values are then fitted with PGopher<sup>24</sup> using  $\nu_0$ ,  $B''_0$ ,  $B'_0$ ,  $D''_0$  and  $D'_0$  as variables yielding a rms of  $0.002$   $\text{cm}^{-1}$ . The resulting constants are listed in Table I. The value for  $B''_0 = 0.0187533(55)$   $\text{cm}^{-1}$  is close to the  $B_e$ -value of  $0.01867$   $\text{cm}^{-1}$  as obtained from density functional calculations.<sup>18</sup> A simulation using these constants proves that the stronger feature in Fig. 1 at  $15247.23(3)$   $\text{cm}^{-1}$  corresponds to the  $R$ -branch band head of the  $A^2\Pi_{3/2} \leftarrow X^2\Pi_{3/2}$  system. A similar feature is observed at  $15247.85$   $\text{cm}^{-1}$  and is tentatively assigned to the  $R$ -branch band head of the second spin-orbit system.

The lines that are left over are mainly due to the  $\Omega = \frac{1}{2}$

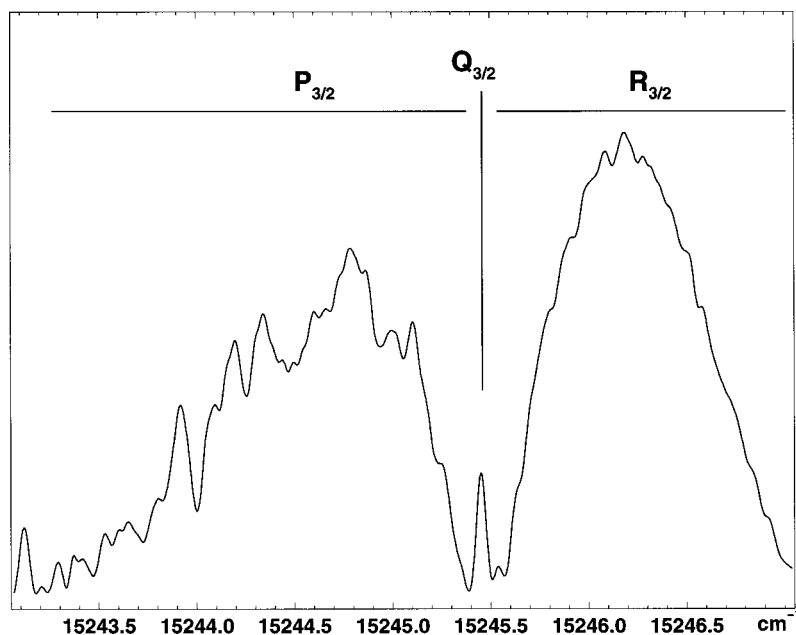


FIG. 2. Cavity ring down absorption spectrum of the  $A^2\Pi_{3/2} \leftarrow X^2\Pi_{3/2}$  electronic origin band of  $\text{NC}_6\text{N}^+$ , recorded through a supersonic plasma. The second spin-orbit component is not visible at the low temperature in the jet ( $T_{\text{rot}} \sim 15$  K). The  $Q$ -branch position is used to assign the FPM spectrum.

TABLE I. Molecular constants (in  $\text{cm}^{-1}$ ) for the  $A^2\Pi_{3/2}-X^2\Pi_{3/2}$  and for the  $A^2\Pi_{1/2}-X^2\Pi_{1/2}$  electronic origin band transition of  $\text{NC}_6\text{N}^+$ . The molecular parameters for the  $A^2\Pi_u-X^2\Pi_g$  electronic origin band transition of the iso-electronic  $\text{HC}_7\text{N}^+$  (Ref. 17) and  $\text{HC}_8\text{H}^+$  (Ref. 19) species are listed for comparison.

	$\text{NC}_6\text{N}^+$		$\text{HC}_7\text{N}^+$	$\text{HC}_8\text{H}^+$
	$\Omega=3/2$	$\Omega=1/2$	$\Omega=3/2$	$\Omega=3/2$ and $1/2$
$B_0''$	0.018 753 3(55)	0.018 707(19)	0.018 966 5(71)	0.019 077 9(93)
$D_0''$	$6.7(15)\cdot 10^{-9}$	$6.2(38)\cdot 10^{-9}$		
$B_0'$	0.018 558 5(56)	0.018 565(19)	0.018 773 1(72)	0.018 867 3(94)
$D_0'$	$7.1(16)\cdot 10^{-9}$	$8.3(39)\cdot 10^{-9}$		
$\Delta B$	-0.00019	-0.00014	-0.00019	-0.00021
$\Delta A$	+ 0.56		-2.04	-3.00
$\nu_0$	15 245.737(1)		14 925.423(4)	14 143.1815(5)

component. The rotational assignment is problematic now as information on the  $Q$ -branch of the  $A^2\Pi_{1/2}-X^2\Pi_{1/2}$  band is missing. The difference between the band heads, however, indicates that the  $Q_{1/2}$ -branch is expected around  $15\,246.1\text{ cm}^{-1}$ . In addition, only minor differences between the rotational constants for the two spin-orbit systems are expected. In previous studies transitions originating from different spin-orbit components were fitted with one single set of rotational parameters.<sup>7,16,19</sup> In the present experiment this turns out not to be possible. However, as long as the effect of spin uncoupling is small, i.e.,  $2BJ \ll |A|$ ,  $B$  is best replaced by effective parameters  $B_{\text{eff}}(^2\Pi_{1/2})$  and  $B_{\text{eff}}(^2\Pi_{3/2})$ . In second order perturbation theory the difference  $\Delta B_{\text{eff}}$  is given by

$$\Delta B_{\text{eff}} = \frac{2B^2}{\bar{A}}, \quad (1)$$

where  $\bar{A} = A - 2B$ .<sup>25</sup>  $\bar{A}$  is expected to be of the order of  $-40(5)\text{ cm}^{-1}$  (Ref. 16) which puts an additional constraint to the fit. The line positions and most likely assignment for

transitions belonging to the  $A^2\Pi_{1/2}-X^2\Pi_{1/2}$  system are available from (Ref. 26). The resulting molecular parameters are given in Table I. The quality of the fit will be worse as only a few transitions share a common level (rms  $\sim 0.004\text{ cm}^{-1}$ ).<sup>26</sup> Nevertheless, using Eq. (1) an  $A''$ -value between  $-15$  and  $-32\text{ cm}^{-1}$  is calculated.<sup>27</sup> The simulation confirms that the band head position coincides with the feature at  $15\,247.85\text{ cm}^{-1}$ .

The spectral features of  $\text{NC}_6\text{N}^+$  are expected to be qualitatively similar to those of the iso-electronic cyanotriacetylene cation<sup>17</sup> and tetraacetylene cation.<sup>19</sup> The molecular parameters of the  $A^2\Pi_u-X^2\Pi_g$  electronic origin bands of these two ions are listed in Table I as well. These bands are shifted to lower energy, by  $320\text{ cm}^{-1}$  for  $\text{HC}_7\text{N}^+$  and by  $1103\text{ cm}^{-1}$  for  $\text{HC}_8\text{H}^+$ . The  $\Delta A$  value of  $\text{HC}_7\text{N}^+$  ( $-2.04\text{ cm}^{-1}$ ) is comparable to that of  $\text{HC}_8\text{H}^+$  ( $-3.00\text{ cm}^{-1}$ ), but the corresponding value for  $\text{NC}_6\text{N}^+$  is significantly smaller and, moreover, is positive ( $+0.56\text{ cm}^{-1}$ ). This value, however, is very close to the  $\Delta A = +0.53\text{ cm}^{-1}$  found for  $\text{NC}_4\text{N}^+$ .<sup>16</sup> There it was concluded that this anomaly is due to a spin-orbit induced interaction of the upper  $A^2\Pi_{1/2}$  electronic state with another low lying electronic state, presumably of  $^2\Sigma$  character, whereas the  $A^2\Pi_{3/2}$  state is not affected. This becomes clear from the different values for  $\Delta B = B_0' - B_0''$ : for the  $\Omega = \frac{3}{2}$  component a value of  $0.000\,19\text{ cm}^{-1}$  is found, similar to the values determined for  $\text{HC}_7\text{N}^+$  ( $0.000\,19\text{ cm}^{-1}$ ) and  $\text{HC}_8\text{H}^+$  ( $0.000\,21\text{ cm}^{-1}$ ), but for  $\Omega = \frac{1}{2}$  the value decreases to  $0.000\,14\text{ cm}^{-1}$ . The second-order spin-orbit contribution to the rotational constant for a  $\Pi$  state is given by<sup>28,29</sup>

$$B^{(2)} = \sum_{n \neq 0} \frac{4B^2}{E_0^0 - E_n^0}. \quad (2)$$

With  $|\Delta E| = 40\text{ cm}^{-1}$  this gives  $B^{(2)} \sim 0.000\,04\text{ cm}^{-1}$ , i.e., an unperturbed value for  $\Delta B$  of  $0.000\,18\text{ cm}^{-1}$ , close to the value of the other spin-orbit component.

In the case of  $\text{NC}_4\text{N}^+$  it was also found that the  $^2\Sigma-^2\Pi$  interaction removes the degeneracy of the  $e$ - and

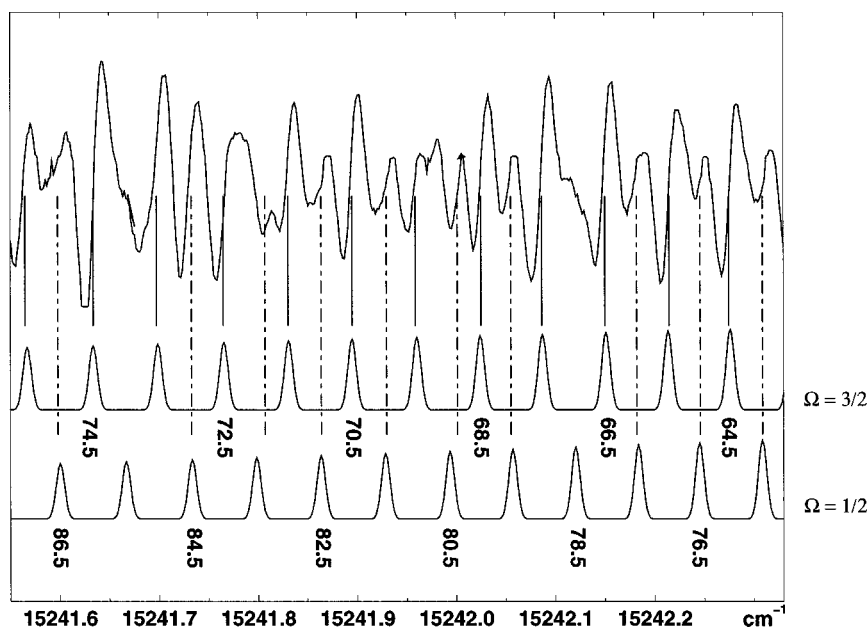


FIG. 3. High  $J$ -level transitions with their typical  $1f$  derivative line shapes recorded in the FPM experiment. The simulated spectrum is shown for both spin-orbit components. There is no evidence for  $\Lambda$ -doubling (see the text).

$f$ -symmetry, resulting in a resolvable  $\Lambda$ -doubling. This effect is not observed here. In Fig. 3 part of the  $P$ -branch range for high  $J$ -levels in both spin-orbit components is shown. The simulated spectrum is given as well. Clearly, there is no evidence for  $\Lambda$ -doubling within the experimental resolution: the size of the splitting would have been  $J$ -dependent and the expected 2:1 spin-statistical alternation is lacking. This is also expected: the rotational constant of  $\text{NC}_6\text{N}^+$  is 2.5 times smaller than that of  $\text{NC}_4\text{N}^+$  ( $\sim 0.044 \text{ cm}^{-1}$ ) and since the  $\Lambda$ -type doubling constants  $p$  and  $q$  are proportional to  $B$  and  $B^2$ , respectively, splittings will be considerably smaller.

## ACKNOWLEDGMENTS

This work has been supported by the Swiss National Science Foundation, Project No. 20-63459.00. One of the authors (H.L.) also acknowledges support from FOM (Fundamenteel Onderzoek der Materie).

- <sup>1</sup>M. C. McCarthy, J. U. Grabow, M. J. Travers, W. Chen, C. A. Gottlieb, and P. Thaddeus, *Astrophys. J.* **494**, L231 (1998).
- <sup>2</sup>M. C. McCarthy and P. Thaddeus, *Chem. Soc. Rev.* **30**, 177 (2001).
- <sup>3</sup>M. B. Bell, P. A. Feldman, M. J. Travers, M. C. McCarthy, C. A. Gottlieb, and P. Thaddeus, *Astrophys. J.* **483**, L61 (1997).
- <sup>4</sup>H. Linnartz, O. Vaizert, P. Cias, L. Grüter, and J. P. Maier, *Chem. Phys. Lett.* **345**, 89 (2001).
- <sup>5</sup>C. D. Ball, M. C. McCarthy, and P. Thaddeus, *J. Chem. Phys.* **112**, 10149 (2000).
- <sup>6</sup>O. Vaizert, T. Motylewski, M. Wyss, E. Riaplov, H. Linnartz, and J. P. Maier, *J. Chem. Phys.* **114**, 7918 (2001).
- <sup>7</sup>H. Linnartz, T. Motylewski, O. Vaizert, J. P. Maier, A. J. Apponi, M. C. McCarthy, C. A. Gottlieb, and P. Thaddeus, *J. Mol. Spectrosc.* **197**, 1 (1999).
- <sup>8</sup>C. A. Gottlieb, A. J. Apponi, M. C. McCarthy, P. Thaddeus, and H. Linnartz, *J. Chem. Phys.* **113**, 1910 (2000).

- <sup>9</sup>J. Agreiter, A. M. Smith, M. Härtle, and V. Bondybey, *Chem. Phys. Lett.* **225**, 87 (1994).
- <sup>10</sup>D. Forney, P. Freivogel, J. Fulara, and J. P. Maier, *J. Phys. Chem.* **102**, 1510 (1995).
- <sup>11</sup>J. Agreiter, A. M. Smith, and V. Bondybey, *Chem. Phys. Lett.* **241**, 317 (1995).
- <sup>12</sup>A. M. Smith, J. Agreiter, and V. Bondybey, *Chem. Phys. Lett.* **244**, 379 (1995).
- <sup>13</sup>E. Kloster-Jensen, J. P. Maier, O. Marthaler, and M. Mohraz, *J. Chem. Phys.* **71**, 3125 (1979).
- <sup>14</sup>G. Bieri, E. Kloster-Jensen, S. Kvisle, J. P. Maier, and O. Mathaler, *J. Chem. Soc., Faraday Trans.* **76**, 676 (1980).
- <sup>15</sup>J. P. Maier, L. Misev, and F. Thommen, *J. Phys. Chem.* **86**, 54 (1982).
- <sup>16</sup>W. E. Sinclair, D. Pfluger, and J. P. Maier, *J. Chem. Phys.* **111**, 9600 (1999).
- <sup>17</sup>W. E. Sinclair, D. Pfluger, D. Verdes, and J. P. Maier, *J. Chem. Phys.* **112**, 8899 (2000).
- <sup>18</sup>S. Lee, *J. Phys. Chem.* **100**, 13959 (1996).
- <sup>19</sup>D. Pfluger, T. Motylewski, H. Linnartz, W. E. Sinclair, and J. P. Maier, *Chem. Phys. Lett.* **329**, 29 (2000).
- <sup>20</sup>W. E. Sinclair, D. Pfluger, H. Linnartz, and J. P. Maier, *J. Chem. Phys.* **110**, 296 (2000).
- <sup>21</sup>T. Motylewski and H. Linnartz, *Rev. Sci. Instrum.* **70**, 1305 (1999).
- <sup>22</sup>No rotational resolution has been obtained, presumably because of residual Doppler broadening.
- <sup>23</sup>See EPAPS Document No. E-JCPSA6-116-004204 for a list with line positions and observed-calculated values. This document may be retrieved via the EPAPS homepage (<http://www.aip.org/pubserv/epaps.html>) or from <ftp.aip.org> in the director /epaps/. See the EPAPS homepage for more information.
- <sup>24</sup>C. M. Western, School of Chemistry, University of Bristol, UK, PGOPHER, 1994 and 1998.
- <sup>25</sup>H. W. Kroto, *Molecular Rotation Spectra* (Wiley, New York, 1975), p. 232.
- <sup>26</sup>See Ref. 23.
- <sup>27</sup>Shifting the rotational assignment by  $\pm 1 J$  gives values of  $-7$  and  $-115 \text{ cm}^{-1}$ .
- <sup>28</sup>J. H. van Vleck, *Rev. Mod. Phys.* **23**, 213 (1951).
- <sup>29</sup>R. F. Curl, *Mod. Phys.* **9**, 585 (1965).



Table I: Frequencies (in  $\text{cm}^{-1}$ ) and rotational assignments for the  $A^2\Pi_u-X^2\Pi_g$  electronic origin band transition of  $\text{NC}_6\text{N}^+$  for  $\Omega = \frac{3}{2}$ .

$P_{\frac{3}{2}}$ -branch					$R_{\frac{3}{2}}$ -branch				
J	Obs.	o-c	Obs.	o-c	J	Obs.	o-c	Obs.	o-c
1.5			--		46.5	15243.335	2	15246.781	2
2.5	15245.383	-2	15245.571	0	47.5	15243.275	-3	--	
3.5	15245.345	-2	15245.606	-1	48.5	15243.220	-2	15246.815	-1
4.5	--		15245.644	2	49.5	15243.166	0		
5.5	--		--		50.5	15243.111	2		
6.5	15245.225	-5	15245.714	2	51.5	15243.054	2		
7.5	15245.190	0	15245.747	1	52.5	15242.999	4		
8.5	15245.153	4	15245.778	-3	53.5	15242.939	2		
9.5	15245.109	0	--		54.5	15242.883	4		
10.5	--		15245.849	2	55.5	15242.821	1		
11.5	15245.027	1	--		56.5	15242.760	-2		
12.5	15244.987	2	15245.913	1	57.5	15242.701	-1		
13.5	15244.942	-1	15245.947	2	58.5	15242.643	1		
14.5	15244.895	-5	15245.975	-1	59.5	15242.581	-1		
15.5	15244.855	-2	15246.007	0	60.5	15242.523	1		
16.5	15244.811	-3	15246.041	3	61.5	15242.461	0		
17.5	15244.771	1	15246.069	0	62.5	15242.399	-1		
18.5	15244.726	0	15246.099	0	63.5	15242.340	2		
19.5	15244.681	0	15246.131	3	64.5	15242.275	-1		
20.5	15244.631	-6	15246.158	0	65.5	15242.215	2		
21.5	15244.592	1	15246.188	1	66.5	15242.150	-1		
22.5	15244.545	-1	15246.214	-1	67.5	15242.086	-1		
23.5	15244.497	-3	15246.244	1	68.5	15242.025	1		
24.5	15244.448	-5	15246.272	1	69.5	15241.959	-1		
25.5	15244.414	8	15246.297	-1	70.5	15241.895	0		
26.5	15244.359	0	15246.327	2	71.5	15241.830	0		
27.5	15244.312	1	15246.351	-1	72.5	15241.765	0		
28.5	15244.262	-1	15246.377	-1	73.5	15241.698	-2		
29.5	15244.215	0	15246.403	-1	74.5	15241.634	1		
30.5	15244.171	5	15246.428	-1	75.5	15241.563	-4		
31.5	15244.120	3	15246.455	1	76.5	--			
32.5	15244.071	3	15246.477	-1	77.5	15241.431	-2		
33.5	--		15246.502	0	78.5	--			
34.5	15243.968	1	15246.525	-1	79.5	15241.299	2		
35.5	15243.917	0	15246.549	0	80.5	15241.228	-1		
36.5	15243.866	1	15246.571	-1	81.5	15241.161	1		
37.5	15243.815	1	15246.593	-2	82.5	15241.089	-2		
38.5	15243.760	-2	15246.615	-2	83.5	15241.020	-1		
39.5	15243.709	-1	15246.640	1	84.5	15240.951	0		
40.5	--		15246.658	-2	85.5	15240.880	0		
41.5	15243.604	0	15246.683	2	86.5	15240.809	0		
42.5	15243.549	-2	15246.703	2	87.5	15240.737	-1		
43.5	15243.496	-1	15246.720	-1	88.5	15240.666	0		
44.5	15243.443	0	15246.740	-1	89.5	15240.598	4		
45.5	15243.385	-3	15246.762	2	90.5	15240.523	1		

Table II: Frequencies (in  $\text{cm}^{-1}$ ) and rotational assignments for the  $A^2\Pi_u-X^2\Pi_g$  electronic origin band transition of  $\text{NC}_6\text{N}^+$  for  $\Omega = \frac{1}{2}$ .

P $_{\frac{1}{2}}$ -branch		R $_{\frac{1}{2}}$ -branch		P $_{\frac{1}{2}}$ -branch			R $_{\frac{1}{2}}$ -branch		
J	Obs.	o-c	Obs.	o-c	J	Obs.	o-c	Obs.	o-c
0.5->			--		62.5	15243.085	5		
<-22.5	--		--		63.5	15243.029	6		
23.5	--		15246.851	-7	64.5	--			
24.5	--		15246.885	-2	65.5	15242.909	1		
25.5	--		15246.915	-2	66.5	--			
26.5	--		15246.947	1	67.5	15242.797	6		
27.5	--		15246.972	-3	68.5	15242.727	-5		
28.5	--		15247.005	1	69.5	15242.675	2		
29.5	--		15247.034	2	70.5	15242.614	1		
30.5	--		15247.062	2	71.5	--			
31.5	--		15247.092	4	72.5	--			
32.5	--		15247.117	2	73.5	15242.431	0		
33.5	--		15247.144	2	74.5	--			
34.5	--		15247.172	3	75.5	15242.309	1		
35.5	--		15247.197	2	76.5	15242.246	0		
36.5	--		--		77.5	15242.179	-5		
37.5	--		--		78.5	--			
38.5	--		15247.274	1	79.5	15242.053	-4		
39.5	--		15247.300	2	80.5	15242.001	8		
40.5	--		15247.323	0	81.5	15241.930	1		
41.5	--		15247.346	-1	82.5	15241.864	0		
42.5	--		15247.369	-2	83.5	15241.807	8		
43.5	--		15247.393	-2	84.5	15241.729	-4		
44.5	--		15247.415	-3	85.5	--			
45.5	15243.989	-6	15247.439	-2	86.5	15241.594	-7		
46.5	15243.945	1	15247.464	0	87.5	15241.530	-4		
47.5	15243.891	-1	15247.487	1	88.5	--			
48.5	15243.842	1	15247.510	2	89.5	--			
49.5	15243.797	8			90.5	15241.331	1		
50.5	15243.739	3			91.5	15241.267	6		
51.5	--				92.5	15241.192	0		
52.5	15243.626	-4			93.5	15241.123	1		
53.5	--				94.5	15241.051	-1		
54.5	15243.525	2			95.5	15240.972	-9		
55.5	15243.465	-4			96.5	15240.903	-7		
56.5	15243.406	-8			97.5	--			
57.5	15243.359	-1			98.5	15240.755	-11		
58.5	15243.308	4			99.5	15240.700	7		
59.5	15243.242	-7			100.5	15240.626	7		
60.5	15243.192	-1			101.5	15240.549	4		
61.5	15243.138	1			102.5	15240.473	2		

# Cw cavity ring down spectroscopy in a pulsed planar plasma expansion

P. Birza, T. Motylewski, D. Khoroshev, A. Chirokolava, H. Linnartz, J.P. Maier\*

*Institute for Physical Chemistry, University of Basel, Klingelbergstrasse 80, CH-4056 Basel, Switzerland*

Received 24 January 2002; accepted 15 February 2002

## Abstract

A cw cavity ring down spectrometer has been constructed with the aim to record electronic spectra of rotationally cold carbon chain radicals at high spectral resolution in direct absorption. The radicals are generated in a discharge of a high pressure gas pulse of acetylene in helium in a multilayer slit nozzle. A passive cavity mode locking scheme is used to handle refractive index changes inside the cavity caused by gas pulse and plasma fluctuations. The performance is demonstrated on the rotationally resolved origin band spectrum of the  $A^2\Pi_g - X^2\Pi_u$  electronic transition of the triacetylene cation,  $HC_6H^+$ , around  $16654.7\text{ cm}^{-1}$ . © 2002 Elsevier Science B.V. All rights reserved.

## 1. Introduction

High resolution spectra of unsaturated carbon chain radicals are of interest in view of their role in interstellar hydrocarbon chemistry. Species of the form  $C_nH$ ,  $C_nN$ ,  $HC_{2n+1}N$  and  $H_2C_n$ , with chains containing as many as 11 carbon atoms, have been identified in the dense interstellar medium with the aid of laboratory Fourier transform microwave spectroscopy [1]. It has been argued that electronic transitions of such chains may be among the carriers of unidentified absorption features in diffuse interstellar clouds [2]. The first experimental indication of this came from observations of the electronic absorption spectra of mass-selected carbon

species in neon matrices [3], but owing to solvation effects, the absorption bands exhibit a shift relative to the corresponding gas phase spectra. The latter are now available from a series of experiments on supersonic plasma expansions, using photo-detachment [4], REMPI-TOF [5], and cavity ring down (CRD) [6] spectroscopy with pulsed laser systems. The frequency resolution in these experiments is typically of the order of  $0.035\text{ cm}^{-1}$  or worse. In a single-mode cw laser experiment a much higher resolution can be obtained and with this aim a cw cavity ring down setup has been constructed.

Cavity ring down spectroscopy has become a powerful tool for the study of the structural and dynamical properties of molecules in the gas phase. In a series of recent review articles [7–9] a number of useful applications is listed. One of the reasons for this success is the conceptual simplicity

\* Corresponding author. Fax: +41-61-267-38-55.

E-mail address: [j.p.maier@unibas.ch](mailto:j.p.maier@unibas.ch) (J.P. Maier).

of a CRD experiment [10]. A small fraction of laser light is coupled into an optical cavity of length  $L$  consisting of two mirrors with a reflectivity  $R \sim 99.99\%$  or better. The rate of light leaking out of the cavity has an envelope which is simply a first order exponential decay,  $\exp(-t/\tau)$ . The ring down time  $\tau$  is given by  $L/[c(1 - R + \alpha l)]$ , where  $c$  is the speed of light and  $\alpha l$  reflects the absorbance for a sample present in the cavity with absorption coefficient  $\alpha$  and length  $l$ . That is, the ring down time reflects the rate of absorption rather than its magnitude and as such it is independent of power fluctuations. In addition, very long absorption pathlengths are obtained by confining light tens of microseconds to the cavity. This increases the sensitivity considerably and absorption values as small as  $10^{-6}$  per pass have been detected.

In conventional CRD experiments pulsed lasers are used; each light pulse induces a ring down event. In cw experiments this is not the case and more complicated detection schemes must be applied; either by measuring the phase retardation of an amplitude modulated cw laser [11] or by analysing the exponential decay after switching off the laser beam with a fast optical switch [12–17]. In addition, the cavity has to be in resonance with the laser wavelength, because the bandwidth is generally too narrow to excite more than one cavity mode at a time. For this reason several active tracking schemes have been developed [13,14,16], but in a pulsed jet experiment – as it is the case here – such schemes do not work: the gas pulse changes the refraction index, effectively changing the optical length of the cavity, pushing it out of resonance. This effect is further enhanced when plasma fluctuations cause additional instabilities. In this case a passive scheme for mode locking must be used, as it was introduced by Quack and coworkers [15,17].

In this contribution the experimental details are described of a cw CRD setup capable of detecting unstable carbon chains generated in a pulsed supersonic planar plasma expansion. The performance is discussed on the example of a rotationally resolved electronic spectrum of the triacetylene cation,  $\text{HC}_6\text{H}^+$ .

## 2. Experimental

The carbon chain radicals are generated by applying a 500  $\mu\text{s}$  high voltage pulse ( $-600$  V, 100 mA) to a 1 ms high pressure gas pulse of a 0.5% HCCH/He mixture that is expanded through a 3 cm  $\times$  200  $\mu\text{m}$  slit with a backing pressure of 10 to 12 bar. The system has been used in other studies (see e.g. [18]) and combines high molecular densities and relatively large absorption path lengths with an effective adiabatical cooling. In addition, the effective resolution is increased compared to pinhole expansions due to a reduced Doppler broadening parallel to the slit. A further reduction is obtained by using a multichannel body. A 3D picture of the nozzle is shown in Fig. 1 together with a short description of its operation. More details are available in [19].

Fig. 2 shows the whole experimental setup. The light of a single mode ring dye laser (Coherent, cw-899 autoscan), pumped by a 6 W solid state laser, is guided through an acousto-optical modulator (AOM). The first order deflection is focused into the ring down cavity via a lens that matches a  $\text{TEM}_{00}$  cavity mode, where it crosses the planar plasma expansion 6 mm downstream. The CRD mirrors (1 m plano/convex,  $R > 99.995\%$ ) are mounted in a mechanically stable holder at a distance of  $L = 32$  cm. A system of internal diaphragms facilitates the alignment and He-curtains protect the mirrors during jet operation from pollution.

A strong transmission occurs only when cavity and laser wavelength are mode matched. To achieve this a passive mode locking system has been used, similar to the method described in [15,17], with several small modifications. One of the mirrors is mounted on a piezo element and by applying a periodical (30 Hz) triangular shaped voltage to the element the cavity length is modulated. The amplitude is chosen in such a way that it corresponds to at least two free spectral ranges of the laser frequency, i.e. the cavity is at least four times in resonance with the laser during one period (Fig. 3). A resonance results in a maximum of transmitted light intensity after the cavity and is monitored using an oscilloscope. When the intensity reaches a certain threshold, a trigger signal is

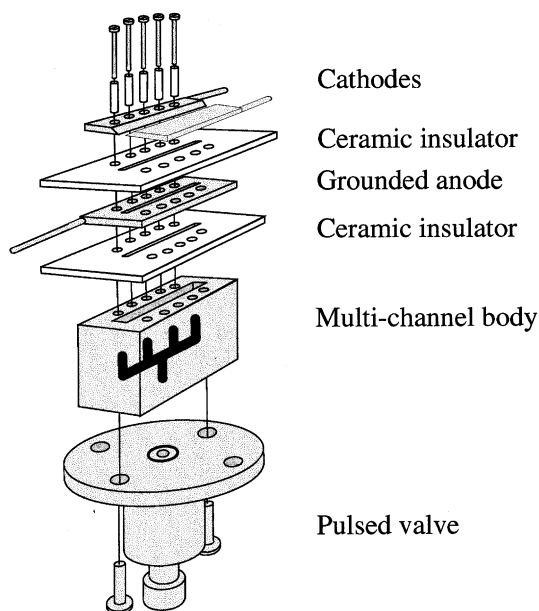


Fig. 1. Artist's view of the high pressure slit nozzle discharge. The orifice consists of two sharp stainless steel jaws (that form the actual slit), a ceramic insulator, a slotted metal plate (grounded) and a second ceramic insulator. Both insulators and metal parts are mounted to the body of the nozzle using electrically isolated screws. A pulsed negative high voltage is applied to the jaws via ballast resistors at the moment that a high pressure gas pulse expands through the channel. The discharge strikes to the grounded plate, localising the reaction zone to a region upstream of the expansion. The body is floating and connected to an electromagnetic driven pulsed valve. A multi-channel system inside the nozzle regulates the gas flow towards the slit and allows a further reduction of the Doppler broadening.

generated that switches off the AOM; the laser beam is interrupted and a ring down event is initiated.

The following detection scheme is used to guarantee that plasma pulse and ring down event coincide (Fig. 3). The data acquisition programme chooses via a simple algorithm the transmission that is strongest and closest to the middle of the ramp voltage. This defines  $t_0$ . The exact ramp voltage at which this cavity resonance occurs is used to define a 300  $\mu\text{s}$  time window at the same ramp voltage in the next cycle. (In order to minimise hysteresis effects of the piezo element, only transmissions on positive or negative ramps are used.) It also defines a delay at which gas and

discharge pulse are activated, in such a way that the plasma expansion coincides with the time window: when a ring down event occurs it automatically samples the plasma. The new resonance defines  $t_1$  and is used to predict the next resonance around  $t_2$ , etc., effectively chasing the resonance. To further increase the sensitivity, only every second cycle is used to trigger gas and discharge pulse. The plasma free ring down event ( $\tau_{\text{reference}}$ ) is then used for background subtraction. This means that with a 30 Hz periodic modulation, 15 ring down events with plasma and 15 ring down events without plasma are measured. The major part of the predicted resonances is within the 300  $\mu\text{s}$  time window, but due to external instabilities the procedure might fail. In this case the data acquisition programme checks the whole ramp, defines a new  $t_0$  and restarts predicting the position of the next resonance. During this short time (3 cycles) only a few data points are lost.

The transmission after the ring-down cavity is focused via a narrow band pass filter onto a broad wavelength band Si-photodiode and recorded in real-time linux using a 12 bit ADC card and a COMEDI driver [20]. The complete decay curve is fitted to an exponential defining  $\tau$ . The CRD spectrum is obtained by recording  $(1/\tau_{\text{plasma}} - 1/\tau_{\text{reference}})$  while scanning the laser. Typical ring down times are  $\tau = 27 \mu\text{s}$ . This is equivalent to approximately 25'000 passes through the plasma or an effective absorption pathlength of 760 m.

### 3. Results

In the lower trace of Fig. 4 the rotationally resolved origin band of the  $A^2\Pi_g - X^2\Pi_u$  electronic transition of  $\text{HC}_6\text{H}^+$  is shown. The same transition has been studied in detail before in a liquid nitrogen cooled hollow-cathode discharge cell applying frequency-plasma double modulation (FPM) spectroscopy [21] and is shown for comparison in the upper trace of Fig. 4. At the high ambient temperature in the cell (approximately 150–200 K) the band system is found to comprise the two  $A^2\Pi_{3/2} - X^2\Pi_{3/2}$  and  $A^2\Pi_{1/2} - X^2\Pi_{1/2}$  subbands, partially overlapping and separated by the difference in spin-orbit constants in ground and elec-

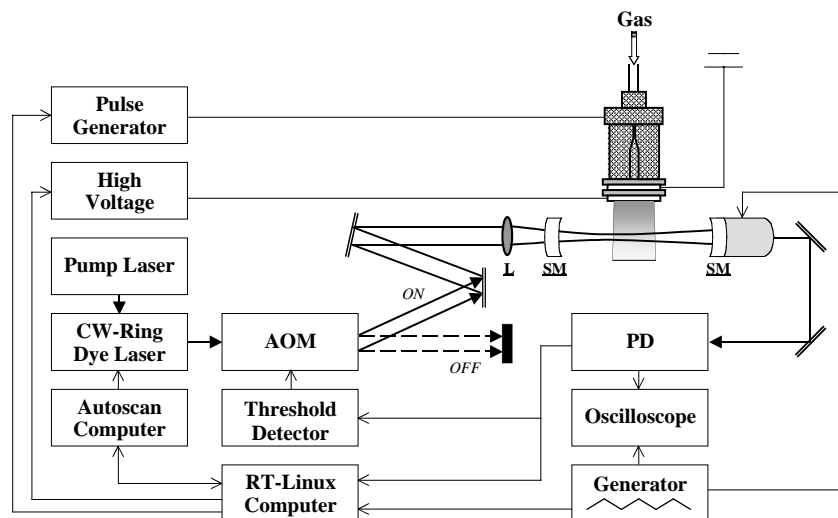


Fig. 2. Schematic of the experimental setup. Details are given in the text.

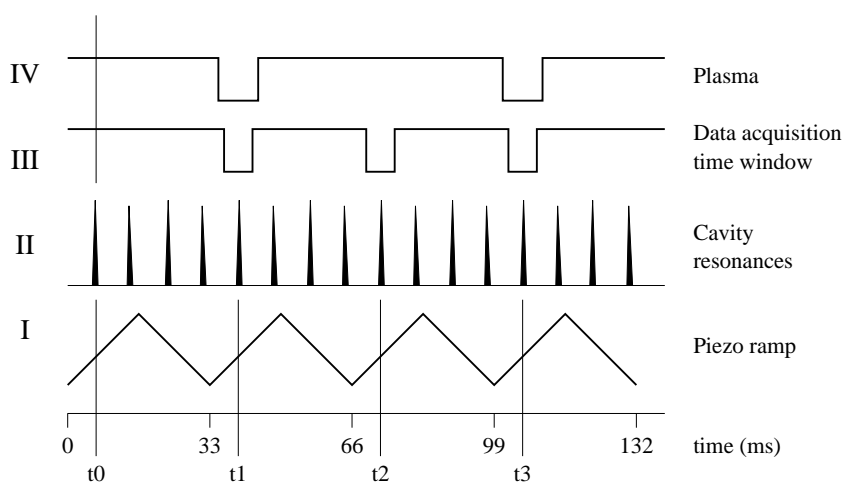


Fig. 3. Timing and triggering scheme. (I) A 30 Hz ramp is applied to a piezo element. (II) The photo diode shows when cavity resonances occur. The data-acquisition programme chooses the transmission closest to the middle of the ramp, defining  $t_0$  and the ramp voltage for which the resonance occurs. When the transmission intensity exceeds a certain threshold, the AOM is switched off and a ring down event is induced. (III) The programme defines a 300  $\mu$ s time window in which the next resonance is expected. In order to circumvent hysteresis effects only signals on positive or negative ramps are taken. The example is shown for a positive ramp. (IV)  $t_0$  is also used to trigger the gas and discharge pulse every second ramp. The plasma free ring down event is used for background subtraction.

tronically excited state. Both subbands show strong P- and R-branches, with clear red shaded bandheads and with a weak Q-branch. The spectral simplification upon jet cooling is striking: the jet spectrum displays only one single band. It

consists of well-defined P- and R-branches and a strong Q-branch (Fig. 4). The lower  $J$ -levels are markedly stronger and no band head is observed. This is consistent with the low temperature in the supersonic jet. From the relative intensity of

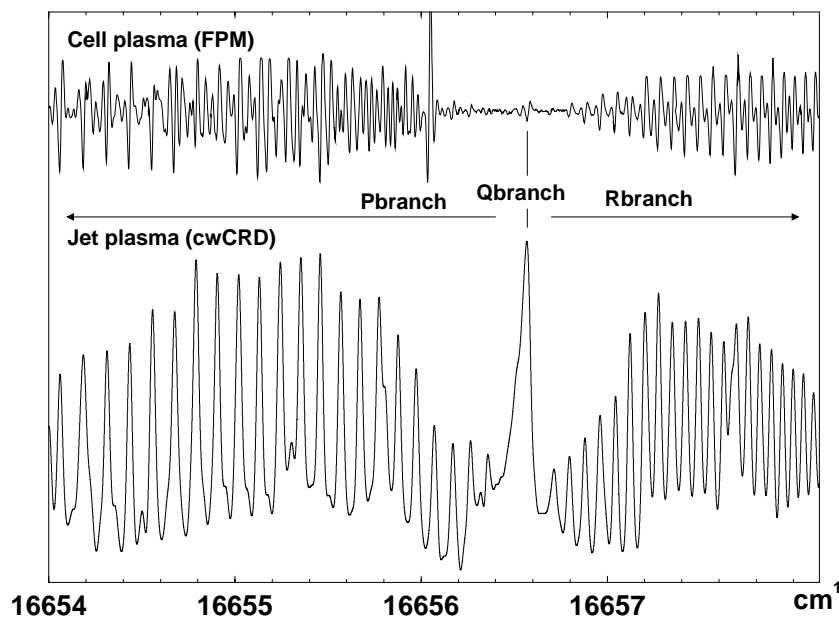


Fig. 4. The origin band of the  $A^2\Pi_g - X^2\Pi_u$  electronic spectrum of triacetylene cation,  $HC_6H^+$ , measured by cw CRD spectroscopy through a supersonic pulsed planar plasma with  $T_{rot} \sim 15$  K (lower trace). The upper trace shows the corresponding cell spectrum using frequency-plasma double modulation spectroscopy with  $T_{rot} \sim 170$  K [21].

subsequent  $J$ -levels a rotational temperature of the order of 10 to 15 K is derived. The lower temperature favours the population of the low- $J$  rotational levels and as the Q-line strength is highest for low  $J$ -values the Q-branch is now much more pronounced. The spin-orbit splitting in the ground state is about  $-31 \text{ cm}^{-1}$  and as a consequence only the lower ( $\Omega = \frac{3}{2}$ ) spin-orbit component is observed.

The best achievable linewidth (FWHM), using a multichannel body was 450 MHz, two to three times smaller than possible up to now in pulsed laser experiments. This is sufficient to obtain rotational resolution for linear chains with 10 to 11 carbon atoms, as long as no lifetime broadening is involved. However, 450 MHz is still considerably larger than expected from the few MHz bandwidth of the cw laser system. Assuming a Doppler-broadened signal, this corresponds to a translational temperature of the order of 125 K. Indeed, this is due to residual Doppler broadening in the slit expansion, as has been observed before in FPM experiments [22]: the use of a slower expansion gas (for example Ar) reduces the achievable

linewidth proportional to the speed ratios. Clearly, further modifications in the expansion source are necessary to take advantage of the small bandwidth of the cw laser used. A possible improvement could be the use of skimmed planar expansions but such systems have not been reported in the literature yet. Furthermore, it might well be possible that molecular ions diffuse out of the expansion because of charge effects.

The present technique is an extension of previous work in which the same discharge source has been used in combination with a pulsed CRD [19] and a cw frequency-plasma double modulation [23] detection scheme. All three techniques – pulsed CRD, cw-CRD and FPM – have their own advantages and disadvantages.

The pulsed CRD is particularly suited for fast scans. A spectrum comparable to the one shown in Fig. 4 takes less than 20 min to record, whereas the two cw techniques need at least 1.5 h. In addition, special boxcar integration schemes are necessary to compensate for the low duty cycle that is typical when combining a cw detection with a pulsed production technique. The achievable resolution,

on the other hand, is substantially higher in the cw experiments and at this stage only limited by residual Doppler broadening in the expansion. The CRD experiments are generally applicable, whereas the application of the FPM experiment is restricted to absorption lines that are not broadened beyond the modulation amplitude ( $\sim 400$  MHz). The resulting line shape is a  $1f$  derivative as shown in the upper trace of Fig. 4.

The best achievable  $S/N$  ratios are comparable for the three methods. This is achieved by *noise reduction* in the FPM experiment – both laser and plasma noise are reduced in a phase sensitive detection scheme – and by *signal improvement* in the CRD experiments – here the effective absorption path length is increased.

#### 4. Conclusion

It has been shown that cw CRD spectroscopy is a sensitive and generally applicable method to study rotationally cold carbon chain radicals that are produced in a pulsed plasma expansion. The method will be particularly useful in the study of long species with small rotational constants. Passive mode matching is sufficient to perform the experiments. A reduction in linewidth has been obtained. The limiting factor turns out to be residual Doppler broadening in the expansion along the slit.

#### Acknowledgements

We thank Dr. M. Hippler and Prof. M. Quack for generously sharing their expertise in cw CRD. This work has been supported by the Swiss National Science Foundation, grant 20.63459.00. One of the authors (H.L.) also acknowledges support from FOM (Fundamenteel Onderzoek der Materie).

#### References

- [1] M.C. McCarthy, P. Thaddeus, Chem. Soc. Rev. 30 (2001) 177, and references therein.
- [2] A.G.G.M. Tielens and T.P. Snow, (Eds.), The diffuse interstellar bands, Dordrecht, 1995, pp. 175–238.
- [3] J.P. Maier, J. Phys. Chem. A. 102 (1998) 3462.
- [4] D.A. Kirkwood, M. Tulej, M.V. Pachkov, M. Schnaiter, F. Guthe, M. Grutter, M. Wyss, J.P. Maier, G. Fischer, J. Chem. Phys. 111 (1999) 9280.
- [5] T. Pino, H.B. Ding, F. Guthe, J.P. Maier, J. Chem. Phys. 114 (2001) 2208.
- [6] T. Motylewski, H. Linnartz, O. Vaizert, J.P. Maier, G.A. Galazutdinov, F.A. Musaev, J. Krelowski, G.A.H. Walker, D.A. Bohlender, Astrophys. J. 531 (2000) 312.
- [7] J.J. Scherer, P.B. Paul, A. O'Keefe, R.J. Saykally, Chem. Rev. 97 (1997) 25.
- [8] M.D. Wheeler, S.M. Newman, A.J. Orr-Ewing, M.N.R. Ashold, J. Chem. Soc. Faraday Trans. 94 (1998) 337.
- [9] G. Berden, R. Peeters, G. Meijer, Int. Rev. Phys. Chem. 19 (2000) 565.
- [10] A. O'Keefe, D.A.G. Deacon, Rev. Sci. Instrum. 59 (1988) 2544.
- [11] R. Engeln, G. von Helden, G. Berden, G. Meijer, Chem. Phys. Lett. 262 (1996) 105.
- [12] D. Romanini, A.A. Kachanov, N. Sadeghi, F. Stoeckel, Chem. Phys. Lett. 264 (1997) 316.
- [13] D. Romanini, A.A. Kachanov, F. Stoeckel, Chem. Phys. Lett. 270 (1997) 538.
- [14] B.A. Paldus, C.C. Harb, T.G. Spence, B. Wilke, J. Xie, J.S. Harris, R.N. Zare, J. Appl. Phys. 83 (1998) 3991.
- [15] Y. He, M. Hippler, M. Quack, Chem. Phys. Lett. 289 (1998) 527.
- [16] M. Murtz, B. Frech, W. Urban, Appl. Phys. B. 68 (1999) 243.
- [17] M. Hippler, M. Quack, Chem. Phys. Lett. 314 (1999) 273.
- [18] H. Linnartz, D. Pfluger, O. Vaizert, P. Cias, P. Birza, D. Khoroshev, J.P. Maier, J. Chem. Phys. 116 (2002) 924, and references therein.
- [19] T. Motylewski, H. Linnartz, Rev. Sci. Instrum. 70 (1999) 1305.
- [20] See D. Schleef, Linux Control and Measurement Device Interface, <ftp://stm.lbl.gov/pub/comedi/>.
- [21] W.E. Sinclair, D. Pfluger, H. Linnartz, J.P. Maier, J. Chem. Phys. 110 (1999) 296.
- [22] D. Pfluger, W.E. Sinclair, H. Linnartz, J.P. Maier, Chem. Phys. Lett. 313 (1999) 171.
- [23] D. Pfluger, T. Motylewski, H. Linnartz, W.E. Sinclair, J.P. Maier, Chem. Phys. Lett. 329 (2000) 29.





# Lifetime broadening in the gas phase $\tilde{B}^2\Pi \leftarrow \tilde{X}^2\Pi$ electronic spectrum of $C_8H$

Petre Birza, Dmitriy Khoroshev, Andrei Chirokolava,  
Tomasz Motylewski, John P. Maier \*

*Department of Chemistry, University of Basel, Klingelbergstr. 80, CH4056 Basel, Switzerland*

Received 9 October 2003; in final form 20 October 2003

## Abstract

The origin band of the  $\tilde{B}^2\Pi_{3/2} \leftarrow \tilde{X}^2\Pi_{3/2}$  electronic transition of linear  $C_8H$  was recorded in a planar supersonic expansion by a cw cavity ring-down spectrometer. The  $C_8H$  radical was produced using a discharge through a  $C_2H_2/He$  mixture inside a pulsed slit nozzle. Despite the fact that the resolution of the spectrometer is 350 MHz, which is 3–4 times higher than the separation of rotational lines in this band, the rotational structure was not resolved. It is concluded that the rotational lines are broadened by rapid radiationless transitions from the excited electronic state. Simulations of the spectrum give an estimate of  $0.8\text{ cm}^{-1}$  Lorentzian linewidth which corresponds to  $\sim 7$  ps lifetime in the excited  $\tilde{B}^2\Pi_{3/2}$  electronic state.

© 2003 Elsevier B.V. All rights reserved.

## 1. Introduction

Electronic spectra of carbon chains are especially of interest from the astrophysical point of view. Linear hydrocarbon chains  $C_nH$  play an important role in the interstellar chemistry. They were detected in the envelopes of evolved stars and interstellar dark and translucent clouds by radio astronomy [1–3]. These species were extensively studied in the laboratory by microwave [4,5] and electronic spectroscopies [6,7]. Recent

progress in experimental techniques made the measurement of rotationally resolved absorption spectra of electronic transitions in shorter carbon chains possible [8–12]. The origin band of the  $\tilde{B}^2\Pi \leftarrow \tilde{X}^2\Pi$  electronic transition of the  $C_{2n}H$  ( $n = 3 - 5$ ) radicals was observed in the gas phase using a combination of pulsed laser cavity ring-down spectroscopy (CRDS) with the slit-nozzle expansion of the discharge-generated species [8,13]. Whereas, the spectrum of  $C_6H$  was rotationally resolved, the ones of  $C_8H$  and  $C_{10}H$  were not. The reason was not clear. We attempted to resolve the rotational structure in the stronger ( $\Omega = 3/2$ ) component of the  $\tilde{B}^2\Pi \leftarrow \tilde{X}^2\Pi$  origin band of  $C_8H$  using a new cw-CRDS setup with resolution of 350 MHz.

\* Corresponding author. Fax: +41-61-267-38-55.

E-mail addresses: [Andrei.Chirokolava@unibas.ch](mailto:Andrei.Chirokolava@unibas.ch) (A. Chirokolava), [J.P.Maier@unibas.ch](mailto:J.P.Maier@unibas.ch) (J.P. Maier).

## 2. Experimental approach

The main features of the experiment have been described previously [12]. It is based on the passive cavity mode locking scheme for cw-CRDS [14]. A piezo moves back and forth one of the mirrors of the cavity. When the cavity comes into resonance with the laser frequency and intensity on the photodetector behind the cavity increases to a certain threshold, the laser beam is interrupted by switching off the acousto-optic modulator. The light intensity in the cavity and on the photodetector then decays exponentially with time. Due to spatial filtering and mode matching of the laser beam, only TEM<sub>00</sub> cavity modes have significant intensity. The timing of the valve opening and high voltage pulse is calculated so as to coincide with the ring-down.

A number of improvements to our previous setup [12] have been made. (1) Before, several signals (photodetector, pressure gauges, voltage applied to the piezo) were recorded by the same data acquisition card, which switched between different channels. The switching resulted in spikes in the ring-down signal. Now two data acquisition cards are used, one for the ring-down signal, the other for all other signals, so there are no spikes. (2) The algorithm for triggering the gas and HV

pulses has been changed. The delays for activating the valve and discharge are measured from the first resonance on the ascending voltage ramp (Fig. 1), rather than from the analysed ring-down in the last period of the triangular-wave voltage. This algorithm is more robust and allows for larger steps in the laser scan. Non-linear response of the piezo element to the applied voltage results in slightly different delays between the first and the second resonances, depending on their positions with respect to the voltage ramp. This leads to the changes in relative timing of the HV pulse and the ring-down event as the laser is scanned and the resonances move relative to the ramp. To preserve this relative timing, the delay between the first resonance and the HV pulse is adjusted taking into account piezo nonlinearity. (3) The triangular-wave voltage for the piezo element is generated now by the data acquisition card instead of the stand-alone function generator. After all these changes, the signal-to-noise ratio improved 2.5 times. The achieved sensitivity was of order  $10^{-7}$ – $10^{-8}$  cm<sup>-1</sup>.

The carbon chain species were generated by applying a high voltage pulse (–1000 V, 150 mA) to a 0.2% gas mixture of acetylene in helium expanding through the slit nozzle (3 cm × 200 μm) with the backing pressure of 11 bar. The pressure

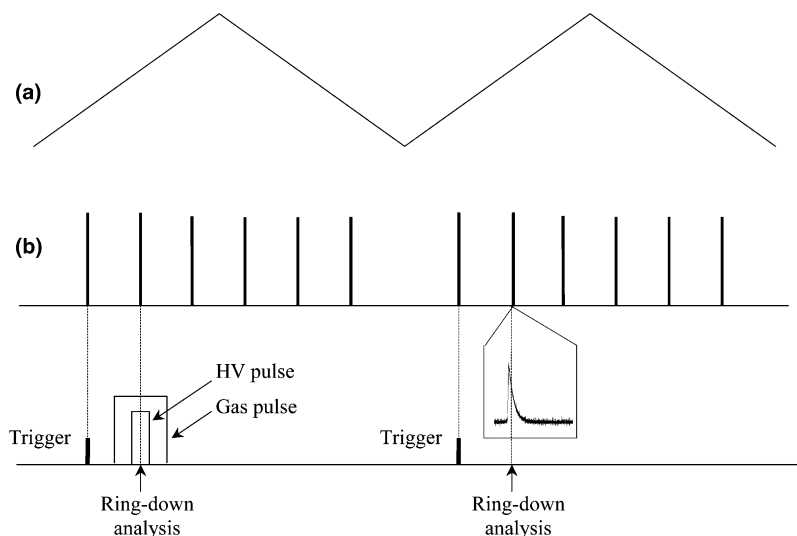


Fig. 1. Relative timing of the piezo ramp voltage, cavity resonances, valve opening, and high voltage pulse applied to the slit electrodes. (a) Ramp voltage applied to the piezo. (b) Signal on the photodetector.

in the vacuum chamber was 0.23 mbar. The laser beam crossed the jet 10 mm downstream the expansion. The number density of  $C_8H$  species in this region was estimated using a theoretical oscillator strength ( $3.4 \times 10^{-3}$ ) for this electronic transition [15]. In the 5 K neon matrix spectrum, the integrated absorption of the origin band is approximately equal to that of the other vibronic bands in the  $\tilde{B}^2\Pi \leftarrow \tilde{X}^2\Pi$  system [6]. Because only the origin band was measured in our experiment, the oscillator strength was reduced accordingly and leads to an estimate of the  $C_8H$  number density in the discharge plasma of  $6 \times 10^8 \text{ cm}^{-3}$ .

### 3. Results and discussion

The recorded spectrum is shown in Fig. 2. The two broad features are the *P* and *R* branches of the origin band of the  $\tilde{B}^2\Pi_{3/2} \leftarrow \tilde{X}^2\Pi_{3/2}$  electronic transition of  $C_8H$ . This band was first observed in 5 K neon matrix using mass-selected deposition [6]. It was assigned in the gas phase [13] on the basis of the known gas phase – neon matrix shifts [16] for similar hydrocarbon chains. This assignment was confirmed by equal frequency shifts resulting from

deuterium substitution in the neon matrix [17] and in the supersonic jet experiment [13].

The large narrow peaks belong to another carrier, propadienyldiene ( $H_2CCC$ ). They are much stronger in this spectrum compared to the earlier measurement [13], because a slightly different nozzle design [12] has been used. The latter minimizes Doppler broadening, but at the same time increases the production of shorter carbon chains. Although overlap with the features of another carrier complicates the spectrum, one can see that the rotational structure of  $C_8H$  remains unresolved.

The distance between the lines in the *P* and *R* branches is expected to be about  $0.04 \text{ cm}^{-1}$  (1.2 GHz). Our resolution, estimated by the width of the narrowest feature (FWHM) in the spectrum, was at least 350 MHz. It should be more than sufficient to resolve the rotational structure of the  $C_8H$  band. One can compare this spectrum to the origin band in the  $\tilde{A}^2\Pi_{3/2} \leftarrow \tilde{X}^2\Pi_{3/2}$  transition of the isoelectronic linear tetraacetylene cation,  $HC_8H^+$ , recorded under similar conditions with a laser linewidth of  $\sim 900 \text{ MHz}$  (see Fig. 2 of [9]). There the *P* branch is well resolved; the *R* branch is partially resolved.

The rotational level broadening in the upper  $\tilde{B}^2\Pi$  electronic state of  $C_8H$  is caused by rapid

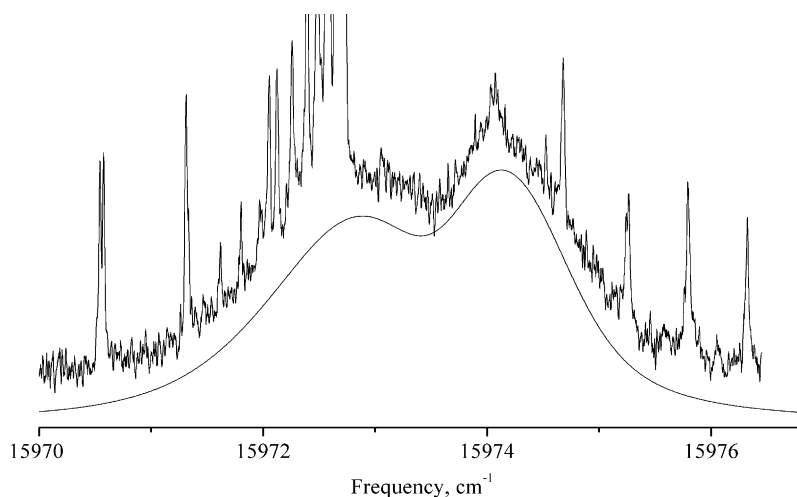


Fig. 2. Experimental and simulated spectra of the origin band in the  $\tilde{B}^2\Pi_{3/2} \leftarrow \tilde{X}^2\Pi_{3/2}$  electronic transition of  $C_8H$ . The spectrum was recorded in absorption across a pulsed supersonic slit jet using a cw cavity ring-down approach. The two broad features are the *P* and *R* branches of this electronic transition. The narrow peaks belong to propadienyldiene  $H_2CCC$ . Upper state rotational constant for the simulated spectrum is  $B' = 0.0195 \pm 0.0001 \text{ cm}^{-1}$ , other constants are fixed to the ground state values [4]. Rotational temperature is  $T_{\text{rot}} = 15 \pm 2 \text{ K}$ , Lorentzian broadening  $\Delta\nu_{\text{lor}} = 0.8 \pm 0.1 \text{ cm}^{-1}$  (24 GHz). The simulated spectrum is slightly shifted down with respect to the experimental one.

radiationless transitions from this electronic state. Nonradiative relaxation of the  $\tilde{B}^2\Pi$  electronic state is present in other members of the  $C_{2n}H$  series as well. It manifests itself as a two-component fluorescence decay in  $C_4H$  with excited state lifetime estimate of 20 ns [18]. In the case of  $C_6H$  [8], the  $\tilde{B}^2\Pi_{3/2} \leftarrow \tilde{X}^2\Pi_{3/2}$  electronic absorption spectrum is best simulated when a Lorentzian broadening of  $\sim 0.055 \text{ cm}^{-1}$  is introduced in addition to a Gaussian linewidth of  $0.037 \text{ cm}^{-1}$  resulting from the laser linewidth and Doppler broadening. This corresponds to an excited state lifetime of order 0.1 ns.

We simulated the observed broadening in the  $\tilde{B}^2\Pi_{3/2} \leftarrow \tilde{X}^2\Pi_{3/2}$  origin band of  $C_8H$  (Fig. 1) by varying three parameters; upper state rotational constant  $B'$ , rotational temperature  $T_{\text{rot}}$ , and Lorentzian linewidth  $\Delta\nu_{\text{lor}}$ .  $B''$  was fixed to the value of  $0.019589011 \text{ cm}^{-1}$  taken from [4]. The obtained values are  $B' = 0.0195 \pm 0.0001 \text{ cm}^{-1}$ ,  $T_{\text{rot}} = 15 \pm 2 \text{ K}$ , and  $\Delta\nu_{\text{lor}} = 0.8 \pm 0.1 \text{ cm}^{-1}$  (24 GHz), respectively. Thus, the ratio  $B'/B''$  for  $C_8H$  is  $0.995 \pm 0.005$ , which is close to the value of 0.99 for isoelectronic species [9–11].

In contrast to  $C_8H$ , the rotational structure is well resolved for the corresponding  $\tilde{A}^2\Pi \leftarrow \tilde{X}^2\Pi$  electronic origin bands of the isoelectronic linear cations  $HC_8H^+$  [9],  $HC_7N^+$  [10] and  $NC_6N^+$  [11]. Apparently, the presence of an additional low-lying  $^2\Sigma^+$  excited electronic state in the  $C_6H$  and  $C_8H$  radicals [15,19–21] enhances vibronic interactions between the  $\tilde{B}^2\Pi$  and lower electronic states and accelerates internal conversion. This broadening caused by intramolecular processes is one of the reasons why carbon chains attracted attention in connection with the diffuse interstellar bands [22].

### Acknowledgements

This work has been supported by the Swiss National Science Foundation (project 200020-100019).

### References

- [1] M. Guelin, J. Cernicharo, M.J. Travers, M.C. McCarthy, C.A. Gottlieb, P. Thaddeus, M. Ohishi, S. Saito, S. Yamamoto, *Astron. Astrophys.* 317 (1997) L1.
- [2] M.B. Bell, P.A. Feldman, J.K.G. Watson, M.C. McCarthy, M.J. Travers, C.A. Gottlieb, P. Thaddeus, *Astrophys. J.* 518 (1999) 740.
- [3] B.E. Turner, E. Herbst, R. Terzieva, *Astrophys. J. Suppl. Ser.* 126 (2000) 427.
- [4] M.C. McCarthy, M.J. Travers, A. Kovacs, C.A. Gottlieb, P. Thaddeus, *Astrophys. J. Suppl. Ser.* 113 (1997) 105.
- [5] C.A. Gottlieb, M.C. McCarthy, M.J. Travers, J.U. Grabow, P. Thaddeus, *J. Chem. Phys.* 109 (1998) 5433.
- [6] P. Freivogel, J. Fulara, M. Jakobi, D. Forney, J.P. Maier, *J. Chem. Phys.* 103 (1995) 54.
- [7] H. Ding, T. Pino, F. Guthe, J.P. Maier, *J. Chem. Phys.* 117 (2002) 8362.
- [8] H. Linnartz, T. Motylewski, O. Vaizert, J.P. Maier, A.J. Apponi, M.C. McCarthy, C.A. Gottlieb, P. Thaddeus, *J. Mol. Spectrosc.* 197 (1999) 1.
- [9] D. Pfluger, T. Motylewski, H. Linnartz, W.E. Sinclair, J.P. Maier, *Chem. Phys. Lett.* 329 (2000) 29.
- [10] W.E. Sinclair, D. Pfluger, D. Verdes, J.P. Maier, *J. Chem. Phys.* 112 (2000) 8899.
- [11] H. Linnartz, D. Pfluger, O. Vaizert, P. Cias, P. Birza, D. Khoroshev, J.P. Maier, *J. Chem. Phys.* 116 (2002) 924.
- [12] P. Birza, T. Motylewski, D. Khoroshev, A. Chirokolava, H. Linnartz, J.P. Maier, *Chem. Phys.* 283 (2002) 119.
- [13] H. Linnartz, T. Motylewski, J.P. Maier, *J. Chem. Phys.* 109 (1998) 3819.
- [14] M. Hippler, M. Quack, *Chem. Phys. Lett.* 314 (1999) 273.
- [15] A.L. Sobolewski, L. Adamowicz, *J. Chem. Phys.* 102 (1995) 394.
- [16] J.P. Maier, *J. Phys. Chem. A* 102 (1998) 3462.
- [17] P. Freivogel, Ph.D. Dissertation, University of Basel, Basel, 1997.
- [18] K. Hoshina, H. Kohguchi, Y. Ohshima, Y. Endo, *J. Chem. Phys.* 108 (1998) 3465.
- [19] T.R. Taylor, C. Xu, D.M. Neumark, *J. Chem. Phys.* 108 (1998) 10018.
- [20] J. Myung Lee, L. Adamowicz, *Spectrochim. Acta. Part A* 57A (2001) 897.
- [21] Z. Cao, S.D. Peyerimhoff, *Phys. Chem. Chem. Phys.* 3 (2001) 1403.
- [22] A.E. Douglas, *Nature* 269 (1977) 130.

---

## 8.6 Curriculum vitae of the author

### Personalities

Name:	Dmitriy Khoroshev
Date of birth:	25.05.1979
Place of birth:	Tobolsk, Russia
Nationality:	Russian
Marital status:	Single

### Education

09.1986 – 06.1995	Primary and Secondary School, Tobolsk, Russia
08.1995 – 06.1996	Physics-Mathematics School at Novosibirsk State University, Novosibirsk, Russia
09.1996 – 07.2000	Undergraduate at Novosibirsk State University, Novosibirsk, Russia
17.07.2000	Diploma with Distinction "Bachelor of Science in Ecology and Nature Resource Using", Novosibirsk, Russia
20.06.2002	Diploma with Distinction "Master of Science in Chemistry", Novosibirsk, Russia
08.2000 – 03.2005	Graduate in the group of Prof. J.P. Maier, Department of Chemistry, University of Basel, Switzerland
07.04.2005	Ph.D. in Chemistry, University of Basel, Switzerland